

# QPM Devices in KTA and RKTP

Andrius Žukauskas



**KTH Engineering Sciences**

Doctoral Thesis

Department of Applied Physics

KTH – Royal Institute of Technology

Stockholm, Sweden 2014

***QPM Devices in KTA and RKTP***

© Andrius Zukauskas, 2014

Laser Physics

Department of Applied Physics

KTH – Royal Institute of Technology

106 91 Stockholm

ISBN 978-91-7501-974-1

TRITA-FYS 2013:71

ISSN 0280-316X

ISRN KTH/FYS/--13:71--SE

Akademisk avhandling som med tillstånd av Kungliga Tekniska Högskolan framlägges till offentlig granskning för avläggande av teknologie doktorsexamen fredagen, den 31 Januari 2014, Albanova, Roslagstullsbacken 21, KTH, Stockholm. Avhandlingen kommer att försvaras på engelska.

Cover picture: QPM crystals with 5 mm, 3 mm and 1 mm apertures

Printed by Universitetsservice US AB, Stockholm 2014

Andrius Zukauskas

*QPM Devices in KTA and RKTP*

Department of Applied Physics, KTH – Royal Institute of Technology

106 91 Stockholm, Sweden

ISBN 978-91-7501-974-1

## Abstract

Even though  $\text{KTiOPO}_4$  (KTP) is considered to be one of the best nonlinear materials for quasi-phase matched (QPM) frequency conversion in the visible and the near-infrared spectral regions, its use is often limited by poor material homogeneity, high ionic conductivity, a considerable linear absorption and photochromatic damage. On the other hand, the improved material homogeneity and the lower ionic conductivity of bulk Rb-doped KTP (RKTP) make this material an ideal alternative for fabrication of fine-pitch QPM gratings, while the arsenate isomorph  $\text{KTiOAsO}_4$  (KTA) promises a better performance in the green spectral region and adds the advantage of a wider transparency window in the infrared. Unfortunately, the available studies on these materials are limited and unable to answer the question whether RKTP and KTA are feasible alternatives to KTP in terms of periodic poling and optical performance.

The optical performance of the QPM devices depends on the periodic poling quality, therefore, a detailed comprehension of domain-grating formation in the KTP isomorphs is highly desired. The goals of this thesis were to gain a better understanding of the periodic poling process in the KTP isomorphs, in order to study the specifics of ferroelectric domain engineering in KTA and RKTP, and to evaluate the optical performance of these isomorphs. Fine-pitch periodically-poled structures were engineered both in KTA and RKTP crystals. It was demonstrated that QPM gratings with excellent quality and with periods as short as  $8.49 \mu\text{m}$  can be fabricated in KTA crystals. Comparative transmission studies have shown that periodically poled KTA (PPKTA) crystals can be superior to KTP for QPM second harmonic generation in the visible spectral region due to lower linear absorption.

It was also demonstrated that RKTP is a superior alternative to KTP for high-quality QPM grating fabrication. A consistent room-temperature periodic poling of 5 mm thick RKTP crystals with a period of  $38.86 \mu\text{m}$  has been achieved. The obtained large aperture periodically poled RKTP (PPRKTP) crystals showed an outstanding QPM grating uniformity and excellent optical performance in optical parametric oscillator (OPO) applications. Moreover, it was shown that RKTP is less susceptible to blue-induced infrared absorption than KTP.

Finally, a novel and a relatively simple method for self-assembling quasi-periodic sub- $\mu\text{m}$  scale ferroelectric domain structure in RKTP crystals has been presented. It was shown that, after treatment in aqueous  $\text{KOH}/\text{KNO}_3$  solution, periodic poling of RKTP with planar electrodes resulted in one-dimensional ferroelectric domain structure with an average periodicity of  $650 \pm 200 \text{ nm}$ , extending over the whole 1 mm thick crystal. Such self-assembled structures in RKTP were used to demonstrate 5<sup>th</sup> order non-collinear QPM backward second harmonic generation.

## Sammanfattning

Kaliumtitanylfosfat ( $\text{KTiOPO}_4$ , KTP) anses allmänt vara ett av de bästa icke-linjära optiska materialen för kvasifasanpassad (QPM) frekvenskonvertering i det synliga och nära-infraröda våglängdsområdet. Materialets användbarhet begränsas dock ofta av den höga andelen K-vakanser och materialdefekter vilket leder till hög ledningsförmåga. Vidare har KTP en relativt hög linjär absorption i det synliga området och relativt låg intensitetbroende skadeträskel. Rubidiumdopad KTP (RKTP), med dess lägre defektkoncentration och ledningsförmåga är ett bättre alternativ vid tillverkning av domängitter med korta perioder, medan isomorfen  $\text{KTiOAsO}_4$  (KTA) ger bättre prestanda i det gröna våglängdsområdet samt utökad transmission i det infraröda våglängdsområdet. Tidigare har dessa material inte studerats i någon större utsträckning och det var då oklart om RKTP och KTA är lämpliga alternativ till KTP vad gäller periodisk polning och optisk prestanda.

Vid QPM används s.k. periodiskt polade kristaller för vilka frekvenskonverteringens verkningsgrad och den frekvenskonverterade strålens optiska kvalitet beror på det skapade domängittrets kvalitet. Därför vore det önskvärt med en djupare förståelse för hur domängitter skapas i KTP-isomorfer under periodisk polning. I detta syfte har polningsprocessen i KTP och dess isomorfer, KTA och RKTP studerats och den optiska kvaliteten hos de skapade domängittren har undersökts. Domängitter med korta perioder har skapats i både KTA och RKTP, och i fallet KTA har det visats att homogena gitter med en period så kort som  $8.49 \mu\text{m}$  kan tillverkas. En jämförande studie av domängittren skapade i de olika kristallerna har visat att KTA är överlägset KTP för frekvensdubbling i det synliga våglängdsområdet p.g.a. dess lägre linjära absorption.

I avhandlingen visas också att RKTP är överlägset KTP för skapande av domängitter av hög kvalitet. Homogena gitter med  $38,6 \mu\text{m}$  periodicitet har skapats i 5 mm tjocka kristaller genom polning vid rumstemperatur. Kristallerna har använts i för frekvenskonvertering i en optisk parametrisk oscillator och har uppvisat hög och jämn kvalitet längs hela kristallens tjocklek samtidigt so de hade hög optisk prestanda. Det har även visats att RKTP är mindre känsligt för infraröd absorption inducerat av blått ljus än KTP.

Slutligen har en ny, relativt enkel metod för skapande av självorganiserade kvasiperiodiska domänstrukturer med domänstorlekar under  $1 \mu\text{m}$  i RKTP demonstrerats. Kristallytorna behandlas med  $\text{KOH}/\text{KNO}_3$  i vattenlösning, följt av polning med plana elektroder vilket ger upphov till en kvasiperiodisk domänstruktur med genomsnittliga perioder mellan 500 nm och 700 nm över hela kristallens tjocklek. Dessa självorganiserade strukturer i RKTP användes för att visa femte ordningens QPM åstakomma kolinjär, motpropagerande frekvensdubbling.

## **Preface**

The research described in this thesis has been performed in the Laser Physics group, of the Applied Physics department at KTH (Royal Institute of Technology), in Stockholm, between 2009 and 2013.

This work has been in part funded by the Swedish Research Council (VR) through the Linnaeus Center of Excellence ADOPT, the Swedish Foundation for Strategic Research (SSF), the Göran Gustafsson Foundation, the Carl Trygger Foundation, and the EC FP7 project MIRSURG under Grant No. 224042.



## List of Publications

This thesis is based on the following journal papers:

- I. **A. Zukauskas**, N. Thilmann, V. Pasiskevicius, F. Laurell, and C. Canalias, “Periodically poled  $\text{KTiOAsO}_4$  for highly-efficient mid-infrared optical parametric devices,” *Appl. Phys Lett.* **95**, 191103 (2009).
- II. **A. Zukauskas**, N. Thilmann, V. Pasiskevicius, F. Laurell, and C. Canalias, “5 mm thick periodically poled Rb-doped KTP for high energy optical parametric frequency conversion”, *Opt. Mat. Express* **1**, 201-206 (2011).
- III. **A. Zukauskas**, G. Strömqvist, V. Pasiskevicius, F. Laurell, M. Fokine, and C. Canalias, “Fabrication of submicrometer quasi-phase-matched devices in KTP and RKTP,” *Opt. Mat. Express* **1**, 1319-1325 (2011).
- IV. **A. Zukauskas**, V. Pasiskevicius, and C. Canalias, "Second-harmonic generation in periodically poled bulk Rb-doped  $\text{KTiOPO}_4$  below 400 nm at high peak-intensities," *Opt. Express* **21**, 1395-1403 (2013).
- V. **A. Zukauskas**, V. Pasiskevicius, F. Laurell, and C. Canalias, “High-fidelity periodic domain structures in  $\text{KTiOAsO}_4$  for the visible spectral range,” *Opt. Mat. Express* **3**, 1444-1449 (2013).
- VI. **A. Zukauskas**, V. Pasiskevicius, and C. Canalias, “Quasi-periodic self-assembled sub- $\mu\text{m}$  ferroelectric bulk domain gratings in Rb-doped  $\text{KTiOPO}_4$ ,” accepted for publication in *Applied Physics Letters*.
- VII. P. Zeil, **A. Zukauskas**, S. Tjörnhammar, C. Canalias, V. Pasiskevicius, and F. Laurell, ”High-power continuous-wave frequency-doubling in  $\text{KTiOAsO}_4$ ,” *Opt. Express* **21**, 30453-30459 (2013).

## **Description of Author Contribution**

My contribution to the original papers has been the following:

### **Paper I**

I periodically poled the KTA crystals, participated in the optical evaluation experiments, discussions and the writing of the paper.

### **Paper II**

I periodically poled the large aperture crystals, participated in the optical evaluation experiments, discussions and the writing of the paper.

### **Paper III**

I participated in the sample preparation, periodic poling, discussions and the writing of the paper.

### **Paper IV**

I periodically poled the crystals, participated in the optical evaluation experiments, discussions and the writing of the paper.

### **Paper V**

I periodically poled the crystals, performed the optical evaluation experiments, participated in the discussions and the writing of the paper.

### **Paper VI**

I did the sample preparation, poling, and the optical evaluation experiments, participated in discussions and the writing of the paper.

### **Paper VII**

I provided the periodically poled KTA samples, participated in the discussions and the writing of the paper.

## Related Publications not Included in the Thesis

- A. A. Zukauskas, N. Thilmann, V. Pasiskevicius, F. Laurell, and C. Canalias, "Periodically Poled KTiOAsO<sub>4</sub> For Mid-Infrared Light Generation," Advanced Solid State Photonics (ASSP 2010), San Diego, USA, January 31 – February 3 (2010), AMC6.
- B. A. Zukauskas, V. Pasiskevicius, F. Laurell, and C. Canalias, "Grey-Track Resistant Periodically Poled Rb-doped KTiOPO<sub>4</sub> For Blue-Light Generation," Conference on Lasers and Electro-Optics (CLEO 2010), San Jose, USA, May 16-21 (2010), CMG3.
- C. A. Zukauskas, V. Pasiskevicius, F. Laurell, C. Canalias, M. Safinas, and A. Michailovas, "High-Performance Periodically Poled Rb-doped KTP For Frequency Conversion In Blue/Green Region," Europhoton 2010, Hamburg, Germany, August 29 – September 3 (2010), FrA4.
- D. N. Thilmann, G. Strömqvist, A. Zukauskas, B. Jacobsson, C. Canalias, V. Pasiskevicius, and F. Laurell, "Optical parametric oscillator at 2.1 μm with large aperture periodically poled KTiOPO<sub>4</sub>," Europhoton 2010, Hamburg, Germany, August 29 – September 3 (2010).
- E. F. Masiello, T. A. Lafford, P. Pernot, J. Baruchel, D. S. Keeble, P. A. Thomas, A. Zukauskas, G. Strömqvist, F. Laurell, and C. Canalias, "Investigation by coherent X-ray section topography of ferroelectric domain behavior as a function of temperature in periodically poled Rb:KTP," J. Appl. Cryst. **44**, 462-466 (2011).
- F. A. Zukauskas, N. Thilmann, V. Pasiskevicius, F. Laurell, and C. Canalias, "5 mm Thick Periodically Poled Rb:KTiOPO<sub>4</sub> for High Power Optical Frequency Conversion," Advanced Solid State Photonics (ASSP 2011), Istanbul, Turkey, February 13-16 (2011), JWB1.
- G. A. Zukauskas, N. Thilmann, V. Pasiskevicius, F. Laurell, and C. Canalias, "High Fidelity Large Aperture Periodically Poled Rb:KTiOPO<sub>4</sub> for High Energy Frequency Conversion," Conference on Lasers and Electro-Optics (CLEO 2011), Baltimore, USA, May 1-6 (2011), CTuE6.
- H. C. Canalias, A. Zukauskas, V. Pasiskevicius, and F. Laurell, "Submicrometer QPM devices," Nonlinear Optics: Materials, Fundamentals and Applications, 2011.
- I. U. Eismann, F. Gerbier, C. Canalias, A. Zukauskas, G. Trenec, J. Vigue, F. Chevy, and C. Salomon, "An all-solid-state laser source at 671 nm for cold-atom experiments with lithium," Appl. Phys. B **106**, 25-36 (2012).
- J. G. Stoepler, N. Thilmann, V. Pasiskevicius, A. Zukauskas, C. Canalias, and M. Eichhorn, "Tunable mid-infrared ZnGeP<sub>2</sub> RISTRA OPO pumped by periodically-poled Rb:KTP optic parametric master-oscillator power amplifier," Opt. Express **20**, 4509-4517 (2012).
- K. A. Zukauskas, V. Pasiskevicius, F. Laurell and C. Canalias, "Self-Assembled Ferroelectric Nano-Domain Gratings in Bulk RKTP", Conference on Lasers and Electro-Optics (CLEO 2012), San Jose, USA, May 6-11 (2012), CTh4D.4.

- L. A. Zukauskas, C. Liljestrand, V. Pasiskevicius, F. Laurell and C. Canalias, "Progress in Fabrication of sub- $\mu\text{m}$  QPM Devices in Bulk Rb-doped KTP", Europhoton 2012, Stockholm, Sweden, August 26-31 (2012), TuA.3.
- M. N. Thilmann, G. Stoepler, M. Eichhorn, V. Pasiskevicius, A. Zukauskas, and C. Canalias, "ZnGeP<sub>2</sub> RISTRA OPO in the mid-IR region pumped by a periodically poled KTiOPO<sub>4</sub> master-oscillator power amplifier," Europhoton 2012, Stockholm, Sweden, August 26-31 (2012), TuA.4.
- N. A. Zukauskas, V. Pasiskevicius, F. Laurell, and C. Canalias, "Periodically Poled KTiOAsO<sub>4</sub> for Second Harmonic Generation in the Green Region," Conference on Lasers and Electro-Optics (CLEO 2013), San Jose, USA, June 9-14 (2013), CW3B.3.
- O. H. Kianirad, A. Zukauskas, T. Frisk, C. Canalias, and F. Laurell, "Contact poling of RKTP with silicon needles," in Conference on Lasers and Electro-Optics Europe (CLEO Europe 2013), Munich, Germany, May 12-16 (2013), CD-7.6 MON.
- P. C. Canalias, A. Zukauskas, C. Liljestrand, V. Pasiskevicius, and F. Laurell, "Sub-wavelength Domain Engineering in KTP isomorphs: QPM Devices with Counter-propagating Photons," Conference on Lasers and Electro-Optics Pacific Rim (CLEO-PR 2013), Kyoto, Japan, June 30 – July 4 (2013), WA3-1.
- Q. P. Zeil, A. Zukauskas, C. Canalias, V. Pasiskevicius, and F. Laurell, "High-power continuous-wave frequency -doubling in KTiOAsO<sub>4</sub>," in Advanced Solid-State Lasers, ASSL 2013, (Optical Society of America, 2013), AM3A.4.
- R. K. Seger, N. Meiser, S. Tjörnhammar, A. Zukauskas, C. Canalias, V. Pasiskevicius, and F. Laurell, "Intra-cavity frequency-doubled Yb:KYW laser using periodically poled Rb-doped KTP with a volume Bragg grating input coupler," Appl. Phys. B., DOI 10.1007/s00340-013-5587-y.

## Acknowledgements

This thesis is a final product of my study years at KTH and I would like to express my greatest gratitude to the people who have helped and supported me throughout this project.

First of all, I would like to offer a special thanks to my main supervisor Dr. Carlota Canalias for introducing and guiding me through the path of KTP and periodic poling. I appreciate your excellent knowledge and enthusiasm which you have shared with me during those numerous hours in the lab. It is always a pleasure to have interesting discussions with you, both within and outside the field of periodic poling. I am also very grateful for the priceless support you provided during my research as well as criticism and advices which helped me to grow as a researcher.

I would also like to thank professor Valdas Pasiskevicius and professor Fredrik Laurell for accepting me as a PhD student in the Laser Physics group and providing priceless support and feedback during these five years.

I would like to express my gratitude to professor emeritus Jens A. Tellefsen for enthusiasm and valuable knowledge of English language that you kindly shared with me by proof-reading this thesis.

I am grateful to my colleagues: Nicky Thilmann, Hoon Jang, Peter Zeil, Hoda Kianirad, Charlotte Liljestränd, Gustav Lindgren, Kai Seger, Niels Meiser, Dr. Michael Fokine and Dr. Gustav Strömqvist for fruitful collaborations, shared experiments and nice discussions.

A special thanks goes to Staffan Tjörnhammar for being a nice office mate, and for interesting discussions about science and life.

Mårten Stjernström – one of the nicest persons I ever met in my life – I will never forget you.

Additionally, I would also like to thank Algis Stalnionis for waking my interest in nonlinear optics and pointing me in the right direction.

I am grateful to Tautvydas Lisauskas for numerous conversations about the PhD student's life and life in general during these five years.

I am also very grateful to my parents, my brother, my grandmother, my parents in law, and the rest of the family for their moral support.

Last, but not least, I would like to thank my beloved wife Agnè, who has always been by my side providing me with love and understanding. Thank you dear for believing in me, I hardly could have done it without you.



# Contents

<b>CHAPTER 1. INTRODUCTION</b>	<b>1</b>
<b>1.1. BACKGROUND AND MOTIVATION</b>	<b>1</b>
<b>1.2. THESIS STRUCTURE</b>	<b>3</b>
<b>REFERENCES</b>	<b>4</b>
<b>CHAPTER 2. BASIC PRINCIPLES OF NONLINEAR OPTICS</b>	<b>7</b>
<b>2.1. NATURE OF NONLINEAR PROCESSES</b>	<b>7</b>
<b>2.2. SECOND ORDER NONLINEAR PROCESSES</b>	<b>8</b>
<b>2.3. SECOND ORDER NONLINEAR COEFFICIENTS</b>	<b>10</b>
<b>2.4. COUPLED WAVE EQUATIONS</b>	<b>10</b>
<b>2.5. PHASE MATCHING</b>	<b>12</b>
<b>2.6. BIREFRINGENT PHASE MATCHING</b>	<b>14</b>
<b>2.7. QUASI-PHASE MATCHING</b>	<b>15</b>
<b>2.8. QPM SHG TUNING AND TOLERANCES</b>	<b>18</b>
<b>2.9. OPTIMAL FOCUSING WITH GAUSSIAN BEAMS</b>	<b>19</b>
<b>2.10. OPTICAL PARAMETRIC OSCILLATORS</b>	<b>20</b>
<b>REFERENCES</b>	<b>22</b>
<b>CHAPTER 3. FERROELECTRICS</b>	<b>23</b>
<b>3.1. CRYSTAL SYMMETRY</b>	<b>23</b>
<b>3.2. FERROELECTRIC MATERIALS</b>	<b>24</b>
<b>3.3. POLARIZATION REVERSAL</b>	<b>28</b>
<b>3.4. ROLE OF DEFECTS</b>	<b>30</b>
<b>REFERENCES</b>	<b>32</b>
<b>CHAPTER 4. KTP, RKTP AND KTA</b>	<b>35</b>
<b>4.1. INTRODUCTION</b>	<b>35</b>
<b>4.2. CRYSTAL STRUCTURE</b>	<b>35</b>
<b>4.3. CRYSTAL GROWTH</b>	<b>38</b>
<b>4.4. IONIC CONDUCTIVITY</b>	<b>39</b>
<b>4.5. OPTICAL PROPERTIES</b>	<b>41</b>
<b>4.6. SELLMEIER EQUATIONS</b>	<b>44</b>
<b>REFERENCES</b>	<b>47</b>

<b>CHAPTER 5. PERIODIC POLING OF THE KTP ISOMORPHS</b>	<b>51</b>
<hr/>	
5.1. INTRODUCTION	51
5.2. POLARIZATION SWITCHING CHARACTERISTICS IN THE KTP ISOMORPHS	51
5.3. DOMAIN BROADENING	56
5.4. SAMPLE PREPARATION	58
5.5. ELECTRIC FIELD POLING SETUP	59
5.6. ELECTRIC FIELD PULSE OPTIMIZATION	61
5.7. SAMPLE CHARACTERIZATION	64
REFERENCES	65
<b>CHAPTER 6. PERIODIC DOMAIN STRUCTURES IN KTA</b>	<b>67</b>
<hr/>	
6.1. KTA AS A NONLINEAR MEDIUM	67
6.2. PERIODIC POLING OF KTA	67
6.3. PPKTA-BASED OPO	69
6.4. PPKTA FOR SECOND HARMONIC GENERATION	70
6.5. TEMPERATURE TUNING CHARACTERISTICS	73
REFERENCES	76
<b>CHAPTER 7. LARGE APERTURE QPM DEVICES</b>	<b>77</b>
<hr/>	
7.1. LARGE APERTURE NONLINEAR CRYSTALS	77
7.2. PERIODIC POLING OF 5 MM THICK RKTP CRYSTALS	77
7.3. LARGE APERTURE PPRKTP OPO PERFORMANCE	80
REFERENCES	82
<b>CHAPTER 8. SHORT-PERIOD QPM DEVICES FOR BLUE LIGHT GENERATION</b>	<b>83</b>
<hr/>	
8.1. NEED OF SHORT-PERIOD QPM STRUCTURES	83
8.2. PERIODIC POLING OF SHORT-PERIOD QPM STRUCTURES	83
8.3. FREQUENCY CONVERSION IN THE BLUE REGION	84
REFERENCES	88
<b>CHAPTER 9. SUB-MM QPM DEVICES</b>	<b>89</b>
<hr/>	
9.1. INTRODUCTION	89
9.2. PERIODIC POLING OF SUB-MM QPM DEVICES	89
9.3. SELF-ASSEMBLED SUB-MM DOMAINS IN RKTP	91
REFERENCES	95
<b>CHAPTER 10. CONCLUSIONS</b>	<b>97</b>
<hr/>	

# Chapter 1. Introduction

## 1.1. Background and Motivation

The field of nonlinear optics emerged in 1961 with the first demonstration of second harmonic generation (SHG) [1.1], and developed very quickly, resulting in a wide range of applications both in fundamental research and in everyday life applications. Recent decades saw great progress both in designing new coherent radiation sources based on nonlinear optical frequency conversion, and in the development of new nonlinear materials which enabled the use of nonlinear optics in areas such as biology, medicine, spectroscopy, remote sensing, material processing, quantum optics, aerospace and defense applications. Indeed, nonlinear optical frequency conversion is one of the best and, sometimes, the only way to achieve coherent electromagnetic radiation in spectral regions where other coherent radiation sources are not available or lack technological advancement. Today, this is an active field of research, constantly demanding further development of nonlinear optical materials.

In order to ensure an efficient nonlinear frequency conversion, a proper phase relationship must be maintained between the interacting waves. This condition, known as phase matching, is not automatically fulfilled; therefore, several techniques have been developed to make efficient frequency conversion possible. The most commonly used method, so-called birefringent phase matching, relies on the material's birefringence in order to ensure an efficient power flow from the pump to the generated waves. Unfortunately, this technique suffers from several drawbacks including Poynting vector walkoff, polarization dependent nonlinearity, and limited frequency conversion spectral range.

Quasi-phase matching (QPM) is an alternative phase matching technique, which ensures efficient energy coupling between the interacting waves during the frequency conversion process and is essentially free of the drawbacks present in birefringent phase matching. Flexibility is perhaps the main advantage of QPM. It allows implementing any nonlinear interaction within the transparency range of the material at any temperature and for any set of polarizations of the interacting waves by appropriately designing the QPM structure. Moreover, it enables nonlinear interactions involving counter-propagating waves, which cannot be realized relying solely on the material's birefringence. Examples of these interactions are backward second harmonic generation, mirrorless optical parametric oscillators [1.2] and amplifiers, etc. QPM relies on periodic structuring of the material nonlinearity in order to reset the accumulated phase mismatch between the interacting waves every coherence length. Various methods to implement quasi-phase matching exist, including the growth of the orientation-patterned nonlinear materials [1.3], and different types of poling techniques [1.4-1.6]. Today, the most extensively used way to implement QPM is electric field poling of ferroelectric oxide crystals. Electric field poling was first demonstrated in 1993 in  $\text{LiNbO}_3$  (LN) [1.6], and since then,  $\text{LiNbO}_3$  and  $\text{LiTaO}_3$  (LT) have become the most intensively investigated and used materials for periodic poling. Those materials present some attractive properties, such as relatively high nonlinearity, wide transparency range,

## ***1.1. Background and Motivation***

commercial availability, and widely investigated periodic poling techniques, which are also relatively standardized today. Despite all the advantages, some serious drawbacks with those materials became apparent. One of the problems is photorefractive damage, which limits the use of LN to relatively low power applications. Another issue is a high coercive field ( $\sim 21$  kV/mm in congruent LN), limiting the possible apertures of QPM devices based on congruent LN to 0.5 mm. Considerable efforts in the area of crystal growth have resulted in the development of stoichiometric LN and LT crystals with substantially reduced coercive fields and improved optical properties. Later, developments in vapor transport equilibration (VTE) technique allowed the preparation of LN [1.7] and LT [1.8] crystals with near-stoichiometric compositions in a controlled manner. Doping with MgO resulted in improved resistance to photorefractive damage in those crystals. However, a trigonal crystal structure of LN and LT crystals favors hexagonal or triangular domain shapes, making the fabrication of one-dimensional QPM gratings with periods below  $7 \mu\text{m}$  and apertures  $>300 \mu\text{m}$  extremely difficult.

KTiOPO<sub>4</sub> (KTP) has also been extensively used for fabrication of QPM devices via electric field periodic poling. This material is considered to be one of the best for frequency conversion in the visible and the near-infrared spectral regions because of its good mechanical and thermal properties, as well as a high nonlinearity, absence of photorefractive damage and relatively high optical damage threshold. A wide transparency range of this material ( $0.35 - 4.3 \mu\text{m}$ ) makes it an ideal candidate for  $1\text{-}\mu\text{m}$ -pumped QPM second harmonic generation (SHG) and optical parametric oscillator (OPO) applications. The transmission window of the arsenate isomorphs extends the available spectral range further to  $\sim 5.2 \mu\text{m}$  in the infrared region. The relatively low coercive field of the KTP isomorphs allows, in principle, fabrication of large aperture QPM devices. Moreover, their orthorhombic crystal structure and the large anisotropy of the ferroelectric domain propagation velocities favor periodic poling of fine-pitch, high aspect ratio, one-dimensional QPM structures.

Clearly, KTP has established itself as a good nonlinear medium for QPM applications, however, it still suffers from serious drawbacks such as high ionic conductivity and unsatisfactory material homogeneity, which influence the quality of the periodic poling. In addition, photochromic damage and a considerable linear absorption in the green spectral region have detrimental effects on the optical performance of KTP.

On the other hand, its arsenate isomorph KTiOAsO<sub>4</sub> (KTA) promises a better performance for green-light generation due to the improved power handling properties [1.9], and a substantially reduced optical absorption at 532 nm. Unfortunately, the use of KTA for SHG applications involving birefringent type II phase matching is limited by a SHG wavelength cut-off around 1075 nm [1.10]. The potential of KTA for QPM applications in the visible region remains unexplored due to the difficulties in implementing short-period QPM structures. Moreover, due to the extended transmission range in the infrared spectral region, KTA also seems to be an ideal candidate for  $1 \mu\text{m}$ -pumped QPM OPO devices operating between  $2 \mu\text{m}$  and  $5 \mu\text{m}$ , which are important for spectroscopy and sensing [1.11], directed countermeasures, or few-cycle femtosecond pulse generation [1.12]. Additionally, employing such OPOs in cascaded schemes [1.13] allows reaching the  $6\text{-}12 \mu\text{m}$  spectral region, covering the second atmospheric

transmission window and the vibrational absorption bands of some biologically important organic molecules. Nevertheless, the limited number of available studies on periodic poling of KTA does not answer whether it is feasible to implement QPM in this material.

Recently, bulk Rb-doped KTP (RKTP) with a Rb doping of 0.3 % has been commercialized. Due to its relatively low ionic conductivity, it appears to be a better candidate for fabrication of high aspect-ratio ferroelectric domain gratings, and the improved homogeneity of this material promises higher poling yield. This is beneficial for obtaining large aperture QPM devices, which can be used for high-energy OPOs with applications in such areas as biology and medicine [1.14], or material processing [1.15]. Moreover, RKTP is also interesting for fabrication of fine pitch, particularly sub- $\mu\text{m}$ , QPM structures. Such structures can be employed to implement nonlinear interactions involving counter-propagating photons, paving the way to applications such as all-optical switching components [1.16-1.18], tunable slow-light structures [1.19], and ultra-bright, backward-wave biphoton sources for quantum information processing [1.20]. In addition, a lower susceptibility to gray-tracking promises a better performance of this material in the blue spectral region. Unfortunately, despite the superior properties of RKTP, a very limited amount of studies of this material is available to date.

The aim of this thesis was to develop periodically poled QPM devices based on RKTP and KTA crystals, as well as to assess their performance. A relatively simple fabrication method of fine ferroelectric-domain gratings in these materials was established through the optimization of the periodic poling procedure. This has enabled fabrication of bulk sub- $\mu\text{m}$  ferroelectric domain gratings in RKTP, demonstrating that this material is excellent for short-period QPM devices. In addition, periodic poling of 5 mm thick PPRKTP crystals has shown that this material is also the best choice for large aperture QPM device fabrication. The ability to achieve consistent periodic poling in KTA has clearly demonstrated that it can be superior to ordinary KTP both in OPO applications aiming to reach wavelengths of up to 5  $\mu\text{m}$  in the mid-infrared spectral region, and in SHG applications pumped by 1  $\mu\text{m}$  light.

## **1.2. Thesis structure**

This thesis is structured as follows: Chapter 2 describes the basic principles of nonlinear optics, including quasi-phase matching, which is a key concept behind the ferroelectric domain engineering for nonlinear optical applications. Chapter 3 introduces the principles of crystal symmetry, ferroelectricity, and polarization switching in ferroelectrics, which are important for understanding of ferroelectric domain engineering in KTP. In Chapter 4, the most important physical properties of the KTP isomorphs are described. Chapter 5 introduces the electric field poling technique and outlines the specifics of the periodic poling of the KTP isomorphs. Chapter 6 describes the periodic poling of KTA for OPO and SHG applications. In Chapter 7 fabrication and evaluation of 5 mm thick PPRKTP crystals are detailed. Chapter 8 introduces fabrication of short period QPM structures with large aspect ratios in 1 mm thick crystals for blue light generation. In Chapter 9, periodic poling of sub- $\mu\text{m}$  QPM structures and self-assembled domain structures in RKTP is reported.

## References

- 1.1. P. A. Franken, A. E. Hill, C. W. Peters, and G. Weinreich, "Generation of optical harmonics," *Phys. Rev. Lett.* **7**, 118 (1961).
- 1.2. C. Canalias and V. Pasiskevicius, "Mirrorless optical parametric oscillator," *Nature Photonics* **1**, 459-462 (2007).
- 1.3. C. B. Ebert, L. A. Eyres, M. M. Fejer, and J. S. Harris, Jr., "MBE of antiphase GaAs films using GaAs/Ge/GaAs heteroepitaxy," *J. Crystal Growth*, **201/202**, 187 (1999).
- 1.4. M. C. Gupta, W. P. Risk, A. C. G. Nutt, and S. D. Lau, "Domain inversion in  $\text{KTiOPO}_4$  using electron beam scanning," *Appl. Phys. Lett.* **63**, 1167-1169 (1993).
- 1.5. W. P. Risk, and S. D. Lau, "Periodic electric field poling of  $\text{KTiOPO}_4$  using chemical patterning," *Appl. Phys. Lett.* **69**, 3999-4001 (1996).
- 1.6. M. Yamada, N. Nada, M. Saitoh, and K. Watanabe, "First-order quasi-phase matched  $\text{LiNbO}_3$  waveguide periodically poled by applying an external field for efficient blue second-harmonic generation," *Appl. Phys. Lett.* **62**, 435-436 (1993).
- 1.7. P. F. Bordui, R. G. Norwood, D. H. Jundt, and M. M. Fejer, "Preparation and characterization of off-congruent lithium niobate crystals," *J. Appl. Phys.* **71**, 875-879 (1992).
- 1.8. M. Katz, R. K. Route, D. S. Hum, K. R. Parameswaran, G. D. Miller, and M. M. Fejer, "Vapor-transport equilibrated near-stoichiometric lithium tantalate for frequency-conversion applications," *Opt. Lett.* **29**, 1775-1777 (2004).
- 1.9. W. R. Bosenberg, L. K. Cheng, and J. D. Bierlein, "Optical parametric frequency conversion properties of  $\text{KTiOAsO}_4$ ," *Appl. Phys. Lett.* **65**, 2765-2767 (1994).
- 1.10. J. D. Bierlein, H. Vanherzeele, and A. A. Ballman, "Erratum: "Linear and nonlinear optical properties of flux-grown  $\text{KTiOAsO}_4$ ," [*Appl. Phys. Lett.* **54**, 783 (1989)]," *Appl. Phys. Lett.* **61**, 3193 (1992).
- 1.11. A. K. Y. Ngai, S. T. Persijn, M. M. J. W. Van Herpen, S. M. Cristescu, and F. J. M. Harren, *Mid-Infrared Coherent Sources and Applications*, (Springer, New York, 2008).
- 1.12. O. Chalus, Ph. K. Bates, M. Smolarski, and J. Biegert, "Mid-IR short-pulse OPCPA with micro-Joule energy at 100kHz," *Opt. Express* **17**, 3587 (2009).
- 1.13. M. W. Haakestad, G. Arisholm, E. Lippert, S. Nicolas, G. Rustad, and K. Stenersen, "High-pulse-energy 8  $\mu\text{m}$  laser source based on optical parametric amplification in  $\text{ZnGeP}_2$ ," *Proc. SPIE* **6998**, 699812 (2008).
- 1.14. V. A. Serebryakov, E. V. Boiko, N. N. Petrishchev, and A. V. Yan, "Medical applications of mid-IR lasers. Problems and prospects," *J. Opt. Technol.* **77**, 6-17 (2010).
- 1.15. S. T. Yang, M. J. Matthews, S. Elhadj, D. Cooke, G. M. Guss, V. G. Draggoo, and P. J. Wegner, "Comparing the use of mid-infrared versus far-infrared lasers for mitigating damage growth on fused silica," *Appl. Opt.* **49**, 2606-2616 (2010).

- 1.16. G. D. Landry and T. A. Maldonado, "Efficient nonlinear phase shifts due to cascaded second-order processes in a counterpropagating quasi-phase-matched configuration," *Opt. Lett.* **22**, 1400-1402 (1997).
- 1.17. G. D. Landry and T. A. Maldonado, "Switching and second Harmonic generation using counterpropagating quasi-phase-matching in a mirrorless configuration," *J. Lightwave Technol.* **17**, 316-320 (1999).
- 1.18. K. Gallo, G. Assanto, K. R. Parameswaran, and M. M. Fejer, "All-optical diode in a periodically poled lithium niobate waveguide," *Appl. Phys. Lett.* **79**, 314-316 (2001).
- 1.19. J. Khurgin, "Slowing and stopping photons using backward frequency conversion in quasi-phase-matched waveguides," *Phys. Rev. A* **72**, 023810 (2005).
- 1.20. C.-S. Chu and S. E. Harris, "Ultrabright backward-wave biphoton source," *Phys. Rev. A* **83**, 061803 (2011).



## Chapter 2. Basic principles of nonlinear optics

### 2.1. Nature of nonlinear processes

The term “nonlinear optics” reflects the nonlinear material response to an applied optical field. In optics, when the applied optical field strength is low, the induced polarization in a dielectric material depends on the applied optical field linearly. For a quasi-monochromatic wave and lossless and dispersionless medium, the induced polarization can be expressed as:

$$\tilde{P}(t) = \varepsilon_0 \chi^{(1)} \tilde{E}(t), \quad (2.1.1)$$

where  $\varepsilon_0$  is the permittivity of free space and  $\chi^{(1)}$  is the linear susceptibility. However, when intense light interacts with the nonlinear medium, the material response can be extended into a power series of  $\tilde{E}(t)$ :

$$\begin{aligned} \tilde{P}(t) &= \varepsilon_0 [\chi^{(1)} \tilde{E}(t) + \chi^{(2)} \tilde{E}^2(t) + \chi^{(3)} \tilde{E}^3(t) + \dots] = \\ &= \tilde{P}^{(1)}(t) + \tilde{P}^{(2)}(t) + \tilde{P}^{(3)}(t) + \dots. \end{aligned} \quad (2.1.2)$$

Here,  $\chi^{(2)}$  and  $\chi^{(3)}$  are the second order and the third order nonlinear optical susceptibilities, respectively. Considering the vector nature of the fields,  $\chi^{(2)}$  is a third rank tensor and  $\chi^{(3)}$  is a fourth rank tensor.

Let us now consider the second order contribution to the nonlinear polarization:

$$\tilde{P}^{(2)}(t) = \varepsilon_0 \chi^{(2)} \tilde{E}^2(t). \quad (2.1.3)$$

Changing the sign of  $\tilde{E}(t)$  should also change the sign of the nonlinear response, if we assume inversion symmetry:

$$-\tilde{P}^{(2)}(t) = \varepsilon_0 \chi^{(2)} [-\tilde{E}(t)]^2, \quad (2.1.4)$$

which is equivalent to:

$$-\tilde{P}^{(2)}(t) = \varepsilon_0 \chi^{(2)} \tilde{E}^2(t). \quad (2.1.5)$$

From Eq. (2.1.3) and Eq. (2.1.5) it is clear that  $\chi^{(2)}$  should be zero in this case, therefore, second order nonlinear optical interactions can only occur only in noncentrosymmetric crystals, whereas third order interactions can occur both in centrosymmetric and noncentrosymmetric media.

The nonlinear processes in which the initial and final quantum mechanical states of a system are identical, are identified as parametric [2.1]. In a parametric process, the population can be removed from the ground state only for brief intervals of time, when it resides on a virtual level. Processes, which involve the transfer of population from one real level to another, are known as non-parametric. Parametric processes can always be described by a real susceptibility, whereas

## 2.2. Second order nonlinear processes

for non-parametric processes, the susceptibility is complex. The photon energy is always conserved in a parametric process, while this is not necessary the case in non-parametric processes.

Examples of non-parametric processes are saturable absorption, multiphoton absorption and stimulated Raman scattering. Frequency doubling, third harmonic generation, or optical parametric generation - are examples of parametric processes. In this thesis, only parametric nonlinear processes of 2<sup>nd</sup> order are considered.

## 2.2. Second order nonlinear processes

An optical field, incident upon a  $\chi^{(2)}$  nonlinear medium, and consisting of two different frequency components,  $\omega_1$  and  $\omega_2$ , can be represented as:

$$\tilde{E}(t) = E_1 e^{-i\omega_1 t} + E_2 e^{-i\omega_2 t} + c. c. \quad (2.2.1)$$

Equations (2.1.3) and (2.2.1) give:

$$\tilde{P}^{(2)}(t) = \varepsilon_0 \chi^{(2)} [E_1^2 e^{-2i\omega_1 t} + E_2^2 e^{-2i\omega_2 t} + 2E_1 E_2 e^{-i(\omega_1 + \omega_2)t} + 2E_1 E_2^* e^{-i(\omega_1 - \omega_2)t} + c. c.] + 2\varepsilon_0 \chi^{(2)} [E_1 E_1^* + E_2 E_2^*]. \quad (2.2.2)$$

The complex polarization amplitudes of the four non-zero frequency components are as follows:

$$P(2\omega_1) = \varepsilon_0 \chi^{(2)} E_1^2 \text{ (SHG),}$$

$$P(2\omega_2) = \varepsilon_0 \chi^{(2)} E_2^2 \text{ (SHG),}$$

$$P(\omega_1 + \omega_2) = 2\varepsilon_0 \chi^{(2)} E_1 E_2 \text{ (SFG),}$$

$$P(\omega_1 - \omega_2) = 2\varepsilon_0 \chi^{(2)} E_1 E_2^* \text{ (DFG).}$$

The abbreviations given in brackets denote the respective nonlinear processes: second harmonic generation (SHG), sum frequency generation (SFG) and difference frequency generation (DFG), respectively. The fifth zero-frequency term in Eq. (2.2.2) corresponds to a process called optical rectification. It leads to the creation of a quasi-static electric field across the nonlinear crystal.

Sum frequency generation is illustrated in Fig. 2.1. The complex amplitude describing this process is given by:

$$P(\omega_1 + \omega_2) = 2\varepsilon_0 \chi^{(2)} E_1 E_2. \quad (2.2.3)$$

In this case, two photons at frequencies  $\omega_1$  and  $\omega_2$  are combined into a third photon at a frequency  $\omega_3$ . The solid line in the Fig. 2.1(b) represents the atomic ground state, while the dashed lines represent the virtual levels.

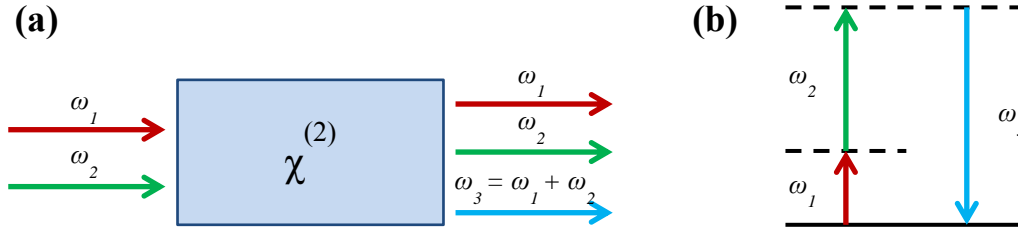


Fig. 2.1. Illustration of sum frequency generation (a) and the energy level diagram of the process (b).

A special case of sum frequency generation is the second harmonic generation, in which the two input waves have the same frequency,  $\omega_1 = \omega_2 = \omega$ , and the generated wave has the frequency of  $2\omega$ . SHG is often used to obtain coherent radiation at 532 nm by frequency doubling the well-established Nd:YAG lasers operating at 1064 nm.

The complex amplitude of the polarization for difference frequency generation is given by:

$$P(\omega_1 - \omega_2) = 2\varepsilon_0\chi^{(2)}E_1E_2^*. \quad (2.2.4)$$

This process is illustrated in Fig. 2.2. The generated wave has a frequency of  $\omega_3 = \omega_1 - \omega_2$ .

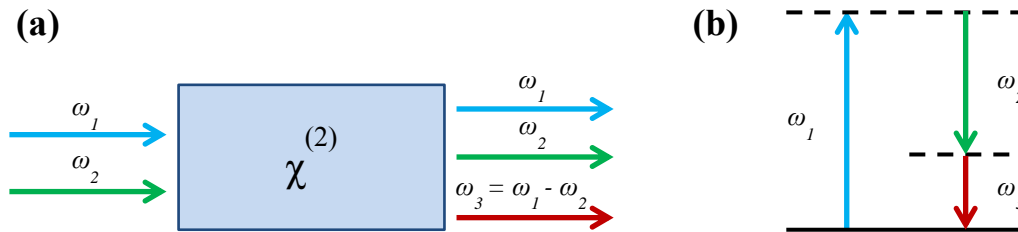


Fig. 2.2. Illustration of difference frequency generation (a) and the energy level diagram of the process (b).

The processes of sum frequency generation and difference frequency generation may appear to be very similar, however, there is an important difference: in DFG, one photon at frequency  $\omega_1$  is destroyed and, simultaneously, one new photon at a frequency  $\omega_2$  and another one at frequency  $\omega_3$  are created. Therefore, the input field at frequency  $\omega_2$  can be amplified, and thus this process is also called optical parametric amplification (OPA). This can even happen when the input at frequency  $\omega_2$  is absent, and, if the gain is high enough, a significant output power can be generated. Then the process is called optical parametric generation (OPG). If an optical resonator is added to the OPG, the output fields can be amplified to fairly large values, and such a device is called optical parametric oscillator (OPO). Conventionally, the interacting fields are called pump ( $\omega_1 = \omega_p$ ), signal ( $\omega_2 = \omega_s$ ) and idler ( $\omega_3 = \omega_i$ ), respectively, so that:  $\omega_p > \omega_s > \omega_i$ . An OPO can be wavelength-tuned, since any pair of frequencies  $\omega_2$  and  $\omega_3$  can satisfy the condition  $\omega_1 = \omega_2 + \omega_3$ . In practice, this is achieved by adjusting the phase-matching condition. OPOs are frequently used to obtain coherent radiation in the mid-infrared region, where there is a lack of other reliable coherent radiation sources.

### 2.3. Second order nonlinear coefficients

### 2.3. Second order nonlinear coefficients

In principle, the second order susceptibility is described as a third rank tensor with 27 different elements. However, when the frequencies of the optical waves in the nonlinear interaction are much smaller than the lowest resonance frequency of the material, the medium can be considered lossless, Kleinman symmetry can thus be applied [2.2], and a contracted notation can be used. The nonlinearity tensor,  $d$ , is often used instead of the susceptibility  $\chi^{(2)}$ :

$$d_{ijk} \equiv \frac{1}{2}\chi_{ijk}^{(2)}. \quad (2.3.1)$$

Under intrinsic permutation symmetry,  $d_{ijk}$  is symmetric with respect to the last two indices; therefore, the following simplified notation is usually adopted:

$$\begin{array}{cccccc} jk: & 11 & 22 & 33 & 23,32 & 31,13 & 12,21 \\ l: & 1 & 2 & 3 & 4 & 5 & 6 \end{array}$$

Then, the nonlinear coefficient matrix can be expressed as:

$$d_{il} = \begin{bmatrix} d_{11} & d_{12} & d_{13} & d_{14} & d_{15} & d_{16} \\ d_{21} & d_{22} & d_{23} & d_{24} & d_{25} & d_{26} \\ d_{31} & d_{32} & d_{33} & d_{34} & d_{35} & d_{36} \end{bmatrix}. \quad (2.3.2)$$

Then, the nonlinear polarization for SFG ( $\omega_1 + \omega_2 = \omega_3$ ) can be described as:

$$\begin{bmatrix} P_x(\omega_3) \\ P_y(\omega_3) \\ P_z(\omega_3) \end{bmatrix} = 4\epsilon_0 \begin{bmatrix} d_{11} & d_{12} & d_{13} & d_{14} & d_{15} & d_{16} \\ d_{21} & d_{22} & d_{23} & d_{24} & d_{25} & d_{26} \\ d_{31} & d_{32} & d_{33} & d_{34} & d_{35} & d_{36} \end{bmatrix} \begin{bmatrix} E_x(\omega_1)E_x(\omega_2) \\ E_y(\omega_1)E_y(\omega_2) \\ E_z(\omega_1)E_z(\omega_2) \\ E_y(\omega_1)E_z(\omega_2) + E_z(\omega_1)E_y(\omega_2) \\ E_x(\omega_1)E_z(\omega_2) + E_z(\omega_1)E_x(\omega_2) \\ E_x(\omega_1)E_y(\omega_2) + E_y(\omega_1)E_x(\omega_2) \end{bmatrix}. \quad (2.3.3)$$

When the Kleinman symmetry condition is valid, the number of independent elements further reduces from 18 to 10. The nonlinear coefficient matrix then acquires the following form:

$$d_{il} = \begin{bmatrix} d_{11} & d_{12} & d_{13} & d_{14} & d_{15} & d_{16} \\ d_{16} & d_{22} & d_{23} & d_{24} & d_{14} & d_{12} \\ d_{15} & d_{24} & d_{33} & d_{23} & d_{13} & d_{14} \end{bmatrix}. \quad (2.3.4)$$

### 2.4. Coupled wave equations

Using Maxwell's equations for a nonmagnetic nonlinear medium with no free charges and zero currents, the wave equation can be written as [2.1]:

$$\nabla^2 \tilde{\mathbf{E}} - \frac{\epsilon^{(1)}}{c^2} \frac{\partial^2 \tilde{\mathbf{E}}}{\partial t^2} = \frac{1}{\epsilon_0 c^2} \frac{\partial^2 \tilde{\mathbf{P}}^{NL}}{\partial t^2}. \quad (2.4.1)$$

Equation (2.4.1) has the form of a driven wave equation, where the nonlinear response of the material acts as a source term. For the case of SFG, the solution to this equation for a plane wave at frequency  $\omega_3$  propagating in  $+x$  direction, can be expressed as follows:

$$\tilde{E}_3(x, t) = A_3 e^{i(k_3 x - \omega_3 t)} + c. c., \quad (2.4.2)$$

where  $k_3 = \frac{n_3 \omega_3}{c}$ , and  $n_3^2 = \varepsilon^{(1)}(\omega_3)$ , are the wavenumber and the refractive index, respectively, at frequency  $\omega_3$ .

The applied optical fields are:

$$\begin{aligned} \tilde{E}_1(x, t) &= A_1 e^{i(k_1 x - \omega_1 t)} + c. c., \\ \tilde{E}_2(x, t) &= A_2 e^{i(k_2 x - \omega_2 t)} + c. c. \end{aligned} \quad (2.4.3)$$

The nonlinear source term in this case can be expressed as:

$$\tilde{P}_3(x, t) = P_3 e^{-i\omega_3 t} + c. c., \quad (2.4.4)$$

where  $P_3 = 4\varepsilon_0 d_{eff} A_1 A_2 e^{i(k_1 + k_2)x}$  and  $d_{eff}$  is an effective nonlinear coefficient, which depends on the polarizations of the interacting waves and on the phase matching conditions.

Using the slowly-varying-envelope-approximation (SVEA), the second derivative terms can be neglected:

$$\begin{aligned} \left| \frac{d^2 A_1}{dx^2} \right| &\ll \left| k_1 \frac{dA_1}{dx} \right|, \\ \left| \frac{d^2 A_2}{dx^2} \right| &\ll \left| k_2 \frac{dA_2}{dx} \right|, \\ \left| \frac{d^2 A_3}{dx^2} \right| &\ll \left| k_3 \frac{dA_3}{dx} \right|. \end{aligned} \quad (2.4.5)$$

Substituting Eqs. (2.4.2), (2.4.3), (2.4.4) and (2.4.5) into the wave equation, (2.4.1) gives the coupled wave equations for SFG:

$$\begin{aligned} \frac{dA_1}{dx} &= \frac{2id_{eff}\omega_1^2}{k_1 c^2} A_3 A_2^* e^{-i\Delta k x}, \\ \frac{dA_2}{dx} &= \frac{2id_{eff}\omega_2^2}{k_2 c^2} A_3 A_1^* e^{-i\Delta k x}, \\ \frac{dA_3}{dx} &= \frac{2id_{eff}\omega_3^2}{k_3 c^2} A_1 A_2 e^{i\Delta k x}, \end{aligned} \quad (2.4.6)$$

where  $\Delta k = k_1 + k_2 - k_3$  is the phase mismatch between the interacting waves.

## 2.5. Phase matching

### 2.5. Phase matching

Assuming undepleted input beams, the amplitudes  $A_1$  and  $A_2$  can be taken as constant in Eq. (2.4.6). For the special case of  $\Delta k = 0$  the amplitude  $A_3$  increases linearly with the propagation distance  $x$ . The condition  $\Delta k = 0$  is called perfect phase matching. Consequently, the intensity of the wave  $\omega_3$  increases quadratically with the propagation distance, and can be expressed as follows:

$$I_3 = \frac{8d_{eff}^2\omega_3^2I_1I_2}{n_1n_2n_3\epsilon_0c^2}L^2\text{sinc}^2\left(\frac{\Delta kL}{2}\right), \quad (2.5.1)$$

where  $L$  is the length of the nonlinear medium. The intensity  $I_3$  as a function of phase mismatch  $\Delta kL/2$  is given in Fig. 2.3.

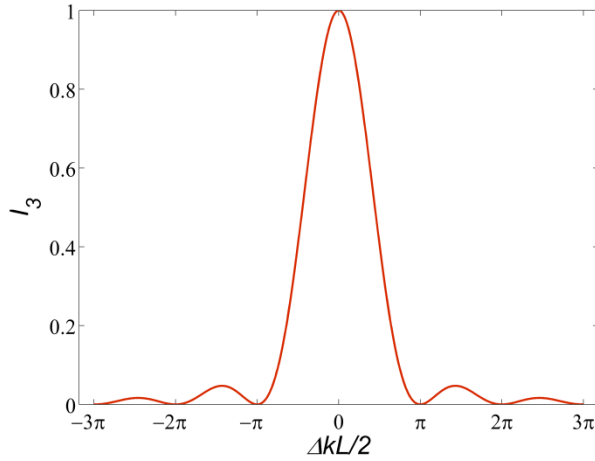


Fig. 2.3. Intensity of the generated wave as a function of the phase mismatch.

The intensity of the generated wave decreases when  $|\Delta kL/2|$  deviates from zero. The output wave gets out of phase with the driving polarization and power starts flowing back into the input waves over a characteristic propagation length, which is called the coherence length, and is defined as:

$$L_c = \frac{\pi}{\Delta k}. \quad (2.5.2)$$

The phase matching condition may in general be difficult to achieve due to the dispersion of the material. The conditions for efficient frequency conversion with collinearly propagating beams can be expressed as:

$$\frac{n_1\omega_1}{c} + \frac{n_2\omega_2}{c} - \frac{n_3\omega_3}{c} = 0, \quad (2.5.3)$$

$$\omega_1 + \omega_2 = \omega_3.$$

For SHG, the condition for perfect phase matching is:

$$n(\omega_1) = n(2\omega_1). \quad (2.5.4)$$

When the process is phase matched, the generated second harmonic intensity according to Eq. (2.5.1) is proportional to the square of the propagated distance,  $L$ . When the input beam intensity is high and the propagation length in the nonlinear medium is long, the conversion efficiency may become large and pump depletion can no longer be neglected. For a perfect phase matching, the intensities of the fundamental and second harmonic beams are [2.3]:

$$I_{\omega_1}(L) = I_{\omega_1}(0) \operatorname{sech}^2(GL), \quad (2.5.5)$$

$$I_{2\omega_1}(L) = I_{\omega_1}(0) \tanh^2(GL), \quad (2.5.6)$$

where  $G$  is defined as:

$$G = \sqrt{\frac{2\omega_1^2}{\epsilon_0 c^3} \frac{d_{eff}^2}{n^3} I_{\omega_1}(0)}. \quad (2.5.7)$$

Fig. 2.4 illustrates the intensity evolution during the SHG process with the propagation distance in the nonlinear medium.

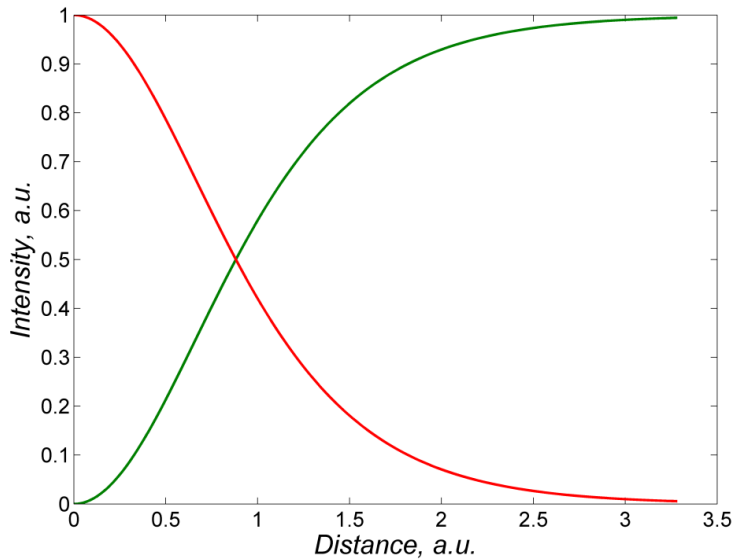


Fig. 2.4. Fundamental (red curve) and second harmonic (green curve) intensity as a function of the propagation length in the nonlinear medium for perfect phase matching case.

Uniform plane wave approximation predicts a total conversion of the fundamental wave into the second harmonic wave; however, in practice, the conversion efficiency may be limited by many factors, such as the laser-beam profile, beam quality, focusing conditions, etc. Often, second harmonic conversion efficiencies above 50% can be achieved, and under special conditions, e.g., with cavity enhancement, conversion efficiencies up to 90% are actually possible [2.4].

## 2.6. Birefringent phase matching

### 2.6. Birefringent phase matching

Birefringent phase matching (BPM) relies on the material property, called birefringence, in order to achieve efficient frequency conversion. As an example, we will consider SHG in a negative uniaxial crystal. The *ordinary wave* (i.e., the wave polarized perpendicular to the plane containing the optical axis of the crystal and the propagation direction), experiences the so-called ordinary refractive index,  $n_o$ , which stays the same regardless of the propagation direction. On the other hand, the *extraordinary wave* (i.e., the wave polarized in the plane containing the optical axis of the crystal and the propagation direction), experiences the index of refraction,  $n_e$ , which depends on the angle  $\theta$  between the optical axis and the propagation direction. From the ellipse equation, the angle-dependent index of refraction for the extraordinary wave can be determined by the following expression [2.5]:

$$n_e(\theta) = \frac{n_o \bar{n}_e}{\sqrt{n_o^2 - (n_o^2 - \bar{n}_e^2) \cos^2 \theta}}, \quad (2.6.1)$$

where  $\bar{n}_e$  is the principal value of the refractive index for the extraordinary wave.  $n_e(\theta) = \bar{n}_e$  for  $\theta = 90^\circ$  and  $n_e(\theta) = n_o$  for  $\theta = 0^\circ$ . For a negative uniaxial crystal,  $n_o > \bar{n}_e$ .

Within its transparency range, the nonlinear medium experiences normal dispersion: the refractive index of a higher frequency wave is larger. Fig. 2.5 shows the angular dependence of the index of refraction for the ordinary and the extraordinary waves, both for the fundamental and the second harmonic waves.

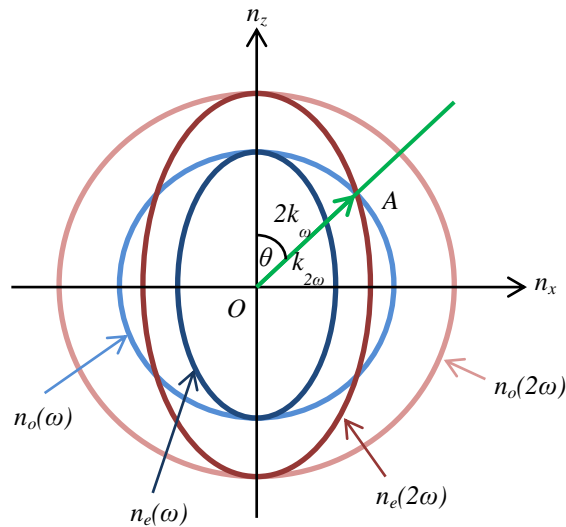


Fig. 2.5. The angular dependence of the index of refraction on the propagation direction for the ordinary and the extraordinary waves for second harmonic generation in negative uniaxial crystal.

It is obvious that in the direction OA, the phase matching condition for collinear SHG is fulfilled:

$$n_o(\omega) = n_e(2\omega). \quad (2.6.2)$$

Depending on the polarizations of the interacting waves, the different phase-matching schemes are grouped into two types: type I phase matching, in which the two lowest-frequency waves are polarized the same way; while in type II phase matching, their polarizations are orthogonal.

Although birefringent phase matching is a straightforward technique, it suffers from several issues. First, when the angle  $\theta$  is not  $0^\circ$  or  $90^\circ$ , the Poynting vector and the propagation vector are not parallel, resulting in a divergence between the ordinary and the extraordinary waves, which limits the conversion efficiency. This so-called walk-off effect, can be avoided by setting the angle  $\theta = 90^\circ$  and tuning the temperature, provided that the material's birefringence has a strong enough dependence on temperature. This is called noncritical phase matching. Second, since the nonlinearity is polarization dependent, it is not always possible to use the highest coefficient for a particular frequency conversion process. For instance, in KTP  $d_{33}$  cannot be used for frequency conversion using the BPM scheme. Moreover, the birefringence may be too weak to achieve phase matching in certain spectral regions. For instance, SHG involving type II phase matching is not possible for wavelengths below 1075 nm in KTA crystals [2.6].

## 2.7. Quasi-phase matching

Instead of relying on the material properties, quasi-phase matching (QPM) ensures efficient frequency conversion by artificially structuring the nonlinear medium. This technique is essentially free of the issues present in birefringent phase matching. QPM was first proposed in 1962 by Armstrong *et al.* [2.7], with the idea of SHG in a set of nonlinear crystals periodically oriented by  $180^\circ$ , with the length of each crystal along the propagation direction equal to the coherence length. In noncentrosymmetric crystals this results in the changing of the sign of the components of the nonlinearity tensor, and, subsequently, resetting the phase mismatch between the interacting waves. A more feasible and a widely used approach to achieve QPM is by periodically reversing the spontaneous polarization in a ferroelectric crystal. This process, called periodic poling, is usually done by applying an external electric field over a periodic electrode. Another approach for implementing QPM relies on growing orientation-patterned nonlinear materials, such as GaAs [2.8]. This thesis focuses on implementing QPM structures by periodic poling of the KTP-family materials.

The idea behind QPM is illustrated in Fig. 2.6. For perfect phase matching, given by the blue curve, the generated wave intensity grows quadratically with the propagation distance. If a phase mismatch is introduced, the generated wave intensity reaches the maximum point at one coherence length and starts coupling back into the input waves, as shown in the green curve. In the case of QPM, the phase difference between the interacting waves is reset every coherence length and efficient frequency conversion can be achieved, as shown in the red curve in Fig. 2.6.

## 2.7. Quasi-phase matching

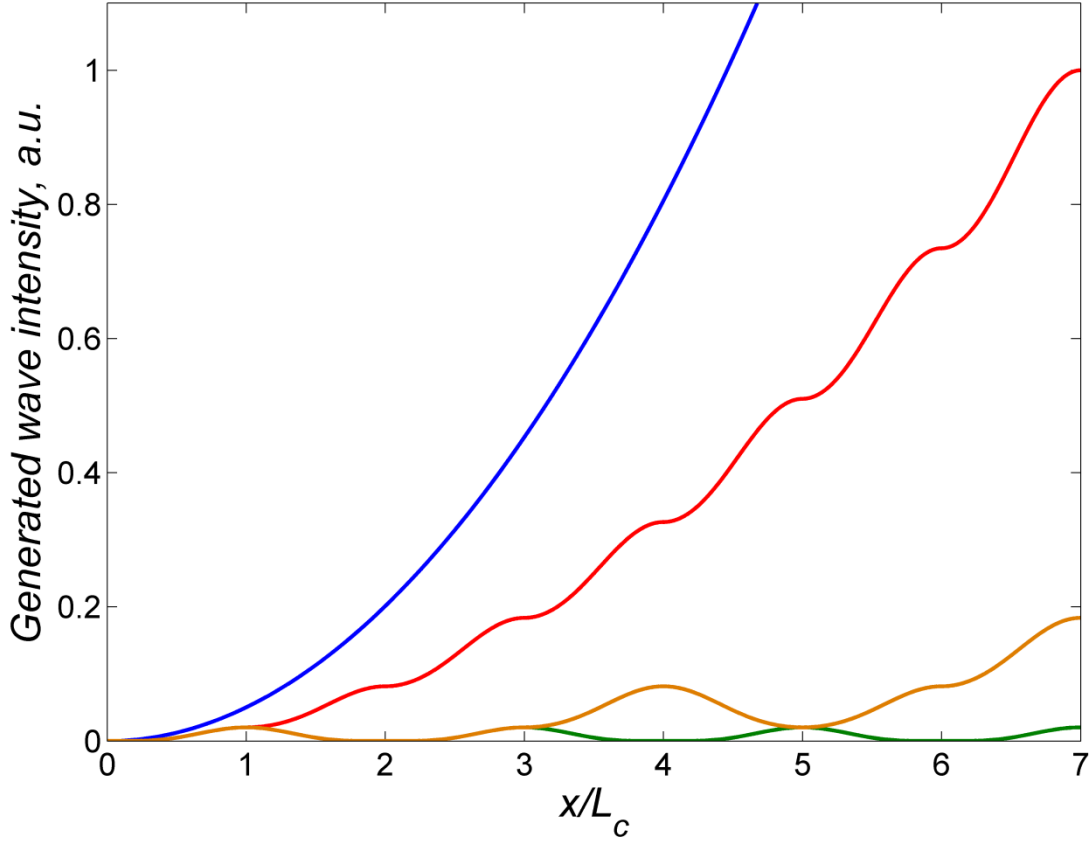


Fig. 2.6. Comparison of different phase matching conditions in a nonlinear frequency conversion process: blue – perfect phase matching, red – first order quasi-phase matching, orange – third order quasi-phase matching, green – no phase matching.

Quasi-phase matching can be implemented by spatially varying the nonlinear coefficient,  $d_{il}$ , in a periodic fashion. The spatial variation of the nonlinear coefficient,  $d(x)$ , can be described by a Fourier series:

$$d(x) = d_{il} \sum_{m=-\infty}^{\infty} G_m e^{ik_m x}, \quad (2.7.1)$$

where  $k_m$  is the magnitude of  $m^{\text{th}}$  order grating vector. In the case of a square-wave modulation of the nonlinear coefficient with a duty-cycle,  $D$ , the coefficients  $G_m$  can be defined as follows:

$$G_m = \frac{2}{m\pi} \sin(m\pi D). \quad (2.7.2)$$

The effective nonlinear coefficient is then defined as:

$$d_{eff} = d_{il} G_m. \quad (2.7.3)$$

Figure 2.7 shows the dependence of the effective nonlinear coefficient on the duty-cycle for orders  $m = 1, 2, 3$ .

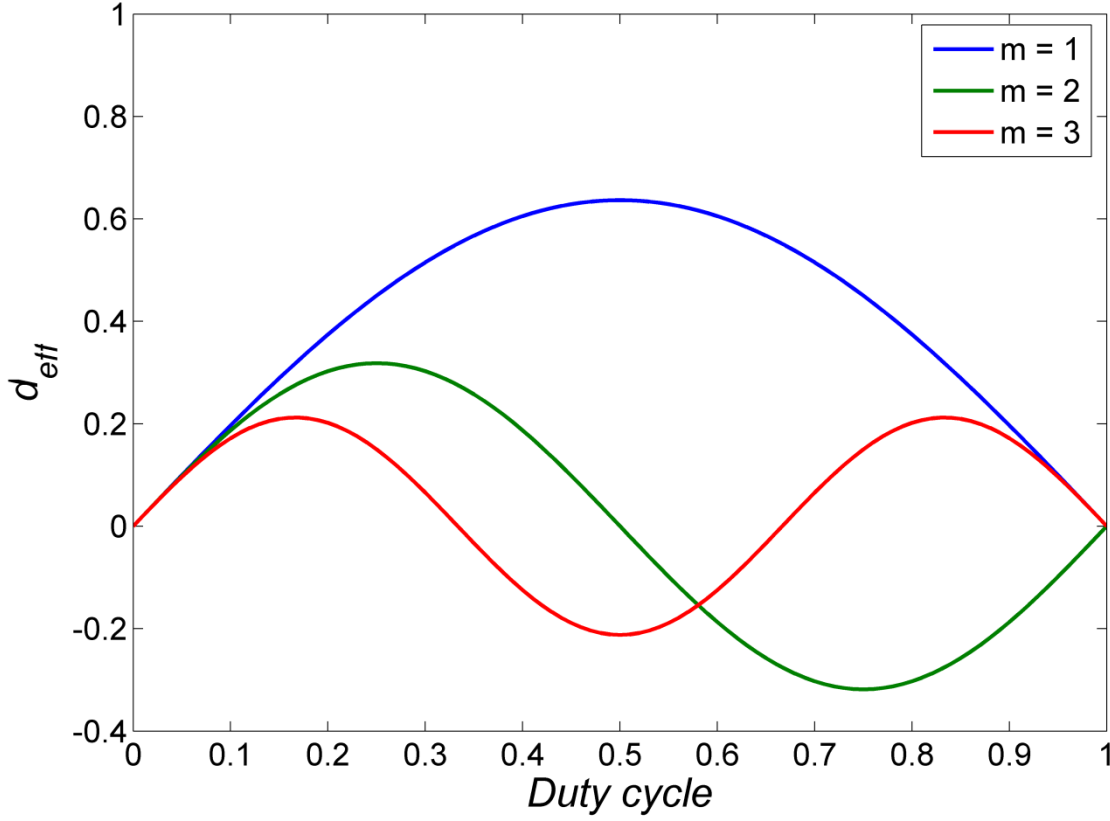


Fig. 2.7. Effective nonlinear coefficient (normalized to  $d_{ii}$ ) as a function of the duty-cycle for orders  $m = 1, 2, 3$ .

From Eqs. (2.7.2), (2.7.3) and Fig. 2.7 it is obvious that first order QPM, with a duty-cycle  $D = 0.5$  is the most desirable, since it gives the highest effective nonlinear coefficient.

Assuming that efficient coupling between the three interacting waves is dominated by a particular Fourier component,  $G_m$ , the coupled wave equations are:

$$\begin{aligned} \frac{dA_1}{dx} &= \frac{2i\omega_1 d_{eff}}{n_1 c} A_3 A_2^* e^{i\Delta k x}, \\ \frac{dA_2}{dx} &= \frac{2i\omega_2 d_{eff}}{n_2 c} A_3 A_1^* e^{i\Delta k x}, \\ \frac{dA_3}{dx} &= \frac{2i\omega_3 d_{eff}}{n_3 c} A_1 A_2 e^{-i\Delta k x}. \end{aligned} \quad (2.7.4)$$

The mismatch is given by:

$$\Delta k = k_3 - k_2 - k_1 - k_m, \quad (2.7.5)$$

where,

$$k_m = \frac{2m\pi}{\Lambda}. \quad (2.7.6)$$

## 2.8. QPM SHG tuning and tolerances

The optimal period for the most efficient frequency conversion depends on the material dispersive properties:

$$\Lambda = 2L_c = \frac{m}{\frac{n_3}{\lambda_3} \frac{n_2}{\lambda_2} \frac{n_1}{\lambda_1}}. \quad (2.7.7)$$

Even though the first order QPM reduces the nonlinearity with a factor of  $2/\pi$ , it can still be more efficient than birefringent phase matching, because the highest nonlinear coefficient can be utilized.

The main advantage of the QPM method is the flexibility that allows tailoring any nonlinear interaction within the material transparency range by appropriately designing the QPM structure. Additional advantages include noncritical phase matching, large acceptance angle, the possibility to implement multiple QPM nonlinear processes in a single crystal, etc. Of particular interest is the possibility of using QPM to realize nonlinear interactions involving counter propagating waves, which otherwise are impossible to obtain with BPM in the visible and near-infrared spectral range. Examples of such interactions are backward second harmonic generation (BSHG), broadband, counter-propagating optical parametric amplifiers, and mirrorless parametric oscillators (MOPO) [2.9]. The concept behind the BSHG is illustrated in Fig. 2.8.

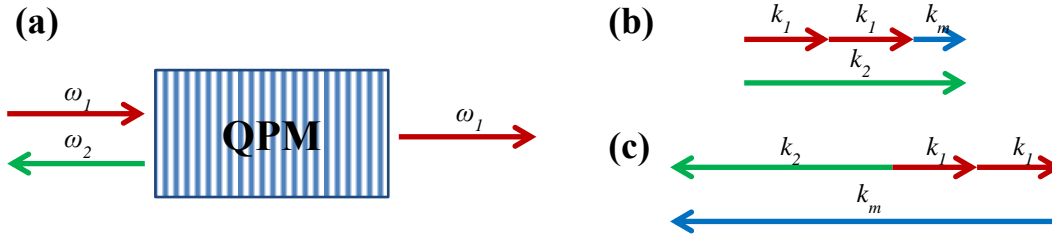


Fig. 2.8. Illustration of backward second harmonic generation (a), wave vector diagrams of collinear second harmonic generation (b), and collinear backward second harmonic generation (c).

The phase matching condition for this case can be expressed as:

$$\Delta k = 2k_1 + k_2 - k_m. \quad (2.7.8)$$

From Eqs. (2.7.6) and (2.7.8) it is obvious that the periods needed to realize BSHG, are much shorter than in the forward case. For example, the 1<sup>st</sup> order QPM SHG of 1064 nm in KTP requires a period of 9.01  $\mu\text{m}$ , whereas the period needed for 1<sup>st</sup> order BSHG is 143 nm. Such short periods are currently beyond the state of the art technology; however, the periods needed for MOPOs are on the order of several hundred nanometers, and are today achievable [2.10].

## 2.8. QPM SHG tuning and tolerances

The QPM SHG tuning and tolerances were thoroughly studied by Fejer *et al.* [2.11], and will now be summarized here. The QPM peak has the shape of  $\text{sinc}^2(\Delta kL/2)$ , with the phase matching factor  $\Delta kL/2 = 0.4429\pi$  at half maximum. This allows evaluating the full width at half maximum

(FWHM) acceptance bandwidths for parameters affecting the phase matching. The spectral acceptance bandwidth of the fundamental wavelength can be expressed as [2.11]:

$$\delta\lambda = \frac{0.4429\lambda}{L} \left| \frac{n_2 - n_1}{\lambda} + \frac{\partial n_1}{\partial \lambda} - \frac{1}{2} \frac{\partial n_2}{\partial \lambda} \right|^{-1}, \quad (2.8.1)$$

where the derivatives are evaluated at their respective wavelengths. It is worth noting that the spectral acceptance bandwidth tends to increase towards longer wavelengths because of the decrease in the dispersion.

The FWHM angular acceptance for a noncritically phase matched interaction in an isotropic medium is given by [2.11]:

$$\delta\theta = 2 \sqrt{1.772 \frac{n_2 L_c}{n_1 L} \cos\theta}. \quad (2.8.2)$$

The refractive indices of the material are temperature dependent. In addition, the thermal expansion alters the period and the length of the QPM structure when the temperature of the nonlinear medium is changed. The temperature acceptance bandwidth can be expressed as [2.11]:

$$\delta T = \frac{0.4429\lambda}{L} \left| \frac{\partial n_2}{\partial T} - \frac{\partial n_1}{\partial T} + \alpha(n_2 - n_1) \right|^{-1}, \quad (2.8.3)$$

where  $\alpha$  is the thermal expansion coefficient. The temperature acceptance bandwidth increases towards longer wavelengths. The indices of refraction and their temperature dependencies are obtained from Sellmeier equations for a particular nonlinear material. From the temperature acceptance bandwidth, an effective QPM grating length can be estimated, which is a good measure of the quality of the QPM structure. The QPM structure is considered to be of high quality when the calculated effective length is equal to the physical grating length,  $L$ .

## 2.9. Optimal focusing with Gaussian beams

Most commonly, lasers have a Gaussian spatial intensity distribution. The diffraction of a focused Gaussian beam limits the interaction length during second harmonic generation, therefore an optimal focusing condition exists, which is essentially a tradeoff between the focused beam intensity and the interaction length in the nonlinear medium. A theory, developed by Boyd and Kleinman [2.12], defines the focusing parameter:

$$\xi = \frac{L}{b}, \quad (2.9.1)$$

where  $L$  is the crystal length, and  $b = 2\pi w_0^2/\lambda$  is the so-called confocal parameter. The second harmonic conversion efficiency can be expressed as:

$$\eta = \frac{2d_{eff}^2 \omega_1^2 k_1 P_1}{\pi \epsilon_0 n_1^2 n_2 c^3} Lh(B, \xi), \quad (2.9.2)$$

## 2.10. Optical parametric oscillators

where  $d_{eff}$  is the effective nonlinear coefficient,  $\omega_1$ ,  $k_1$ ,  $P_1$  and  $n_1$  – the frequency, wavevector, power and the index of refraction of the fundamental beam,  $n_2$  – the index of refraction of the second harmonic beam,  $c$  – the speed of light,  $\epsilon_0$  – the permittivity of free space, and  $h(B, \zeta)$  is the Boyd-Kleinman focusing factor. For QPM (no walk-off,  $B = 0$ ), the maximum nonlinear interaction is specified by the focusing parameter  $\xi_m = 2.84$ , and the focusing factor  $h(0, \xi_m) = 1.068$ . The adjustment with respect to  $\zeta$  is not a very critical factor, since the second harmonic efficiency stays within 10% of its maximum value in the range  $1.52 \leq \zeta \leq 5.3$ . From Eq. (2.9.2), it is obvious that the conversion efficiency increases linearly with the fundamental power and the nonlinear crystal length. In order to compare the performance of different QPM devices, the conversion efficiency is normalized with respect to the length of the nonlinear medium and the power of the fundamental beam:

$$\eta_{norm} = \frac{\eta}{P_1 L} = \frac{2d_{eff}^2 \omega_1^2 k_1}{\pi \epsilon_0 n_1^2 n_2 c^3} h(B, \xi). \quad (2.9.3)$$

The normalized conversion efficiency is usually evaluated in the low power regime.

The effective nonlinear coefficient can be used as a quality measure of the QPM structure and is defined as:

$$d_{eff} = \sqrt{\frac{\pi \epsilon_0 c^3 n_1^2 n_2 P_2 m^2}{2 \omega_1^2 k_1 P_1^2 h(B, \xi)}}, \quad (2.9.4)$$

where  $m$  is the QPM order.

## 2.10. Optical parametric oscillators

In difference frequency generation, a strong input signal at frequency  $\omega_p$  interacts with a weak signal at frequency  $\omega_s$ , and, as a consequence, the signal at frequency  $\omega_s$  gets amplified and a signal at frequency  $\omega_i$  is generated (Fig. 2.9(a)). The power, coupled to the signal and the idler waves from the pump, is governed by Manley-Rowe relations [2.1]:

$$\frac{I_p}{\omega_p} = -\frac{I_s}{\omega_s} = -\frac{I_i}{\omega_i}, \quad (2.10.1)$$

where  $I_p$ ,  $I_s$  and  $I_i$  denote the intensities of the pump, the signal and the idler waves, respectively. Since the difference frequency mixing is an amplification process, the coupling between the signal and the idler must be considered. For undepleted pump and with a strong gain, the signal and the idler intensities are respectively given by:

$$I_s(L) = I_s(0) \cosh^2(gL), \quad (2.10.2)$$

$$I_i(L) = I_s(0) \frac{\omega_i}{\omega_s} \sinh^2(gL). \quad (2.10.3)$$

Here,  $g$  is the gain coefficient:

$$g^2 = \frac{2\omega_s\omega_i d_{eff}^2 l_p}{\varepsilon_0 n_p n_s n_i c^3}. \quad (2.10.4)$$

In an OPO, the nonlinear medium is placed into an optical cavity providing feedback of the generated waves. The simplest OPO configuration is a linear cavity (Fig. 2.9(b)), where the input coupler is a highly reflective mirror and the output coupler is a partially reflective mirror for the signal and/or the idler waves.

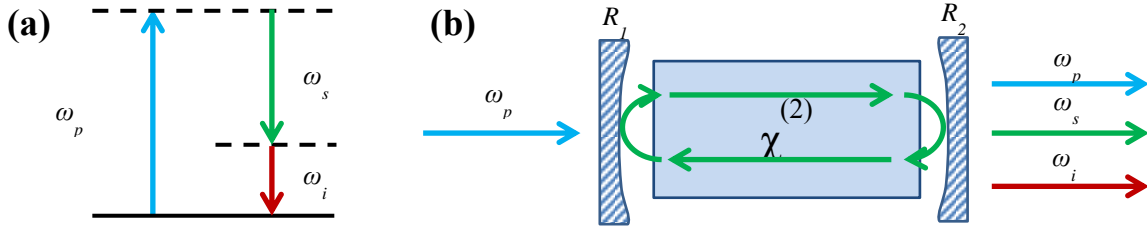


Fig. 2.9. Energy level diagram of difference frequency generation process (a) and optical parametric oscillator linear cavity (b).

If the resonator mirrors are reflective at  $\omega_s$  or  $\omega_i$ , the device is called singly resonant OPO. When the mirrors are reflective at  $\omega_s$  and  $\omega_i$ , the device is a doubly resonant OPO. The operational threshold for a doubly resonant OPO is usually lower than that for a singly resonant OPO. Nevertheless, singly resonant OPOs are predominantly used due to their superior stability and tuning characteristics. For a singly resonant OPO, the oscillation occurs at the cavity mode closest to the gain peak, whereas for a doubly resonant OPO, the oscillation is supported by both modes corresponding to the signal and the idler, which may not necessarily be closest to the gain peak. Consequently, small fluctuations in the pump frequency or the cavity length can lead to large variations in the output frequencies of a doubly resonant OPO.

Any pair of signal and idler frequencies, satisfying the condition  $\omega_p = \omega_s + \omega_i$ , can be generated by an OPO. The OPO tuning can be accomplished by setting the phase matching condition  $\Delta k = 0$  for any pair of frequencies  $\omega_s$  and  $\omega_i$ . The most popular way to tune OPOs employing QPM is by changing the temperature of the nonlinear medium. Other methods include the use of noncolinear geometries, multiple gratings, fan-shaped gratings and a variation of the QPM period by rotating the QPM grating [2.13].

## References

- 2.1. R. W. Boyd, *Nonlinear optics* (Academic Press, 2008).
- 2.2. D. A. Kleinman, "Nonlinear dielectric polarization in optical media," *Phys. Rev.* **126**, 1977 (1962).
- 2.3. P. N. Butcher, and D. Cotter, *The elements of nonlinear optics* (Cambridge University Press, 1998).
- 2.4. T. Sudmeyer, Y. Imai, H. Masuda, N. Eguchi, M. Saito, and S. Kubota, "Efficient 2<sup>nd</sup> and 4<sup>th</sup> harmonic generation of a single-frequency, continuous-wave fiber amplifier," *Opt. Express* **16**, 1546-1551 (2008).
- 2.5. Дмитриев В. Г., Тарасов Л. В., *Прикладная нелинейная оптика: Генераторы второй гармоники и параметрические генераторы света* (Радио и связь, 1982).
- 2.6. J. D. Bierlein, H. Vanherzeele, and A. A. Ballman, "Erratum: "Linear and nonlinear optical properties of flux-grown KTiOAsO<sub>4</sub>,"" *Appl. Phys. Lett.* **61**, 3193 (1992).
- 2.7. J. A. Armstrong, N. Bloembergen, J. Ducuing, and P. S. Pershan, "Interactions between light waves in a nonlinear dielectric," *Phys. Rev.* **127**, 1918 (1962).
- 2.8. C. B. Ebert, L. A. Eyres, M. M. Fejer, and J. S. Harris, Jr., "MBE of antiphase GaAs films using GaAs/Ge/GaAs heteroepitaxy," *J. Crystal Growth*, **201/202**, 187 (1999).
- 2.9. S. E. Harris, "Proposed backward wave oscillation in the infrared," *Appl. Phys. Lett.* **9**, 114 (1996).
- 2.10. C. Canalias, and V. Pasiskevicius, "Mirrorless optical parametric oscillator," *Nature photon.* **1**, 459 (2007).
- 2.11. M. M. Fejer, G. A. Magel, D. H. Jundt, and R. L. Byer, "Quasi-phase-matched second harmonic generation: tuning and tolerances," *IEEE J. Quantum Electron.* **28**, 2631 (1992).
- 2.12. G. D. Boyd, and D. A. Kleinman, "Parametric interaction of focused Gaussian light beams," *J. Appl. Phys.* **39**, 3597 (1968).
- 2.13. J. P. Feve, O. Pacaud, B. Boulanger, B. Menaert, J. Hellström, V. Pasiskevicius, and F. Laurell, "Widely and continuously tunable optical parametric oscillator based on a cylindrical periodically poled KTiOPO<sub>4</sub> crystal," *Opt. Lett.* **26**, 1882 (2001).

## Chapter 3. Ferroelectrics

### 3.1. Crystal symmetry

A crystalline solid consists of atoms which have a regular arrangement that exhibits translational symmetry. An ideal crystal can be defined as being defectless and with the atoms taking equilibrium positions in the crystal lattice. For simplicity, we can assume that ideal crystals are also of infinite dimensions. Ideal crystals exhibit many types of symmetries, which determine many of their properties. The crystal symmetry operations are those that project the crystal back onto itself. Examples of such symmetry operations are translations, rotations, and reflections. These operations are called point transformations since they leave at least one crystal lattice point fixed. A collection of such point transformations form groups, called point groups. There are only 32 different point groups that are allowed by translational symmetry [3.1]. In the international (Herman-Mauguin) notation, the rotation axes are denoted by a number  $n$  (angle of rotation is  $2\pi/n$ ). The rotation inversion axes are denoted by the corresponding number with the macron symbol  $\bar{n}$ . The mirror plane, with its direction being normal to the plane, is denoted by the symbol  $m$ . If the rotation axis and a mirror plane have the same direction, they are denoted as the fraction  $n/m$ . If the notation contains three positions, then they denote symmetry operations in the  $z$ -,  $y$ -,  $x$ - directions, respectively. For example, KTP belongs to the point group  $2mm$ , which means that it has a two-fold rotation axis along the polar  $z$ - direction (angle of rotation  $\pi$ ), and two mirror planes along the  $x$ - and the  $y$ - directions.

Table 3.1 shows the seven basic crystal systems with the 32 point groups as their subdivisions. These seven crystal systems, based on their optical properties, can be subdivided into three groups: biaxial, uniaxial and isotropic.

**Table 3.1. The seven crystal systems with corresponding point groups and optical groups. The polar point groups are given in bold.**

Crystal system	Point group	Optical group
Triclinic	<b>1</b>	Biaxial
	$\bar{1}$	
Monoclinic	<b>2</b>	Biaxial
	<b><i>m</i></b>	
	$(2/m)$	
Orthorhombic	<b>222</b>	Biaxial
	<b><i>2mm</i></b>	
	$(2/m)(2/m)(2/m)$	
	$(2/m)(2/m)(2/m)$	
Tetragonal	<b>4</b>	Uniaxial
	$\bar{4}$	
	$(4/m)$	
	<b>422</b>	
	<b><i>4mm</i></b>	
	$\bar{4}2m$	
$(4/m)(2/m)(2/m)$		

### 3.2. Ferroelectric materials

Trigonal	<b>3</b>	Uniaxial
	$\bar{3}$	
	32	
	<b>3m</b>	
Hexagonal	$\bar{3}(2/m)$	Uniaxial
	<b>6</b>	
	$\bar{6}$	
	(6/m)	
	622	
	<b>6mm</b>	
	$\bar{6}m2$	
(6/m)(2/m)(2/m)		
Cubic	23	Isotropic
	(2/m) $\bar{3}$	
	432	
	$\bar{4}3m$	
	(4/m)( $\bar{3}$ )(2/m)	

### 3.2. Ferroelectric materials

Ferroelectricity is strongly related to the crystal structure of the material. The relation between the crystal point groups and their polarization properties are shown in Fig. 3.1. Eleven point groups out of the 32 are centrosymmetric, and 21 are noncentrosymmetric. The absence of inversion symmetry is a requirement for piezoelectricity. One of the 21 noncentrosymmetric point groups exhibits other symmetry elements and is not piezoelectric, while the other 20 point groups are piezoelectric. If a mechanical stress is applied to a piezoelectric crystal along certain directions, it exhibits an electric polarization proportional to the applied stress. On the other hand, if an electric field is applied across such crystal, it expands or contracts proportionally to the applied field. Ten of the 20 piezoelectric point groups are polar: they exhibit a nonvanishing dipole moment per unit volume – the so-called spontaneous polarization. The ten polar classes are:  $1$ ,  $2$ ,  $m$ ,  $2mm$ ,  $4$ ,  $4mm$ ,  $3$ ,  $3m$ ,  $6$  and  $6mm$  [3.2]. An electric charge can be created on the surface of the polar crystal if it is heated or cooled, since the external or internal conductivity in general cannot provide enough current to screen the change of the spontaneous polarization with temperature. This effect is called pyroelectricity. Ferroelectric materials are a subgroup of the pyroelectric class, and therefore they also exhibit pyroelectric and piezoelectric properties. A material is classified as ferroelectric, if it possesses a spontaneous polarization over a certain range of temperatures that can be reversed or reoriented by applying an external electric field [3.3].

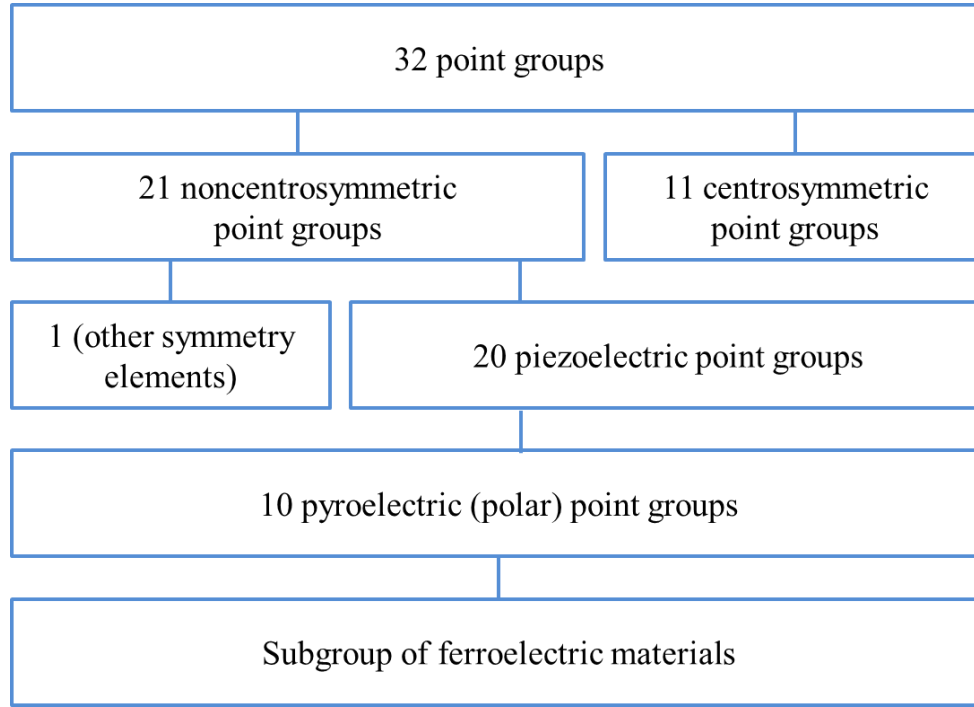


Fig. 3.1. Relationship between the crystal point groups and their polarization properties.

The temperature at which the ferroelectric material undergoes a structural phase transition to a higher symmetry paraelectric phase is called the Curie temperature. The ferroelectric phase can be considered as a modification of the higher symmetry paraelectric phase of the same crystal. Ferroelectric phase transitions are defined as first order transitions when the spontaneous polarization vanishes abruptly at the Curie temperature. When the spontaneous polarization decreases smoothly to the vanishing point, the phase transition is defined as a second order phase transition [3.3]. In KTP, a second order phase transition from the paraelectric to the ferroelectric phase occurs at a temperature  $T_c \approx 934 \text{ }^\circ\text{C}$  [3.4].

Phenomenologically, the ferroelectric phase can be described using a polynomial thermodynamic potential. Most commonly, the elastic Gibbs function with independent variables of temperature, stress and polarization is used. Under the assumptions that the spontaneous polarization occurs along the direction of the applied electric field, all stresses are zero, and the non-polar phase is centrosymmetric, the free Gibbs energy can be expressed in the following polynomial form:

$$G = G_0 + \frac{\alpha}{2} P^2 + \frac{\beta}{4} P^4 + \frac{\gamma}{6} P^6, \quad (3.2.1)$$

where  $\alpha$ ,  $\beta$ , and  $\gamma$  are temperature dependent coefficients and  $P$  is the polarization. Differentiating Eq. (3.2.1) with respect to  $P$  gives the equation of state:

$$E = \alpha P + \beta P^3 + \gamma P^5, \quad (3.2.2)$$

### 3.2. Ferroelectric materials

where  $E$  is the electric field. The extremum points of the Gibbs function are determined solving Eq. (3.2.2) for  $E = 0$ . Figure 3.2 shows the Gibbs free energy as a function of  $P$  for the three cases:  $T > T_c$ ,  $T = T_c$ , and  $T < T_c$ .

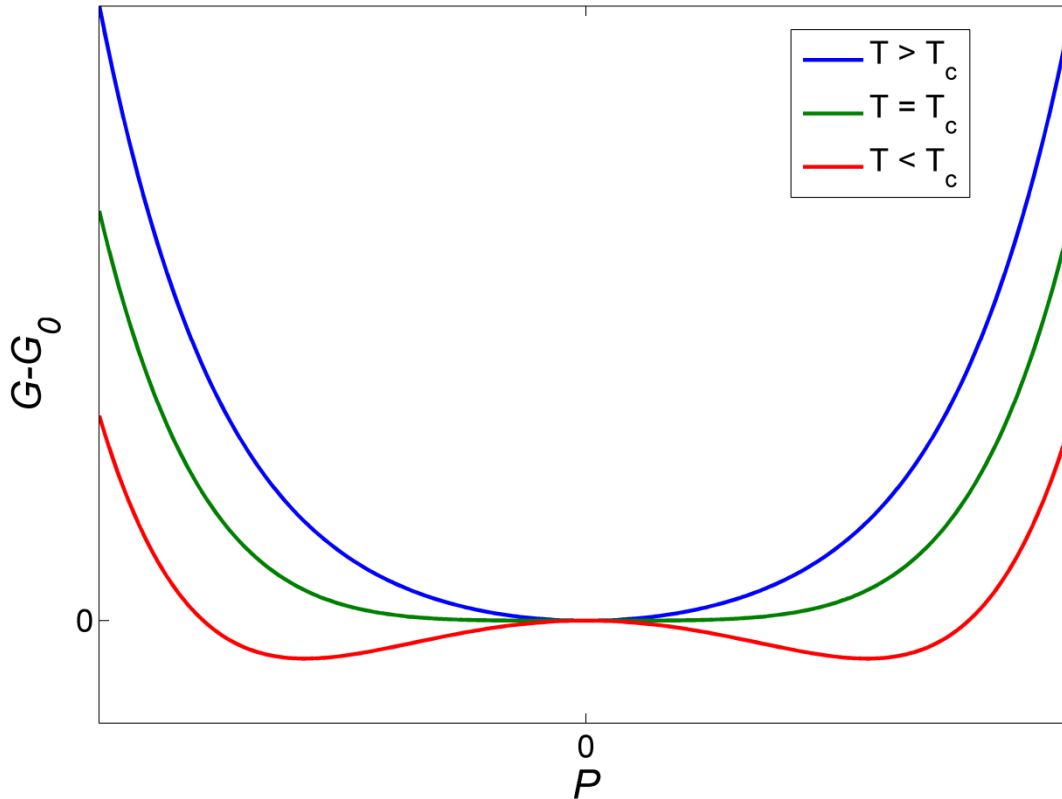


Fig. 3.2. The free Gibbs energy as a function of polarization above, at, and below the Curie temperature.

From Fig. 3.2 it is clear that only one Gibbs potential minimum exists in the paraelectric phase, while in the ferroelectric phase, two minima appear, corresponding to the equilibrium values of the spontaneous polarization  $P_s$ . It is worth noting that this thermodynamic approach allows describing important properties of ferroelectrics taking into account purely symmetry considerations, but neglecting the physical mechanisms behind ferroelectricity.

At constant temperature, Eq. (3.2.2) also defines a hysteresis loop, which is a significant property of all ferroelectric materials. A typical hysteresis loop is illustrated in the Fig. 3.3. At large electric fields, the polarization is saturated, and all dipoles in the material are oriented along the direction of the electric field. If the electric field is decreased to zero, the polarization reaches a non-zero value, called remnant polarization  $P_r$ .  $P_r$  may be smaller than the saturated polarization,  $P_{sat}$ , since some domains may return to the reversed state due to e.g. the presence of internal stress in the crystal. The remnant polarization is equal to the saturated polarization in a single-domain ferroelectric crystal. The magnitude of the electric field needed to change the polarization from  $P_r$  to zero, is called the coercive field,  $E_c$ . The coercive field depends on many

parameters, such as the temperature, pressure, frequency and the waveform of the applied field, electrodes, crystal history, etc.

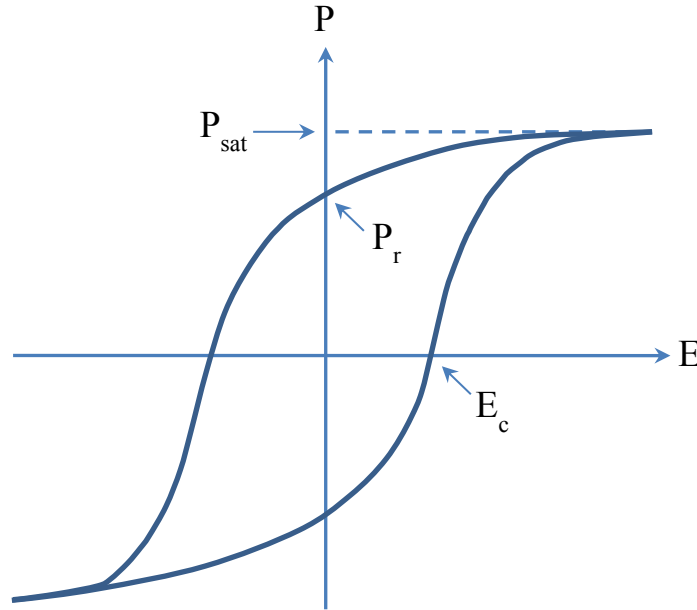


Fig. 3.3. Typical hysteresis loop of a ferroelectric material, showing the spontaneous polarization, remnant polarization and the coercive field.

Polarization switching is the process in which an electric field opposite to the spontaneous polarization and with a magnitude exceeding that of the coercive field is applied to a ferroelectric crystal to change the direction of the spontaneous polarization.

The electric displacement, the electric field and the polarization are connected via the following relation:

$$\mathbf{D} = \epsilon_0 \mathbf{E} + \mathbf{P}. \quad (3.2.3)$$

The displacement field is a consequence of the polarizability of the material in an external electric field and the net spontaneous polarization. Gauss's law in differential form states:

$$\nabla \cdot \mathbf{D} = \rho, \quad (3.2.4)$$

where  $\rho$  is the free charge density. From Eqs. (3.2.3) and (3.2.4):

$$\nabla \cdot \mathbf{E} = \frac{1}{\epsilon \epsilon_0} (\rho - \nabla \cdot \mathbf{P}_s). \quad (3.2.5)$$

In an ideal, infinite ferroelectric crystal, the spontaneous polarization is uniform,  $\nabla \cdot \mathbf{P}_s = 0$ . Therefore  $\nabla \cdot \mathbf{E} = \frac{\rho}{\epsilon \epsilon_0}$ . In real ferroelectric crystals, however,  $\nabla \cdot \mathbf{P}_s \neq 0$  at the crystal surfaces or in the bulk of the material due to defects, and, therefore, gives rise to an electric field, antiparallel to the spontaneous polarization, which is called the depolarization field [3.5]. The depolarization field can be compensated for by the flow of the internal free charges in the crystal. Alternatively, the depolarization field can also be compensated by free charges present in the crystal

### 3.3. Polarization reversal

environment. When the surface charge is accumulated, the electric field is zero both in the bulk and outside of the ferroelectric crystal, but not just below the surfaces of the crystal.

When a crystal is cooled down from the paraelectric phase to the ferroelectric phase, the direction of the spontaneous polarization can take two alternative values. Different regions of the crystal can be polarized along the opposite directions and form ferroelectric domains in order to minimize the energy associated with the depolarization field. A ferroelectric domain can be defined as a crystal region with a homogeneous spontaneous polarization [3.3]. The region in the crystal, which separates two domains with antiparallel spontaneous polarization directions, is called a domain wall. The ferroelectric domain structure is stable when the depolarization energy and the domain wall energy are at their minimum values.

### 3.3. Polarization reversal

It is accepted that the polarization reversal in ferroelectrics involves the following steps: domain nucleation, domain growth along the polar axis, sideways expansion and coalescence of the domains. Most commonly, domain nucleation is modelled as a statistical process with the probability depending exponentially on the applied external electric field [3.6]. The theory of the domain nucleation was first formulated by Merz [3.7] and further expanded by Landauer [3.8]. When a new domain is nucleated, the total energy change is given by:

$$\Delta W = W_w + W_E - \mathbf{D} \cdot \mathbf{E}V, \quad (3.3.1)$$

where  $W_w$  represents the domain wall energy,  $W_E$  is the depolarization energy of the nucleus, and  $\mathbf{D} \cdot \mathbf{E}V$  is the electrostatic energy of the nucleus of volume  $V$  in the applied electric field. Assuming that both the polarization and the local electric field within the nucleus are uniform, the rate of domain nucleation is proportional to  $\exp(-\Delta W/kT)$ . The Landauer theory predicts a critical nucleus energy that is unrealistically large (on the order of  $10^8 kT$ ) [3.9]. Experimentally, however, switching can be observed at fields lower than the estimated thermodynamic coercive field. Since the Landauer model assumes an ideal insulating ferroelectric crystal containing no free carriers or defects, defect-assisted nucleation models were proposed by Janovec [3.10] and Molotskii *et al.* [3.11]. The most accepted domain nucleation model today, proposed by Gerra *et al.* [3.12], extends the Landauer model by including the ferroelectric-electrode coupling and defects in the ferroelectric-electrode interface. In this model the domains of the shape of prolate semispheroids are considered. The total energy change associated with the nucleation of a new domain now includes the ferroelectric-electrode interface energy, and can be expressed as:

$$\Delta W = W_w + W_E - \mathbf{D} \cdot \mathbf{E}V - \pi \xi P_s r^2, \quad (3.3.2)$$

where  $r$  is the base radius of the domain, and  $\xi$  represents the local surface field.

The ferroelectric domain growth is anisotropic in the three dimensions. The domain forward growth velocity (along the polar direction) is usually much larger than lateral growth velocities, and follows an inverse exponential dependence on the applied electric field [3.9]. The domain wall velocity along the polar direction in the KTP isomorphs is at least a few orders of magnitude

higher than that in the lateral directions [3.13]. It is important to point out that due to the measurement difficulties the problem of the domain forward growth velocity in ferroelectrics still remains an open question.

A domain sideways expansion mechanism through a lateral domain wall motion is unlikely [3.5]. Miller and Weinreich explained the domain sideways expansion via the nucleation at the crystal surface and the propagation of step-like domains adjacent to the existing domain walls [3.14]. The most energetically favorable shape of a step-like domain forming adjacent to an existing domain wall is triangular, as shown in Fig. 3.4. Thus, the domain sideways expansion speed depends on the rate of nucleation and the growth velocity of such step-like domains.

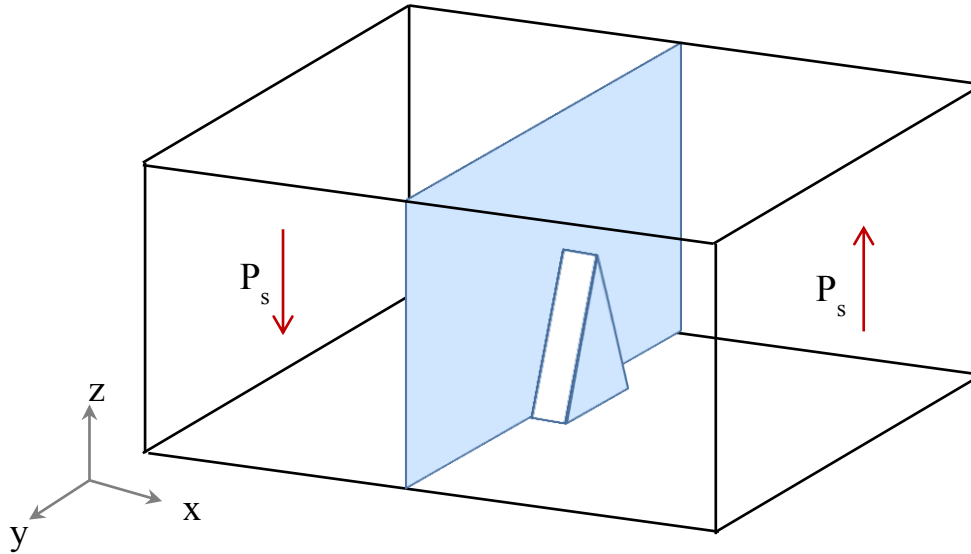


Fig. 3.4. Schematic representation of a triangular, step-like domain adjacent to an existing domain wall. The applied electric field is parallel to the  $z$  axis (adapted from [3.14]).

$\text{BaTiO}_3$  is considered to be a model ferroelectric in many aspects of polarization switching and domain dynamics. This material is the most studied experimentally, and the obtained results can be generalized to other ferroelectric crystals. The temporal dependence of the polarization switching on the electric field magnitude was first determined experimentally by Merz in  $\text{BaTiO}_3$  by applying electric field pulses and measuring the transient current as a function of time [3.7]. The switching time is defined as the time needed to complete the switching process under a given applied external electric field. For convenience, it is taken as the time measured from the beginning of the electric field pulse until the switching current drops to 5% of its maximum value. For  $\text{BaTiO}_3$ , in low fields (below  $E_c$ ) the switching time follows an exponential dependence:

$$t_s \sim \exp\left(\frac{\alpha}{E}\right), \quad (3.3.3)$$

where  $\alpha$  is the activation field. Domain wall motion evaluation by Miller and Savage in  $\text{BaTiO}_3$  revealed that the sideways domain wall velocity at low fields also shows an exponential dependence [3.15]:

### 3.4. Role of defects

$$v = v_{\infty} \exp\left(-\frac{\delta}{E}\right), \quad (3.3.4)$$

where  $v_{\infty}$  and  $\delta$  are parameters independent of the applied electric field. At higher fields (above  $E_c$ ) the switching time dependence follows a power-law [3.16]:

$$t_s \sim E^{-n}, \quad (3.3.5)$$

where  $n$  is the material-dependent parameter. Stadler and Zachmanidis demonstrated that in the high field range, the domain wall velocity in BaTiO<sub>3</sub> has the following dependence [3.17]:

$$v \sim E^n, \quad (3.3.6)$$

which is consistent with Eq. (3.3.5). Assuming an exponential nucleation rate dependence on the electric field, the polarization switching behavior can be understood as nucleation-dominated in the low field regime, while at high fields, the nucleation is not a limiting factor any more, and, therefore, switching is governed by the domain wall motion. It is important to note that even though this model is based on the studies of BaTiO<sub>3</sub>, the existence of the different stages of domain evolution is general for most ferroelectric crystals, with the exponential dependence being characteristic for low electric fields, while the behavior at high fields is material-specific. Indeed, a similar polarization switching behavior is reported for KTP by Rosenman *et al.* [3.18], Urenski *et al.* [3.19], and Canalias *et al.* [3.13], distinguishing a nucleation-dominated regime at low fields, whereas at high fields, the switching rate is controlled by the domain wall motion.

In principle, polarization switching using short electric field pulses is feasible provided that the electric field magnitude is large enough. However, Fatuzzo and Merz have experimentally showed that there is a critical pulse duration,  $t^*$ , below which there is no net reversal of the spontaneous polarization [3.20]. The physical mechanism behind this phenomenon is not yet fully understood [3.6]. Fatuzzo and Merz suggested that the time  $t^*$  may be associated with the time needed to form critical nuclei [3.20], whereas Gopalan and Mitchell attributed it to domain stabilization time and backswitching [3.21].

### 3.4. Role of defects

The existence of a defect causes deformations in the crystal lattice and thus modifies the local fields. The extent of these effects depends on the parameters such as the type and the location of the defect and the defect-host interaction. An accentric defect creates a dipole moment [3.5]:

$$\overline{\Delta\mu} = \Delta\mu_d + \sum_i q_i \Delta x_i, \quad (3.4.1)$$

where  $\Delta\mu_d$  is the change in the dipole moment and  $\Delta x_i$  is the displacement of the charge  $q_i$  in the surrounding lattice due to the defect. The interaction between different defects can be neglected if the defect concentration  $N$  is sufficiently small. The change in the macroscopic polarization can be described by the following expression:

$$\Delta P = N \overline{\Delta\mu}. \quad (3.4.2)$$

The polarization contribution due to the defects  $\Delta P$  may or may not reverse when the polarization of the ferroelectric crystal is reversed by an external electric field. If it reverses, the hysteresis loop may become biased, i.e., the coercive field will be dependent on the field required to reverse the dipoles associated with the defects. If it does not reverse, it may act as initial nucleation sites during the polarization reversal, or may be the source of backswitching.

Domain wall pinning may also have a considerable impact on the polarization switching. The domain wall becomes pinned when, under an applied external electric field, its motion is hindered by the coupling of the domain wall with defects in the crystal [3.9]. Defects impose a pinning potential that needs to be overcome in order to enable the motion of the domain wall through the pinning point. Depinning requires either a larger electric field magnitude or a longer pulse duration. This effect can influence the quality of the QPM grating during the periodic poling process, therefore the use of high quality crystals with low defect concentrations is always desirable.

## References

- 3.1. J. Patterson and B. Bailey, *Solid-State Physics*, (Springer-Verlag, 2010).
- 3.2. K. C. Kao, *Dielectric Phenomena in Solids*, (Academic Press, 2004).
- 3.3. ANSI/IEEE std. 180-1986, *IEEE Standard Definitions of Primary Ferroelectric Terms*, The Institute of Electrical and Electronics Engineers, Inc., (New York, 1986).
- 3.4. V. K. Yanovskii, and V. I. Voronkova, "Ferroelectric Phase Transitions and Properties of Crystals of the  $\text{KTiOPO}_4$  Family," *Phys. Status Solidi* **93**, 665-668 (1986).
- 3.5. M. E. Lines, and A. M. Glass, *Principles and Applications of Ferroelectrics and Related Materials*, (Oxford University Press, 1977).
- 3.6. T. Volk and M. Wöhlecke, *Lithium Niobate. Defects, Photorefraction and Ferroelectric Switching*, (Springer-Verlag, 2008).
- 3.7. W. J. Merz, "Domain Formation and Domain Wall Motions in Ferroelectric  $\text{BaTiO}_3$  Single Crystals," *Phys. Rev.* **95**, 690-698 (1954).
- 3.8. R. Landauer, "Electrostatic Considerations in  $\text{BaTiO}_3$  Domain Formation during Polarization Reversal," *J. Appl. Phys.* **28**, 227-234 (1957).
- 3.9. A. K. Tagantsev, L. E. Cross, and J. Fousek, *Domains in Ferroic Crystals and Thin Films*, (Springer-Verlag, 2010).
- 3.10. V. Janovec, "Anti-parallel ferroelectric domains in surface space-charge layers of  $\text{BaTiO}_3$ ," *Czech. J. Phys.* **9**, 468-480 (1959).
- 3.11. M. Molotskii, R. Kris, and G. Rosenman, "Fluctuon effects in ferroelectric polarization switching," *J. Appl. Phys.* **88**, 5318-5327 (2000).
- 3.12. G. Gerra, A. K. Tagantsev, and N. Setter, "Surface-Stimulated Nucleation of Reverse Domains in Ferroelectrics," *Phys. Rev. Lett.* **94**, 107602 (2005).
- 3.13. C. Canalias, J. Hirohashi, V. Pasiskevicius, and F. Laurell, "Polarization-switching characteristics of flux-grown  $\text{KTiOPO}_4$  and  $\text{RbTiOPO}_4$  at room temperature," *J. Appl. Phys.* **97**, 124105 (2005).
- 3.14. R. C. Miller and G. Weinreich, "Mechanism for the Sidewise Motion of  $180^\circ$  Domain Walls in Barium Titanate," *Phys. Rev.* **117**, 1460-1466 (1960).
- 3.15. R. C. Miller and A. Savage, "Velocity of Sidewise  $180^\circ$  Domain-Wall Motion in  $\text{BaTiO}_3$  as a Function of the Applied Electric Field," *Phys. Rev.* **112**, 755-762 (1958).
- 3.16. H. L. Stadler, "Ferroelectric Switching Time of  $\text{BaTiO}_3$  Crystals at High Voltages," *J. Appl. Phys.* **29**, 1485-1487 (1958).
- 3.17. H. L. Stadler and P. J. Zachmanidis, "Nucleation and Growth of Ferroelectric Domains in  $\text{BaTiO}_3$  at Fields from 2 to 450 kV/cm," *J. Appl. Phys.* **34**, 3255-3260 (1963).
- 3.18. G. Rosenman, A. Skliar, M. Oron, and M. Katz, "Polarization reversal in  $\text{KTiOPO}_4$  crystals," *J. Phys. D: Appl. Phys.* **30**, 277-282 (1997).

- 3.19. P. Urenski, M. Lesnykh, Y. Rosenwaks, G. Rosenman, and M. Molotskii, "Anisotropic domain structure of  $\text{KTiOPO}_4$  crystals," J. Appl. Phys. **90**, 1950-1954 (2001).
- 3.20. E. Fatuzzo and W. J. Merz, "Switching Mechanism, in Triglycine Sulfate and Other Ferroelectrics," Phys. Rev. **116**, 61-68 (1959).
- 3.21. V. Gopalan and T. E. Mitchell, "Wall velocities, switching times, and the stabilization mechanism of  $180^\circ$  domains in congruent  $\text{LiTaO}_3$  crystals," J. Appl. Phys. **83**, 941-954 (1998).



## Chapter 4. KTP, RKTP and KTA

### 4.1. Introduction

The KTP isomorphs have a unit formula,  $\text{MTiOXO}_4$ , where M usually is K, Rb, Cs or Tl, and X can be P or As. Mixed compositions, such as, e.g.,  $\text{Rb}_x\text{K}_{1-x}\text{TiOPO}_4$ , are also available. These crystals do not occur in nature. The first report of KTP synthesis dates back to 1890 [4.1], however, it was not until the 1970s that KTP and its isomorphs attracted some interest, primarily as nonlinear media for frequency conversion applications [4.2]. These materials are biaxial nonlinear crystals with many excellent properties, such as relatively high nonlinearity, high damage threshold, low optical losses, physical and chemical stability, etc., which make them very attractive for nonlinear optics.

The crystal structure of KTP was determined for the first time in 1974 by Tordjman [4.1, 4.3], whereas its ferroelectric properties were first reported in the 1980s [4.4]. Reports of periodic poling of KTP date back to the 1990s. Various methods were employed to achieve periodic poling in KTP, including electric field poling using chemical patterning [4.5], electron beam writing [4.6], poling at low temperatures [4.7], as well as electric field poling at room temperature [4.8].

This thesis deals mainly with periodic poling of KTP, KTA and bulk Rb-doped KTP (RKTP) crystals. Some important properties of these crystals are outlined in this chapter.

### 4.2. Crystal structure

The KTP isomorphs are orthorhombic and belong to the point group  $2mm$  and the space group  $Pna2_1$ . The crystallographic axes  $a$ ,  $b$  and  $c$  correspond to the optical axes  $x$ ,  $y$  and  $z$ , respectively. The crystal lattice constants for KTP and KTA are given in Table 4.1 [4.9, 4.10]. Every unit cell of a KTP isomorph consists of four asymmetric units, with two formula units per cell.

Table 4.1. Crystal lattice constants of KTP and KTA.

Material	Crystallographic axis, Å		
	A	b	c
KTP	12.819	6.399	10.584
KTA	13.130	6.581	10.781

Note that owing to very low dopant concentration, the lattice constants for bulk Rb-doped KTP can be considered the same as those of KTP.

The crystal structure of KTP consists of  $\text{PO}_4$  tetrahedra and distorted  $\text{TiO}_6$  octahedra, with large cavities in the framework, occupied by the alkali ions, as illustrated in Fig. 4.1.  $\text{PO}_4$  tetrahedra are replaced by  $\text{AsO}_4$  tetrahedra in the KTA crystals. There are eight oxygen atoms bonding both titanium and phosphorus/arsenic atoms. Two oxygen atoms bond only titanium atoms.

## 4.2. Crystal structure

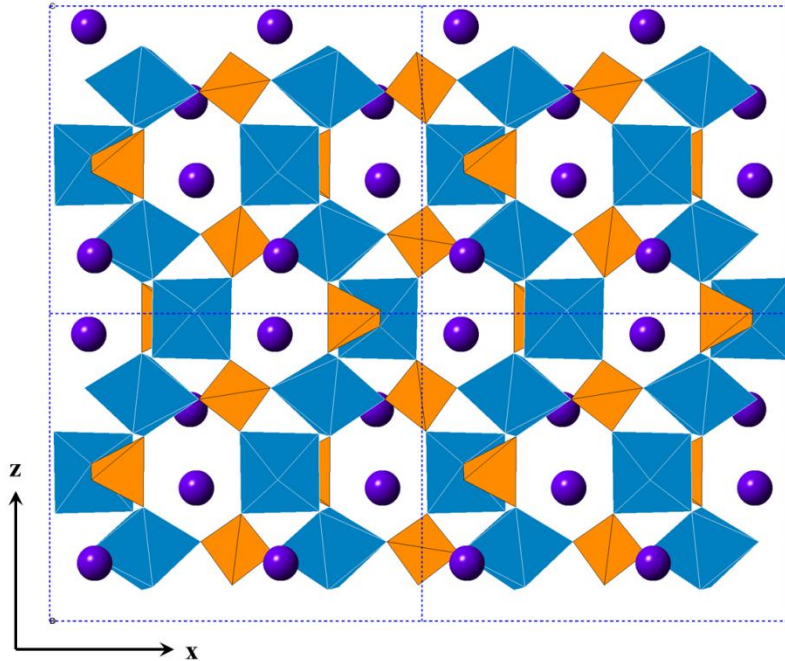


Fig. 4.1. Crystal structure of KTP, viewed in the (010) direction. TiO<sub>6</sub> octahedra are given in blue, PO<sub>4</sub> tetrahedra – in orange, and K<sup>+</sup> ions – in purple color (adapted from [4.9]).

The titanium atoms are displaced in the TiO<sub>6</sub> octahedra, therefore the length of the Ti-O bonds is different. The difference in the Ti-O bond lengths has been suggested as the partial cause of the optical nonlinearity in the KTP crystals. An analysis of KSnOPO<sub>4</sub> (KSP) crystals performed by Thomas *et al.* [4.11], showed that these crystals are closer to being centrosymmetric, because the SnO<sub>6</sub> octahedra in these crystals are much less distorted than TiO<sub>6</sub> in KTP. The SHG output of KSP crystals is only 2% of that of KTP. It has also been shown that the Ti-O bonds are strongly covalent [4.12]. Indeed, the large polarizability of the short covalent Ti-O bonds could also explain the nonlinearity of KTP. On the other hand, the TiO<sub>6</sub> groups are less distorted in KTA; however, the nonlinearity of KTA is similar to that of KTP. Another study indicates that the TiO<sub>6</sub> and P(1)O<sub>4</sub> groups are mainly responsible for the linear optical properties, and that the nonlinearity comes from the KO<sub>x</sub> (x = 8, 9) and the P(2)O<sub>4</sub> groups [4.13]. These contradicting reports indicate that the degree of contribution of the different bonds to the nonlinearity is not yet completely determined.

The cavities, accommodating the cations in the KTP crystal framework, are slightly stretched in the polar direction, forming open channels along the *c* axis, as shown in Fig. 4.2. These channels are responsible for the high ionic conductivity of KTP and KTA. A cation can occupy one of two alternative sites within each cavity. These sites are designated as K(1) and K(2). In the KTP and the KTA crystals both sites are occupied by K<sup>+</sup> ions, with the K(1) site being eight-coordinated and the K(2) site being nine-coordinated.

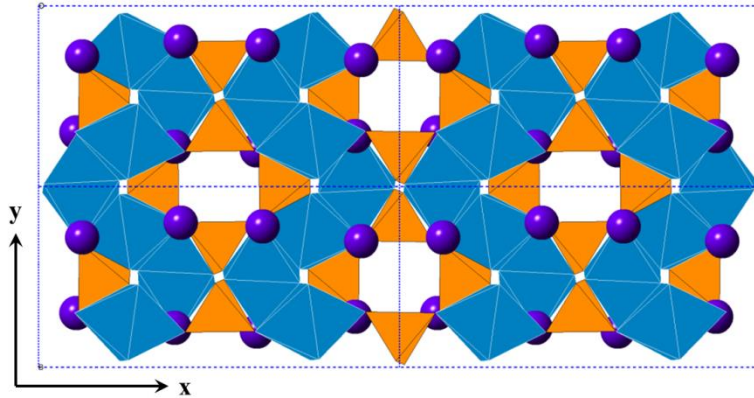


Fig. 4.2. Ionic transport channels in the KTP crystal structure, viewed in the (001) direction (adapted from [4.9]).

The RKTP crystals reported in this thesis are grown from a flux containing 1.4 mol%  $\text{Rb}^+$ , resulting in 0.3%  $\text{Rb}^+$  ions replacing  $\text{K}^+$  ions in the bulk of the grown crystals [4.14]. Rubidium ions preferentially occupy the larger K(2) sites within the crystal structure, when the  $\text{Rb}^+$  concentration is low [4.15].

It has been suggested that domain inversion in the KTP isomorphs occurs by shifting the alkali ions to the alternative sites in the  $-c$  direction, with a slight relaxation of the oxygen sublattice [4.16]. The eight-coordinated alkali ion becomes nine-coordinated and the nine-coordinated alkali ion becomes eight-coordinated. Then the crystal structure is reproduced with the reversed polarity.

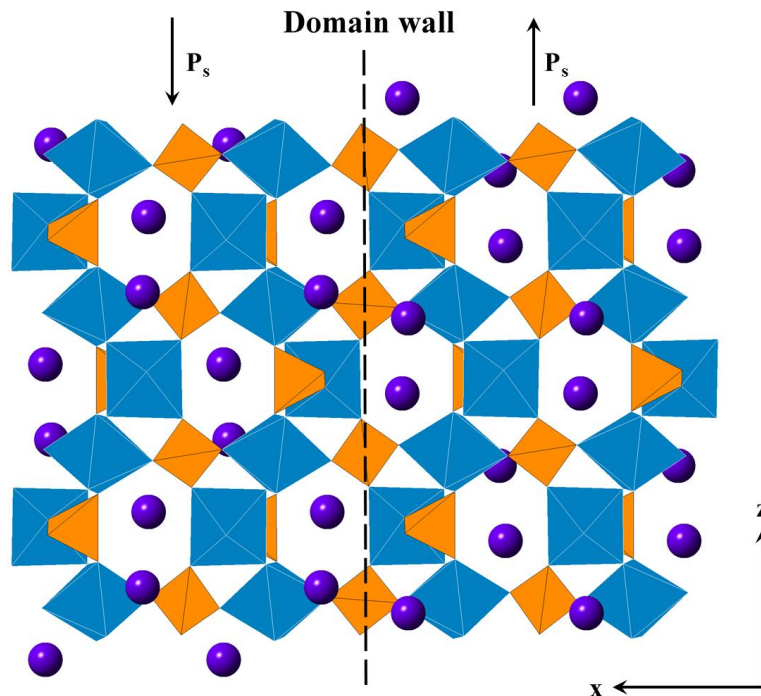


Fig. 4.3. Schematic view of the opposite polarity domains in KTP, linked through the P(1) atoms (adapted from [4.17]).

### 4.3. Crystal growth

An X-ray study of the structural matching at the domain walls performed by Pernot-Rejmankova *et al.*, indicates that the P(1) atom is the pivotal point, linking the inverted domains in the periodically poled KTP crystal, as shown in Fig. 4.3 [4.17].

### 4.3. Crystal growth

The most convenient method to grow large single crystals is to pull the seed from a melt of the material while at the same time controlling the temperature gradients. A necessary condition for this method is that the material melts congruently, i.e., the liquid composition of the material must remain the same as that of the solid. Unfortunately, this is not the case for the KTP isomorphs since they decompose before the melting point is reached. There are two alternative techniques for growing these crystals: the so-called hydrothermal and the flux growth methods.

The most commonly used technique to grow relatively large single crystals of KTP is the flux growth. The term “flux” refers to a solvent containing the crystal components. Fluxes used for growing the KTP isomorphs usually contain various phosphates/arsenates or tungstates. If the flux contains only the crystal components, it is called self-flux. Various dopants can be added to the flux in order to modify the properties of the crystals to be grown. In all of the cases, the crystals are grown in a high temperature flux, usually within 700-1000 °C, depending on the solvents used; however, below the crystal’s melting temperature. For example, KTP crystals can be grown from  $K_6P_4O_{13}$  flux between 928 °C and 840 °C [4.18]. The crystal growth starts from a seed, placed in the coldest spot in the flux in order to avoid secondary nucleations, and continues while the temperature of the container with the flux is slowly decreased. Good temperature stability (better than  $\pm 0.05$  K) and low temperature gradients ensure low thermal strain. It is also important to ensure sufficient flux convection, therefore, the crystal is usually rotated. Flow inhomogeneity is avoided by periodically changing the rotation direction.

The usual morphology of an as-grown KTP crystal is shown in Fig. 4.4 [4.1]. The crystal tends to grow on the (100), (201), (011) and (110) planes. The (201) and (011) faces form sharp caps along the polar direction. The growth rates of the different facets vary depending on the growth parameters, such as the flux components used, and the flux saturation, the temperature, etc. Depending on the growth process, other morphologies are also available; for instance, the growth process can be modified to have a morphology exhibiting (001) faces, which is favorable for growing periodically patterned crystals from a periodically poled seed [4.19]. The disadvantages of the flux growth method include slow crystal growth, different growth rates of the facets and flux impurities. On the other hand, this method is simpler and less expensive compared to the hydrothermal growth.

Alternatively, KTP isomorphs can be grown using the hydrothermal technique. The term “hydrothermal” originates from the field of geological research. The first crystals grown using this technique date from the 19<sup>th</sup> century. In this method, the material is first dissolved in a mineralizer and then recrystallized using high pressure and high temperature.

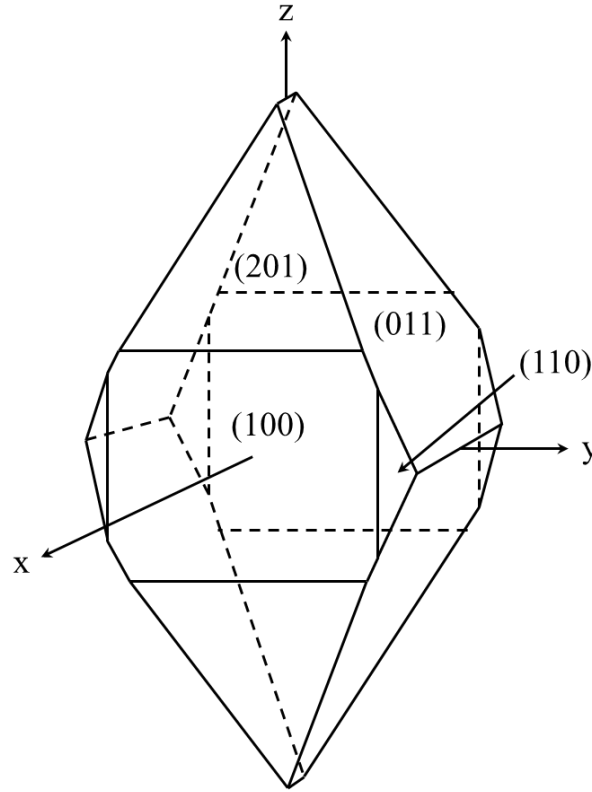


Fig. 4.4. Morphology of the KTP crystals [4.1].

The growth is performed in an autoclave, which must be able to withstand corrosive solvents under the high pressures and temperatures. A temperature gradient is created across the autoclave, so that the nutrient is dissolved in the hot part and then the crystallization occurs in the cooler part. The convection currents generated by the temperature gradient ensure the transport of the material from the hot part to the cooler part. Hydrothermal growth of KTP can be done using a 2M  $\text{K}_2\text{HPO}_4$  mineralizer at a temperature of 400 °C and at a pressure of 1 kbar [4.20]. KTA crystals can also be grown using the hydrothermal method from a 4M  $\text{KH}_2\text{AsO}_4$  mineralizer at a temperature of 590 °C and at a pressure of 1.7 kbar [4.21]. The main advantage of this method is that high quality crystals with a low concentration of vacancies can be grown; however, the special growth conditions and the need for complex equipment make this method a very expensive alternative.

#### 4.4. Ionic conductivity

KTP and its isomorphs are ionic conductors. As already mentioned in Section 4.2, the crystal framework forms open channels along the polar direction, allowing the alkali ions to move via a vacancy hopping mechanism when an electric field is applied across the crystal. Since the channels are formed along the polar direction, the ionic conductivity is highly anisotropic. The magnitude of the conductivity can vary depending on the isomorph composition and the growth process. Potassium vacancies  $V(\text{K}^+)$  are the main defects responsible for the high ionic conductivity of the KTP isomorphs. These defects are dominant in the flux-grown crystals and

#### 4.4. Ionic conductivity

their concentration has a strong dependence on the range of temperatures used for the crystal growth [4.22]. The typical value of the ionic conductivity of KTP and KTA is of the order of  $10^{-4}$  S/m. KTP, grown using the hydrothermal method, usually is of higher stoichiometry, therefore less conductive; however, such crystals are more complicated and expensive to grow.

The ionic conductivity of RKTP crystals is much lower than that of the conventional flux-grown KTP and is typically of the order  $10^{-7}$  S/m. This is a consequence of the  $\text{Rb}^+$  ion being approximately 1.1 times larger than the  $\text{K}^+$  ion, hence, the activation energy of the  $\text{Rb}^+$  ion (0.45 eV) is higher than that of  $\text{K}^+$  ion (0.33 eV). Rubidium ions can form bottlenecks in the ionic conduction channels within the crystal lattice and thereby substantially reduce the ionic conductivity even when their concentration is very low. Polarization switching in this material was first demonstrated by Jiang *et al.*, [4.23], while Wang *et al.*, demonstrated periodic poling of RKTP for the first time [4.24].

The KTA crystals used in our studies were obtained from two different suppliers and can be divided into two groups by their conductivity: a low conductive KTA (LC-KTA) and a high conductive KTA (HC-KTA), confirming the dependence of the ionic conductivity on the growth process. The ionic conductivity of HC-KTA is of the order of  $10^{-4}$  S/m and follows that of the flux-grown KTP, while the conductivity of the LC-KTA is of the order of  $10^{-7}$  S/m and is closer to that of the RKTP crystals.

Fig. 4.5 shows the ionic conductivity dependence on the applied electric field for the different crystals studied in this work. It is worth noting that the dependence of the ionic conductivity on the electric field is nonlinear, which needs to be taken into account when poling these materials with large electric fields.

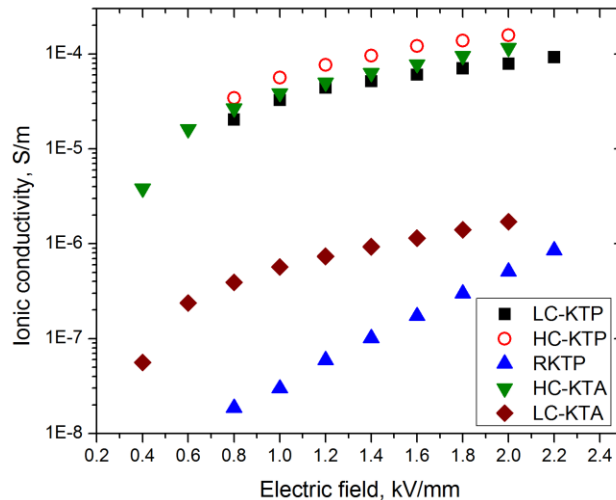


Fig. 4.5. Ionic conductivity dependence on the electric field in low-conductive KTP (black squares), high-conductive KTP (open circles), RKTP (blue triangles), high-conductive KTA (green triangles), and low-conductive KTA (wine rhombs).

## 4.5. Optical properties

The nonlinear coefficient matrix in KTP is:

$$d = \begin{bmatrix} 0 & 0 & 0 & 0 & d_{15} & 0 \\ 0 & 0 & 0 & d_{24} & 0 & 0 \\ d_{31} & d_{32} & d_{33} & 0 & 0 & 0 \end{bmatrix}. \quad (4.5.1)$$

The nonlinear coefficients for KTP and KTA are given in Table 4.2. For QPM applications, usually the largest  $d_{33}$  coefficient is used.

**Table 4.2. Nonlinear coefficients in KTP and KTA.**

	$d_{15}$	$d_{24}$	$d_{31}$	$d_{32}$	$d_{33}$
<b>KTP @ 1064 nm, pm/V [4.25]</b>	1.91	3.64	2.54	4.35	16.9
<b>KTA @ 1064 nm, pm/V [4.26]</b>	2.3	3.2	2.8	4.2	16.2

The optically induced damage threshold is an important parameter of any nonlinear crystal, since it indicates the amount of optical power which can be safely transmitted through the nonlinear medium. The necessity to keep the laser beam intensity below this threshold may also limit the efficiency of the nonlinear frequency conversion process. There are several different mechanisms which can cause optical damage in nonlinear crystals:

1. Linear absorption, dominant with CW, long ( $>1 \mu\text{s}$ ) pulses and high repetition rate pulse trains.
2. Avalanche ionization, pronounced for shorter pulses ( $<1 \mu\text{s}$ ).
3. Multiphoton ionization, dominant with ultra-short (femtosecond) pulses.

Defects, imperfections, and impurities may act as absorption centers or as a source of initial free electrons, and, thereby, play an important role in the ability of the nonlinear material to handle high optical power. Since the concentration of impurities and defects may vary in the crystal, depending on the sample preparation process, the damage threshold is usually presented as a statistical quantity. The damage threshold at the crystal surfaces is usually lower than that in the crystal bulk. The single-shot optical damage threshold is higher compared to the one when the crystal is irradiated with multiple pulses due to accumulation effects. Optical damage may be caused by a single dominant mechanism, or by a combination of different mechanisms. Optically induced damage threshold is a function of the wavelength, pulse duration, pulse repetition rate, focal spot dimensions and the polarization; therefore, these parameters must always be indicated together with the measured damage threshold value.

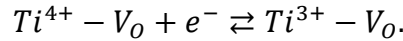
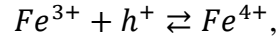
Most optical damage investigations in KTP were done employing nanosecond pulses. Some damage threshold values for KTP are given in Table 4.3. For arbitrary polarized nanosecond pulses, the damage threshold of KTP is  $\sim 2\text{-}3 \text{ GW/cm}^2$ . For comparison, the damage threshold of another extensively used QPM material – near-stoichiometric  $\text{LiTaO}_3$ , in the nanosecond regime, is  $\sim 600 \text{ MW/cm}^2$  [4.27].

#### 4.5. Optical properties

Table 4.3. Damage thresholds of KTP.

Damage threshold, GW/cm <sup>2</sup>	Orientation	Type of damage	Wavelength, nm	Pulse duration, ns	Repetition rate, Hz
2-3[4.28]	type II SHG	Surface	1064	11	10
10-30 [4.29]	type II SHG	?	526	0.03	10
31.5 [4.30]	type II SHG	Bulk	1064	8.5	single shot
2.8-6.2 [4.31]	type II SHG	Bulk	1064	17	1
9.5 [4.32]	type II SHG	?	1064	10	?
2.3-3.3 [4.33]	x or y polarized	Bulk	1064	6	10
8.3 [4.33]	z polarized	Bulk	1064	6	10
3-3.5 [4.34]	type II SHG	Bulk	1064	11	2
2.5-3 [4.34]	type II SHG	Bulk	532	7.8	2

Although KTP has a relatively high damage threshold at 1064 nm, its performance in the visible range is less satisfying. Here, KTP suffers from gray-tracking and considerable linear absorption [4.35, 4.36]. Gray-tracking involves color-center formation under green or blue light, resulting in increased infrared absorption. The formation of gray-tracks is a consequence of crystal imperfections and impurities. A gray-tracking mechanism, proposed by Scripsick *et al.* [4.37], assumes that nearly every KTP crystal contains oxygen vacancies and Fe<sup>3+</sup> impurities of varying concentrations, depending on the specific growth process. The impurities and vacancies act as hole and electron traps, forming color centers of higher optical absorption via the following mechanism:



Potassium vacancies are also partially responsible for color-center formation [4.38]. In this process, the unstable Frenkel pairs ( $K_i^+ - V(K^+)$ ) are stabilized by capturing holes and electrons, resulting in the formation of color centers. In principle, gray-tracks do not introduce permanent damage to the crystals, since the process is reversible; however, the optical damage threshold is reduced due to the higher absorption. KTP is less susceptible to gray-tracking when irradiated with  $z$ -polarized light [4.39]. Consequently, the optical damage threshold for  $z$ -polarized light is substantially higher than that for the orthogonal polarizations [4.33]. This is beneficial in the QPM schemes, since they usually involve  $z$ -polarized photon interactions.

The gray-tracking problem is mitigated in RKTP due to its lower ionic conductivity. In order to assess the resistance to gray-tracking, we compared the blue light-induced infrared absorption dynamics in single-domain, flux-grown KTP, RKTP, and commercial gray-track resistant KTP (GTR-KTP) crystals. In this experiment, the 800 nm, 1 ps long pulses were frequency doubled using a type-I BBO crystal, and, together with the remaining fundamental light, were superimposed with a continuous wave He-Ne beam and focused into the sample. The blue and

the infrared light was polarized parallel and perpendicular to the crystal  $z$ -axis, respectively. The dynamics of the color-center concentration in the samples, after starting the exposure to the picosecond pulses, was determined by measuring the changes in the transmission of the He-Ne beam. Figure 4.6 shows the gray-tracking dynamics of the investigated RKTP, KTP and the GTR-KTP crystals.

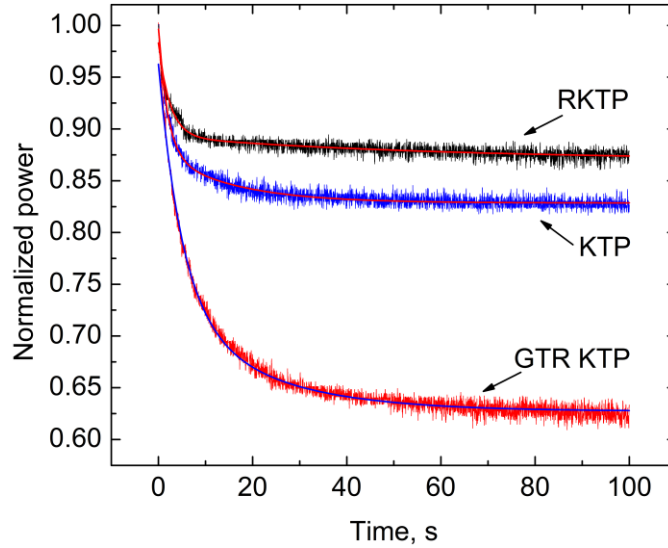


Fig. 4.6. Induced absorption dynamics in RKTP, KTP, and GTR-KTP.

It is clear that RKTP presents the highest resistance to gray-tracking. This can be attributed to the fact that RKTP has a reduced effective mobility of the potassium vacancies. Surprisingly, in the blue spectral region, GTR-KTP appears to be the most susceptible to gray-tracking. Owing to the proprietary process of the crystal growth, there is not enough information to determine the physical reasons of this strong susceptibility to gray-tracking in GTR-KTP.

The transmission spectra for KTP and KTA crystals are shown in Fig. 4.7 [4.40].

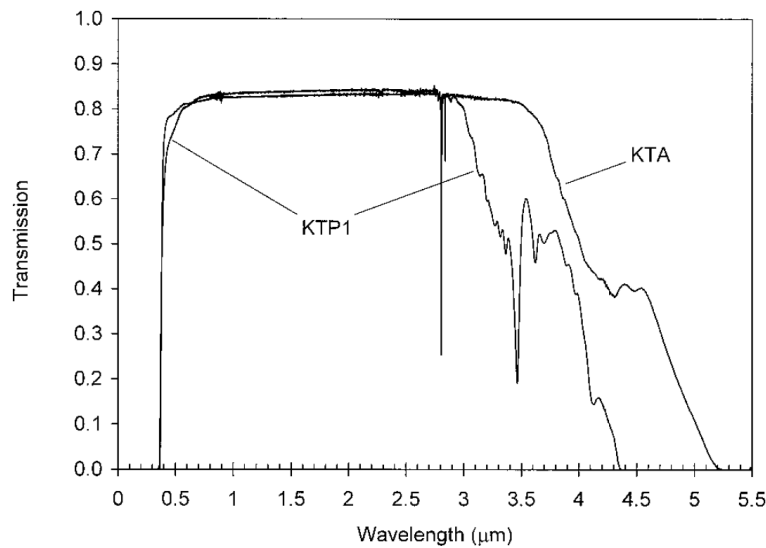


Fig. 4.7. Transmission windows of KTP and KTA in the  $E||z$  direction [40].

#### 4.6. Sellmeier equations

The transmission window of KTP is approximately 0.35-4.3  $\mu\text{m}$ , with a strong absorption feature at  $\sim 2.8 \mu\text{m}$ , caused by  $\text{OH}^-$  impurities, incorporated into the crystals during the growth process. The transparency of KTA extends to  $\sim 5.2 \mu\text{m}$  in the infrared spectral range.

A higher linear absorption in KTP at 532 nm leads to thermal dephasing and, consequently, to lower conversion efficiency, long-term stability and optical damage threshold in SHG applications. The absorption spectra in the visible region for KTP, RKTP and KTA crystals from different vendors are shown in Fig. 4.8.

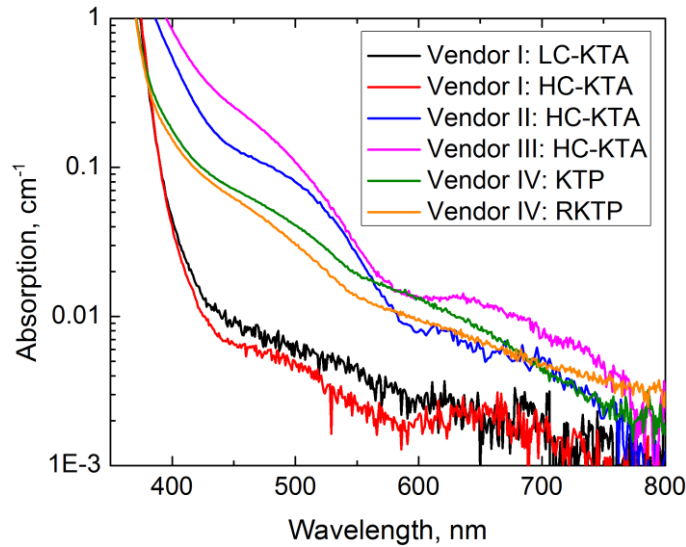


Fig. 4.8. Absorption as a function of wavelength in KTP, RKTP and KTA crystals for  $z$ -polarized light.

Obviously, all evaluated crystals show different absorption properties in the visible spectral range. The most striking difference can be observed among the KTA crystals obtained from vendor I and KTA crystals from vendors II and III. It is also interesting that the difference in absorption among the LC-KTA and HC-KTA crystals, obtained from vendor I, is not significant, even though they substantially differ in their ionic conductivity. This suggests that the increased absorption in the KTA crystals from vendors II and III is likely connected to the impurities which might have been introduced during the growth process to prevent multi-domain crystal formation [4.26]. This also raises the question if the reduced linear absorption in the visible range is an intrinsic property of the KTA crystals, or whether the growth process of KTP and RKTP crystals can be improved in order to reduce the linear absorption in these crystals.

#### 4.6. Sellmeier equations

The QPM grating period in the KTP isomorphs may vary from a few hundred nanometers to a few hundred micrometers depending on the application. For example, periods used for nonlinear interactions, involving counter-propagating photons are in the sub- $\mu\text{m}$  range, a PPKTP crystal designed for SHG of 1064 nm has a period of 9.01  $\mu\text{m}$ , and a 1064 nm pumped degenerate OPO requires a period of 38.86  $\mu\text{m}$ . The optimal period for a specific application depends on the dispersive properties of the material, therefore, accurate knowledge of indices of refraction for

the interacting waves is needed. In addition, the temperature dependence of the refractive indices is very important. The indices of refraction can be calculated using the Sellmeier equations. In KTP and RKTP, the best results for wavelengths shorter than 1  $\mu\text{m}$  can be obtained using the Sellmeier equations derived by Fan *et al.* [4.41], together with the temperature correction from Wiechmann *et al.* [4.42]. The Sellmeier equation in this case is given by:

$$n_z^2 = A + \frac{B}{1-C\lambda^{-2}} + \frac{D}{1-E\lambda^{-2}} - F\lambda^2. \quad (4.6.1)$$

The temperature correction can be written as:

$$\frac{dn_z}{dT} = \frac{a}{\lambda^3} + \frac{b}{\lambda^2} + \frac{c}{\lambda} + d. \quad (4.6.2)$$

The coefficients  $A$ ,  $B$ ,  $C$ ,  $D$ ,  $E$ ,  $F$ , and  $a$ ,  $b$ ,  $c$ ,  $d$  are material specific, and  $\lambda$  is the vacuum wavelength with units in microns. For wavelengths above 1  $\mu\text{m}$ , the Sellmeier data derived by Fradkin *et al.* [4.43], together with the temperature correction by Emanuelli and Arie [4.44], are better optimized. In this case, Eq. (4.6.1) is suitable for calculating the index of refraction but the temperature correction takes the form:

$$\Delta n = n_1(T - 25^\circ\text{C}) + n_2(T - 25^\circ\text{C})^2, \quad (4.6.3)$$

where

$$n_{1,2} = \sum_{m=0}^3 \frac{a_m}{\lambda^m}. \quad (4.6.4)$$

Here the coefficients  $a_m$  are material specific.

Unfortunately, the available Sellmeier data for KTA do not give as good prediction as for KTP. The Sellmeier equation for KTA, derived by Kato and Umemura [4.45], gives the best results for the wavelengths shorter than 1  $\mu\text{m}$  and is given by:

$$n_z^2 = A + \frac{B}{\lambda^2 - C} + \frac{D}{\lambda^2 - E}, \quad (4.6.5)$$

while Eq. (4.6.2) can be used to calculate the refractive index temperature dependence. For wavelengths longer than 1  $\mu\text{m}$ , the Sellmeier data by Fradkin-Kashi *et al.* [4.46], together with the temperature correction by Emanuelli and Arie [4.44] gives better results. The index of refraction, in this case, can be calculated using Eq. (4.6.1), while the temperature correction can be calculated using Eqs. (4.6.3) and (4.6.4). The Sellmeier coefficients for KTP and KTA are given in Table 4.4. The coefficients for temperature correction evaluation for wavelengths below 1  $\mu\text{m}$  are given in Table 4.5 and for wavelengths above 1  $\mu\text{m}$  – in Table 4.6.

**Table 4.4. Sellmeier coefficients for KTP and KTA.**

Material	Coefficient					
	A	B	C	D	E	F
KTP, $\lambda < 1 \mu\text{m}$ [4.41]	2.25411	1.06543	0.05486	0	0	0.02140
KTP, $\lambda > 1 \mu\text{m}$ [4.43]	2.12725	1.18431	0.0514852	0.6603	100.00507	0.00968956
KTA, $\lambda < 1 \mu\text{m}$ [4.45]	6.98362	0.06644	0.05279	920.3789	259.8645	-
KTA, $\lambda > 1 \mu\text{m}$ [4.46]	1.214331	2.225328	0.178542	0.310017	8.989998	0.009381

**Table 4.5. Coefficients for the refractive index temperature correction in KTP and KTA for  $\lambda < 1 \mu\text{m}$ .**

Material	Coefficient, $10^{-5}/^{\circ}\text{C}$			
	a	b	c	D
KTP, $\lambda < 1 \mu\text{m}$ [4.42]	1.2415	-4.4414	5.9129	-1.2101
KTA, $\lambda < 1 \mu\text{m}$ [4.45]	1.5855	-4.2712	4.1149	0.7051

**Table 4.6. Coefficients for the refractive index temperature correction in KTP and KTA for  $\lambda > 1 \mu\text{m}$ .**

Material		Coefficient			
		$a_0$	$a_1$	$a_2$	$a_3$
KTP, $\lambda > 1 \mu\text{m}$ [4.44]	$n_1, 10^{-6}$	9.9587	9.9228	-8.9603	4.1010
	$n_2, 10^{-8}$	-1.1882	10.459	-9.8136	3.1481
KTA, $\lambda > 1 \mu\text{m}$ [4.44]	$n_1, 10^{-6}$	-6.1537	64.505	-56.447	17.169
	$n_2, 10^{-8}$	-0.96751	13.192	-11.78	3.6292

## References

- 4.1. J. Nordborg, "Non-linear Optical Titanyl Arsenates," Doctoral thesis, Department of Inorganic Chemistry, Chalmers University of Technology (Göteborg, Sweden, 2000).
- 4.2. F. C. Zumsteg, J. D. Bierlein, and T. E. Gier, " $K_xRb_{1-x}TiOPO_4$ : A new nonlinear optical material," *J. Appl. Phys.* **47**, 4980-4985 (1976).
- 4.3. P. I. Tordjman, R. Masse, and J. C. Guitel, "Structure Cristalline du Monophosphate  $KTiPO_5$ ," *Zeitschrift für Kristallographie* **139**, 103-115 (1974).
- 4.4. V. K. Yanovskii, and V. I. Voronkova, "Ferroelectric Phase Transitions and Properties of Crystals of the  $KTiOPO_4$  Family," *Phys. Status Solidi* **93**, 665-668 (1986).
- 4.5. W. P. Risk, and S. D. Lau, "Periodic electric field poling of  $KTiOPO_4$  using chemical patterning," *Appl. Phys. Lett.* **69**, 3999-4001 (1996).
- 4.6. M. C. Gupta, W. P. Risk, A. C. G. Nutt, and S. D. Lau, "Domain inversion in  $KTiOPO_4$  using electron beam scanning," *Appl. Phys. Lett.* **63**, 1167-1169 (1993).
- 4.7. G. Rosenman, A. Skliar, D. Eger, M. Oron, and M. Katz, "Low temperature periodic electrical poling of flux-grown  $KTiOPO_4$  and isomorphous crystals," *Appl. Phys. Lett.* **73**, 3650-3652 (1998).
- 4.8. H. Karlsson and F. Laurell, "Electric field poling of flux grown  $KTiOPO_4$ ," *Appl. Phys. Lett.* **71**, 3474-3476 (1997).
- 4.9. D. R. Allan, J. S. Loveday, R. J. Nelmes, and P. A. Thomas, "A high-pressure structural study of potassium titanyl phosphate (KTP) up to 5 GPa," *J. Phys. Condens. Matter* **4**, 2747-2760 (1992).
- 4.10. P. Pernot-Rejmankova, P. A. Thomas, P. Cloetens, F. Lorut, J. Baruchel, Z. W. Hu, P. Urenski, and G. Rosenman, "Periodically poled KTA crystal investigated using coherent X-ray beams," *J. Appl. Cryst.* **33**, 1149-1153 (2000).
- 4.11. P. A. Thomas, A. M. Glazer, and B. E. Watts, "Crystal Structure and Nonlinear Optical Properties of  $KSnOPO_4$  and their Comparison with  $KTiOPO_4$ ," *Acta Cryst.* **B46**, 333-343 (1990).
- 4.12. N. K. Hansen, J. Protas, and G. Marnier, "The electron-density distribution in  $KTiOPO_4$ ," *Acta Cryst.* **B47**, 660-672 (1991).
- 4.13. D. Xue and S. Zhang, "The origin of nonlinearity in  $KTiOPO_4$ ," *Appl. Phys. Lett.* **70**, 943-945 (1997).
- 4.14. F. Masiello, T. A. Lafford, P. Pernot, J. Baruchel, D. S. Keeble, P. A. Thomas, A. Zukauskas, G. Strömquist, F. Laurell, and C. Canalias, "Investigation by coherent X-ray section topography of ferroelectric domain behaviour as a function of temperature in periodically poled  $Rb:KTP$ ," *J. Appl. Cryst.* **44**, 462-466 (2011).
- 4.15. P. A. Thomas, R. Duhlev, and S. J. Teat, "A comparative structural study of a flux-grown crystal of  $K_{0.86}Rb_{0.14}TiOPO_4$  and an ion-exchanged crystal of  $K_{0.84}Rb_{0.16}TiOPO_4$ " *Acta Cryst.* **B50**, 538-543 (1994).
- 4.16. R. A. Stolzenberger and M. P. Scripsick, "Recent advancements in the periodic poling and characterization of RTA and its isomorphs," *Proc. SPIE* **3610**, 23-35 (1999).

## References

- 4.17. P. Pernot-Rejmankova, P. A. Thomas, P. Cloetens, T. Lyford, and J. Baruchel, "Structural matching of ferroelectric domains and associated distortion in potassium titanyl phosphate crystals," *J. Phys.: Condens. Matter* **15**, 1613–1624 (2003).
- 4.18. R. J. Bolt, M. H. van der Mooren, and H. de Haas, "Growth of  $\text{KTiOPO}_4$  (KTP) single crystals by means of phosphate and phosphate/sulfate fluxes out of a three-zone furnace," *J. Cryst. Growth* **114**, 141-152 (1991).
- 4.19. A. Peña, B. Menaert, B. Boulanger, F. Laurell, C. Canalias, V. Pasiskevicius, P. Segonds, C. Felix, J. Debray and S. Pairis, "Template-growth of periodically domain-structured  $\text{KTiOPO}_4$  [Invited]," *Opt. Materials Express* **1**, 185-191 (2011).
- 4.20. R. A. Laudise, R. J. Cava, and A. J. Caporaso, "Phase relations, solubility and growth of potassium titanyl phosphate, KTP," *J. Crystal Growth* **74**, 275-280 (1986).
- 4.21. R. F. Belt and J. B. Ings, "Hydrothermal growth of potassium titanyl arsenate (KTA) in large autoclaves," *J. Crystal Growth* **128**, 956-962 (1993).
- 4.22. P. A. Morris, A. Ferretti, and J. D. Bierlein, "Reduction of the ionic conductivity of flux grown  $\text{KTiOPO}_4$  crystals," *J. Cryst. Growth* **109**, 367-375 (1991).
- 4.23. Q. Jiang, P. A. Thomas, K. B. Hutton, and R. C. C. Ward, "Rb-doped potassium titanyl phosphate for periodic ferroelectric domain inversion," *J. Appl. Phys.* **92**, 2717-2723 (2002).
- 4.24. S. Wang, V. Pasiskevicius, and F. Laurell, "High-efficiency frequency converters with periodically-poled Rb-doped  $\text{KTiOPO}_4$ ," *Opt. Mat.* **30**, 594-599 (2007).
- 4.25. H. Vanherzeele and J. D. Bierlein, "Magnitude of the nonlinear-optical coefficients of  $\text{KTiOPO}_4$ ," *Opt. Lett.* **17**, 982-984 (1992).
- 4.26. L. K. Cheng, L.-T. Cheng, J. D. Bierlein, F. C. Zumsteg, and A. A. Ballman, "Properties of doped and undoped crystals of single domain  $\text{KTiOAsO}_4$ ," *Appl. Phys. Lett.* **62**, 346-348 (1993).
- 4.27. D. S. Hum, R. K. Route, G. D. Miller, V. Kondilenko, A. Alexandrovski, J. Huang, K. Urbanek, R. L. Byer, and M. M. Fejer, "Optical properties and ferroelectric engineering of vapor-transport-equilibrated, near-stoichiometric lithium tantalate for frequency conversion," *J. Appl. Phys.* **101**, 093108 (2007).
- 4.28. F. Ahmed, "Laser damage threshold of  $\text{KTiOPO}_4$ ," *Appl. Opt.* **28**, 119-122 (1989).
- 4.29. J. D. Bierlein and H. Vanherzeele, "Potassium titanyl phosphate: properties and new applications," *J. Opt. Soc. Am. B* **6**, 622-633 (1989).
- 4.30. R. J. Bolt and M. van der Mooren, "Single shot bulk damage threshold and conversion efficiency measurements on flux grown  $\text{KTiOPO}_4$  (KTP)," *Opt. Commun.* **100**, 399-410 (1993).
- 4.31. X. B. Hu, H. Liu, J. Y. Wang, H. J. Zhang, H. D. Jiang, S. S. Jiang, Q. Li, Y. L. Tian, Y. Y. Huang, W. X. Huang, and W. He, "Comparative study of  $\text{KTiOPO}_4$  crystals," *Opt. Mat.* **23**, 369-372 (2003).
- 4.32. C. Zhang, L. Huang, W. Zhou, G. Zhang, H. Hou, Q. Ruan, W. Lei, S. Qin, F. Lu, Y. Zuo, H. Shen, and G. Wang, "Growth of KTP crystals with high damage threshold by hydrothermal method," *J. Cryst. Growth* **292**, 364-367 (2006).

- 4.33. F. R. Wagner, A. Hildenbrand, J. Y. Natoli, M. Commandre, F. Theodore, and H. Albrecht, "Laser damage investigation in  $\text{KTiOPO}_4$  (KTP) and  $\text{RbTiOPO}_4$  (RTP) crystals: threshold anisotropy and the influence of SHG," *Proc. SPIE* **6720**, 672015 (2007).
- 4.34. P. Yankov, D. Schumov, A. Monev, and A. Nenov, "Laser damage tests of large flux-grown  $\text{KTiOPO}_4$  crystals," *Opt. Lett.* **18**, 1771-1773 (1993).
- 4.35. J. Hirohashi, V. Pasiskevicius, S. Wang, and F. Laurell, "Picosecond blue-light-induced infrared absorption in single-domain and periodically poled ferroelectrics," *J. Appl. Phys.* **101**, 033105 (2007).
- 4.36. S. Wang, V. Pasiskevicius, and F. Laurell, "Dynamics of green light-induced infrared absorption in  $\text{KTiOPO}_4$  and periodically poled  $\text{KTiOPO}_4$ ," *J. Appl. Phys.* **96**, 2023-2028 (2004).
- 4.37. M. P. Scripsick, D. N. Loiacono, J. Rottenberg, S. H. Goellner, L. E. Halliburton, and F. K. Hopkins, "Defects responsible for gray tracks in flux-grown  $\text{KTiOPO}_4$ ," *Appl. Phys. Lett.* **66**, 3428-3430 (1995).
- 4.38. V. Mürk, V. Denks, A. Dudelzak, P.-P. Proulx, and V. Vassiltzenko, "Gray tracks in  $\text{KTiOPO}_4$ : Mechanism of creation and bleaching," *Nucl. Instrum. Methods Phys. Res., Sect. B* **141**, 472-476 (1998).
- 4.39. X. B. Hu, J. Y. Wang, H. J. Zhang, H. D. Jiang, H. Liu, X. D. Mu, and Y. J. Ding, "Dependence of photochromic damage on polarization in  $\text{KTiOPO}_4$  crystals," *J. Cryst. Growth* **247**, 137-140 (2003).
- 4.40. G. Hansson, H. Karlsson, S. Wang, and F. Laurell, "Transmission measurements in KTP and isomorphic compounds," *Appl. Opt.* **39**, 5058-5069 (2000).
- 4.41. T. Y. Fan, C. E. Huang, B. Q. Hu, R. C. Eckardt, Y. X. Fan, R. L. Byer, and R. S. Feigelson, "Second harmonic generation and accurate index of refraction measurements in flux-grown  $\text{KTiOPO}_4$ ," *Appl. Opt.* **26**, 2390-2394 (1987).
- 4.42. W. Wiechmann, S. Kubota, T. Fukui, and H. Masuda, "Refractive-index temperature derivatives of potassium titanyl phosphate," *Opt. Lett.* **18**, 1208-1210 (1993).
- 4.43. K. Fradkin, A. Arie, A. Skliar, and G. Rosenman, "Tunable midinfrared source by difference frequency generation in bulk periodically poled  $\text{KTiOPO}_4$ ," *Appl. Phys. Lett.* **74**, 914-916 (1999).
- 4.44. S. Emanuelli and A. Arie, "Temperature-Dependent Dispersion Equations for  $\text{KTiOPO}_4$  and  $\text{KTiOAsO}_4$ ," *Appl. Opt.* **42**, 6661-6665 (2003).
- 4.45. K. Kato, and N. Umemura, "Sellmeier and thermo-optic dispersion formulas for  $\text{KTiOAsO}_4$ ," in *Conference on Lasers and Electro-Optics, CLEO 2004, Technical Digest (CD)*, (Optical Society of America, 2004), paper CThT35. <http://www.opticsinfobase.org/abstract.cfm?URI=CLEO-2004-CThT35>
- 4.46. K. Fradkin-Kashi, A. Arie, P. Urenski, and G. Rosenman, "Mid-infrared difference-frequency generation in periodically poled  $\text{KTiOAsO}_4$  and application to gas sensing," *Opt. Lett.* **25**, 743-745 (2000).



## Chapter 5. Periodic poling of the KTP isomorphs

### 5.1. Introduction

Various methods have been developed in order to implement QPM structures in KTP crystals including electron-beam writing [5.1], electric field poling using chemical patterning [5.2], electric field poling at room temperature [5.3], and at low temperatures [5.4]. Today, the most common method to achieve periodic domain inversion in the KTP isomorphs is room temperature electric field poling.

The goal of the periodic poling is to achieve a uniform QPM grating extending throughout the crystal volume, and with the correct duty-cycle. Unfortunately, this is not always straightforward, because the resulting structure depends on many interrelated parameters, such as the crystal conductivity and its homogeneity, the magnitude, duration and shape of the electric field pulse, the poling temperature, etc. In this chapter periodic poling of KTP, RKTP and KTA crystals is described, the room-temperature electric field poling technique is introduced, and the main difficulties in achieving high-quality QPM gratings are discussed.

### 5.2. Polarization switching characteristics in the KTP isomorphs

The periodic poling process is illustrated in Fig. 5.1.

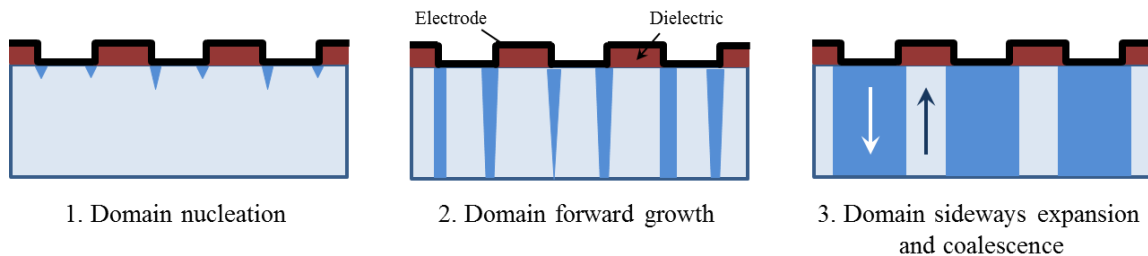


Fig. 5.1. Illustration of the periodic poling process.

When an external electric field is applied to a periodically patterned sample, domain inversion starts with the nucleation at the electrode edges, where the normal component of the electric field is the highest. The nucleated domain tips rapidly propagate along the polar direction, and, at the same time, new tips nucleate under the electrodes. Finally, due to domain sideways expansion the domain tips merge under the electrodes, and ideally, a periodic ferroelectric domain structure with the desired duty-cycle is formed. However, deviation from this is often seen if the poling parameters are not well adjusted, and therefore a good understanding of the polarization switching parameters, such as the ionic conductivity, coercive field, switching time, domain-wall velocities and the domain nucleation properties, is of utmost importance.

High ionic conductivity introduces serious problems in the periodic poling of the KTP isomorphs. In order to switch the spontaneous polarization, it is necessary to simultaneously

## 5.2. Polarization switching characteristics in the KTP isomorphs

supply an electric field exceeding the coercive field of the material, together with a sufficient amount of charge, in order to compensate the ionic current that screens the switching. The shape and the length of the electric field pulse should be designed in a way that will prevent excessive ion-migration in the crystal, which can lead to material breakdown, while at the same time promoting large domain-velocity anisotropy in the in-plane and the polar directions. Therefore, these requirements may impose some limitations, set by the available poling equipment. In addition, high ionic conductivity is one of the dominant factors influencing the domain broadening during the periodic poling process.

Typically, a pronounced variation of the conductivity can be observed across the as-purchased crystal wafers, which can drastically affect the switching characteristics. The conductivity along the polar direction can be determined by applying electric field pulses and measuring the ionic current through a probe with a known surface area. The electric field is applied in the direction parallel to the spontaneous polarization in order to avoid polarization reversal. The spontaneous polarization direction is determined using a  $d_{33}$  piezo tester. By measuring the conductivity in multiple points across the wafer it is possible to obtain a conductivity map and thereby determine the homogeneity of the wafer. A typical conductivity map of a flux-grown KTP is shown in Fig. 5.2(a).

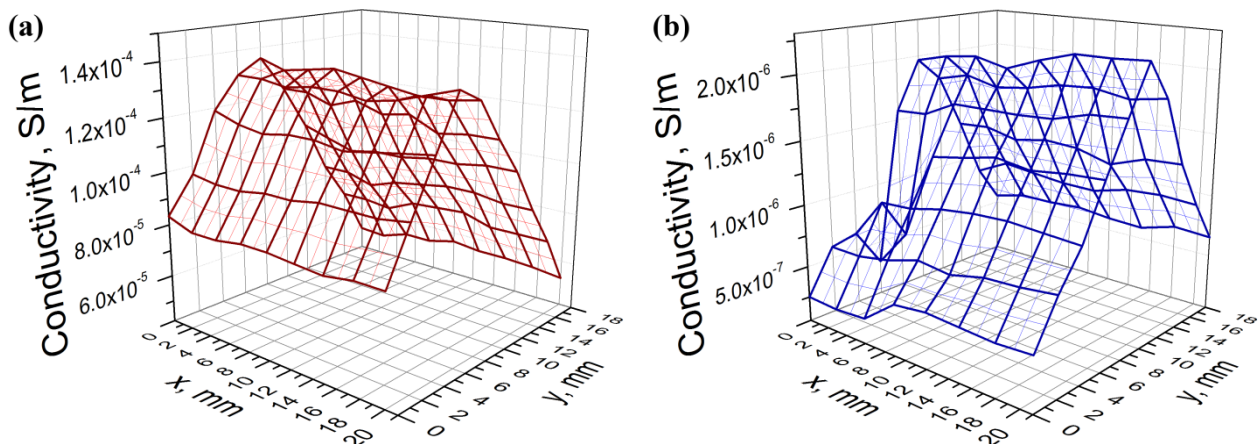


Fig. 5.2. Ionic conductivity map of KTP (a), RKTP (b) wafers.

Usually, the conductivity variation along the  $x$  axis of the wafer is small, while the variation along the  $y$  axis is much more pronounced, sometimes as much as an order of magnitude, and has a parabolic shape. A similar conductivity profile has been obtained for RKTP wafers (Fig. 5.2(b)). Note that the RKTP conductivity is approximately two orders of magnitude lower than that of the flux-grown KTP.

In general, such behavior should also apply to the KTA crystals, however, the KTA crystals used in this project were purchased already cut and polished as single pieces of size of  $10 \times 5 \times 1$  mm<sup>3</sup> along  $x$ ,  $y$  and  $z$  axes, respectively. Unfortunately, it was not possible to obtain conductivity maps or to track the crystal-to-crystal relation in this case.

The coercive field of the material determines the peak voltage of the pulses used for the periodic poling. It can be determined by observing the switching current under a linearly ramped

electric field. In the KTP isomorphs, this measurement is complicated by their high ionic conductivity, which results in the switching current being screened by the ionic current. The total current density, including the switching and the ionic current contributions, can be expressed as follows [5.5]:

$$J = \frac{9}{8} \varepsilon \varepsilon_0 \mu \frac{V^2}{L^3} + 2P_s \frac{1}{A} \frac{\partial A_i}{\partial t}, \quad (5.2.1)$$

where  $\varepsilon$  is the relative permittivity of the material,  $\varepsilon_0$  – the permittivity of free space,  $\mu$  – the ion mobility,  $V$  – the applied voltage,  $L$  – the crystal thickness,  $P_s$  – the spontaneous polarization, and  $A_i$  is the area of the switched domain. When the electric field is ramped up linearly, the ionic current will show a square dependence on the applied voltage, while the switching current will result in a sharp peak at the coercive field. The length and the magnitude of the electric field pulse must be chosen so that the peak of the switching current can be clearly distinguished from the ionic current, and, of course, at the same time, an electric breakdown must be avoided. Figure 5.3 shows some examples of the coercive field measurement in RKTP (a) and KTP (b) crystals.

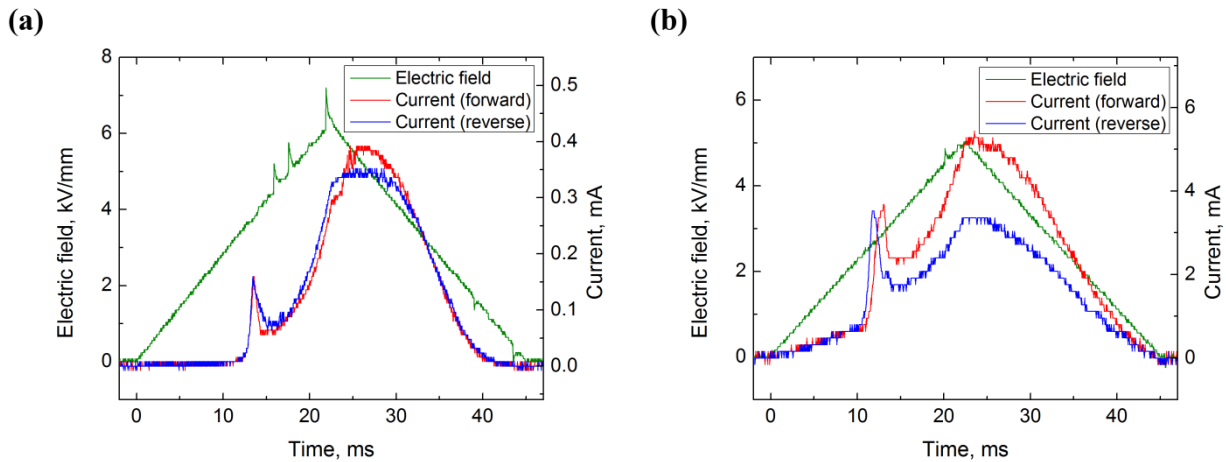


Fig. 5.3. Measured currents under triangular electric field pulses in RKTP (a) and KTP (b) crystals.

The coercive fields were measured by switching the samples from the original to the reversed states (forward direction), and from the reversed state back to the original one (reverse direction). The coercive field in RKTP is 3.7 kV/mm, and it is approximately the same in both the forward and the reverse directions. The coercive field in KTP, as measured in the forward direction, is 2.7 kV/mm, while in the reverse direction it is 2.8 kV/mm. This difference indicates the presence of an internal field of 100 V/mm in KTP, which can be attributed to nonstoichiometric defects [5.6].

It is important to point out that the coercive field strongly depends on the ramp rate of the electric field, which is defined by the peak field magnitude and the pulse length. Keeping a constant peak field magnitude, the coercive field will depend on the pulse length in the following way [5.7]:

$$E_c = \frac{\alpha}{\ln(\tau) - \ln(\gamma)}, \quad (5.2.2)$$

## 5.2. Polarization switching characteristics in the KTP isomorphs

where  $\alpha$  is the activation field,  $\tau$  is the pulse length, and  $\gamma$  is a parameter, independent of the electric field. Figure 5.4 shows the dependence of the coercive field on the pulse length for KTP and RKTP. In this measurement, triangular electric field pulses with a peak magnitude of 6.4 kV/mm were employed.

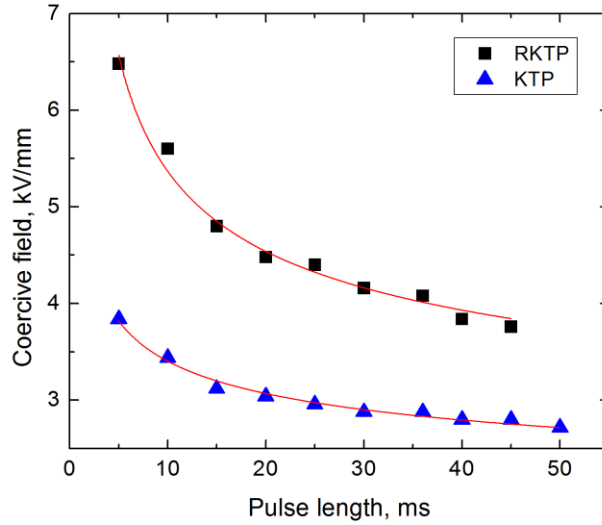


Fig. 5.4. Coercive field dependence on the pulse length. Solid lines represent the numerical fits.

Polarization-switching times and the domain-wall velocities are crucial parameters for understanding the dynamics of domain formation. The switching time indicates how fast the domain structure forms. In addition, the dependence of the switching time on the electric field allows us to distinguish between the different switching regimes, which is important for optimizing the periodic poling conditions. An example of the switching time dependence on the electric field in RKTP is shown in Fig. 5.5.

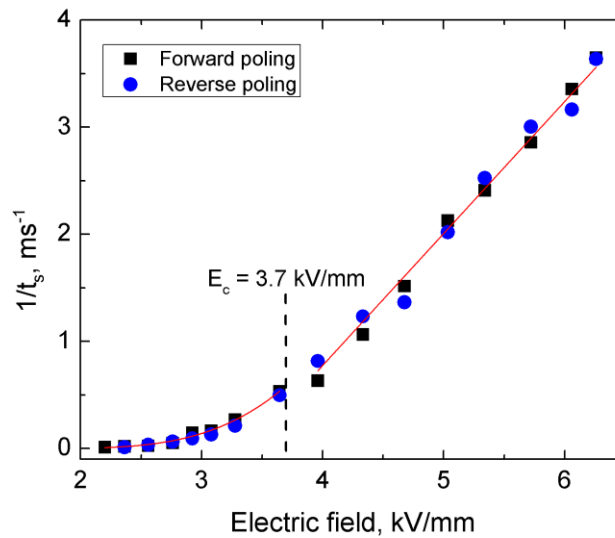


Fig. 5.5. Reciprocal switching time in RKTP as a function of applied electric field.

Two different polarization-switching regimes can be distinguished: the low-field regime (below  $E_c$ ), where the switching is limited by domain nucleation, and the high-field regime (above  $E_c$ ), where the polarization switching is dominated by the domain wall motion. Similar results have been obtained for KTP crystals [5.5].

The domain-wall velocities determine the domain anisotropy and can be estimated by the Miller and Savage method [5.8]: an electric field pulse is applied to the sample and the resulting domain structure is observed; the domain-wall velocity is defined as the average domain width divided by the electric field pulse length. In KTP, the estimated velocity in the  $y$  direction is  $\sim 30$  times larger than that in the  $x$  direction. The domain-wall velocity along the polar axis is at least two orders of magnitude higher than that in the lateral directions [5.5].

The ferroelectric-electrode interface is one of the key factors influencing the domain nucleation rate. Experimentally, it has been determined that an aluminum film, deposited on the  $c^-$  polar face, enhances the domain nucleation in KTP isomorphs. Fig. 5.6 compares the density of the nucleation sites in a virgin RKTP sample ((a) and (b)) to that of RKTP samples metallized on the  $c^-$  face (c), and the  $c^+$  face (d).

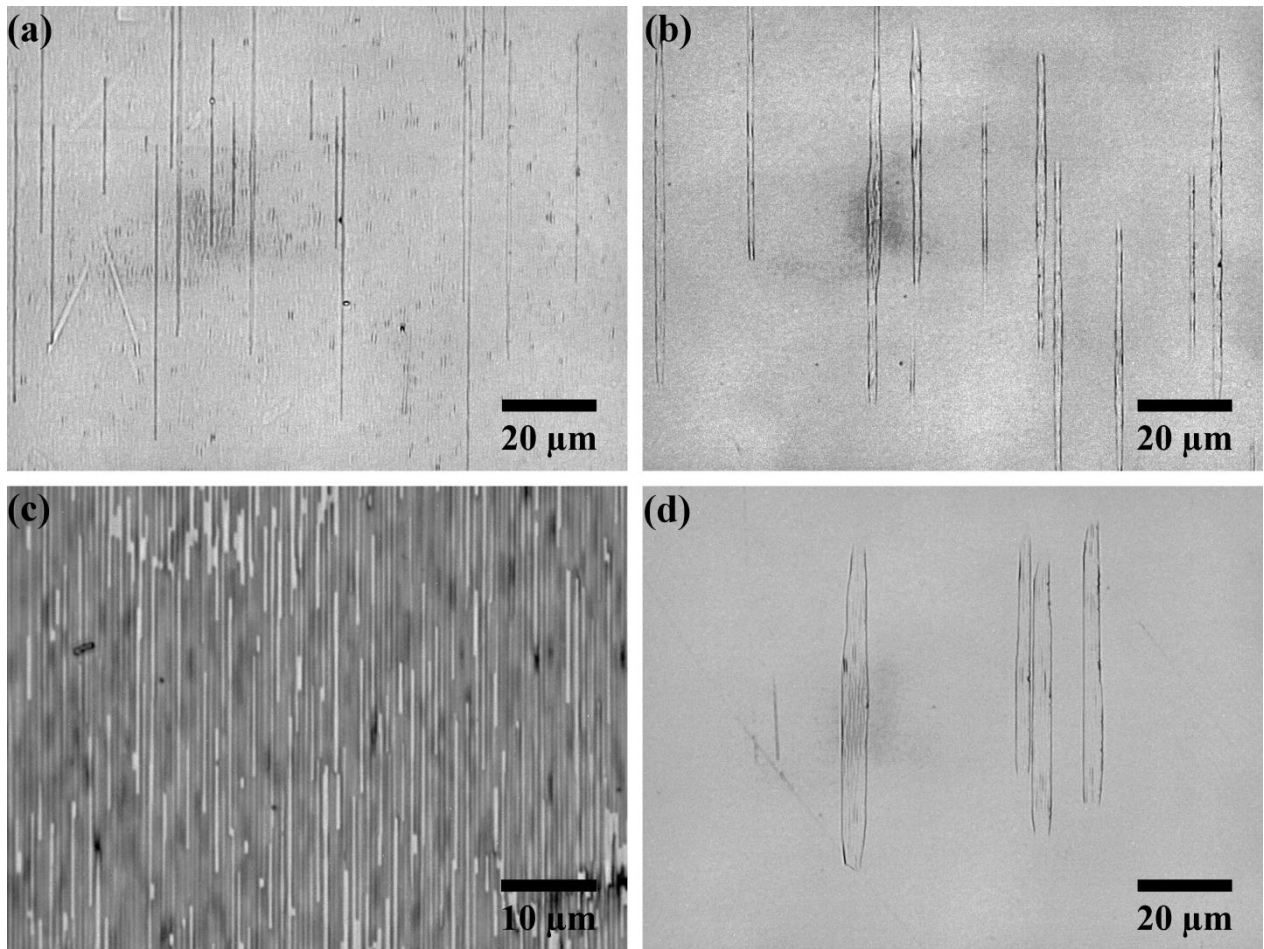


Fig. 5.6. Nucleation sites on the  $c^-$  face (a) and  $c^+$  face (b) of a virgin RKTP crystal, RKTP crystal with an aluminum film on  $c^-$  face (c) and RKTP crystal with an aluminum film on  $c^+$  face (d).

### 5.3. Domain broadening

In all of the cases, a 5 ms long symmetric triangular pulse with a peak magnitude of 5 kV/mm was applied. As can be seen, the nucleation density is the highest in the RKTP sample with an aluminum film deposited on the  $c^-$  face; therefore, this face is a preferential choice for patterning. A similar behavior can be observed in other KTP isomorphs.

### 5.3. Domain broadening

A periodic electrode pattern distorts the distribution of the normal component of the applied electric field,  $E_z$ , and gives rise to a tangential component,  $E_x$ . The distributions of  $E_z$  and  $E_x$  are shown in Fig. 5.7.

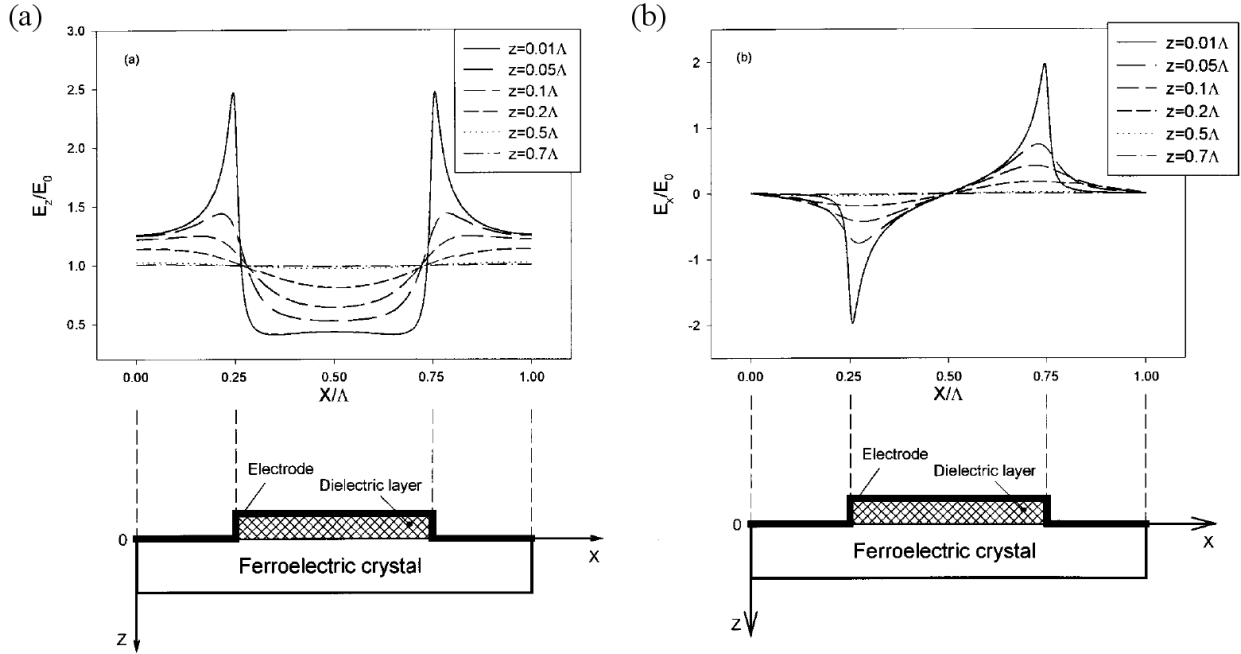


Fig. 5.7. Electric field distribution of the normal component (a) and tangential component (b) in ferroelectric crystal due to the electrode edge [5.9].

During the polarization-switching, the depolarization energy is minimized by the externally supplied compensation charges. The  $E_z$  component is responsible for the inversion of the spontaneous polarization. The domain reversal starts at the edges of the electrodes, since the  $E_z$  component is much higher there than in the bulk. However, compensation charges may also be injected under the isolating photoresist layer by the high tangential electric field component,  $E_x$ , if the conductivity of the crystal is high enough, leading to domain nucleation and growth under the dielectric, causing domain broadening. The width of the domain, growing under the insulating layer, is [5.9]:

$$\Delta a \sim \sigma \tau_{sw}, \quad (5.3.1)$$

where  $\sigma$  is the crystal conductivity, and  $\tau_{sw}$  is the switching time. Domain broadening in the KTP isomorphs can be reduced by the use of the crystals with lower conductivity and/or poling with short electric field pulses.

In addition, domain broadening can be compensated for by controlling the electrode duty-cycle. By choosing an electrode duty-cycle  $D < 0.5$ , it is possible to obtain the optimum domain duty-cycle  $D = 0.5$ . Figure 5.8 shows the former patterned (a) and non-patterned (b) faces of a 3 mm thick PPKTP sample with a period  $\Lambda = 38.86 \mu\text{m}$ . The duty-cycle of the inverted domains on the former patterned face is  $D = 0.49$ , while the electrode duty-cycle was only  $D = 0.3$  (shown in the inset). This duty-cycle is well maintained over the whole crystal thickness and is equal to  $D = 0.48$  on the non-patterned face. Domain broadening is, however, less severe in the PPRKTP due to the lower ionic conductivity of this crystal. Fig. 5.8(c) shows the former patterned face of a 3 mm thick PPRKTP crystal where the duty-cycle of the inverted domains is  $D = 0.3$  – the same as that of the electrode. The duty-cycle is well maintained over the whole sample thickness, and is equal to  $D = 0.32$  on non-patterned face (Fig. 5.8(d)).

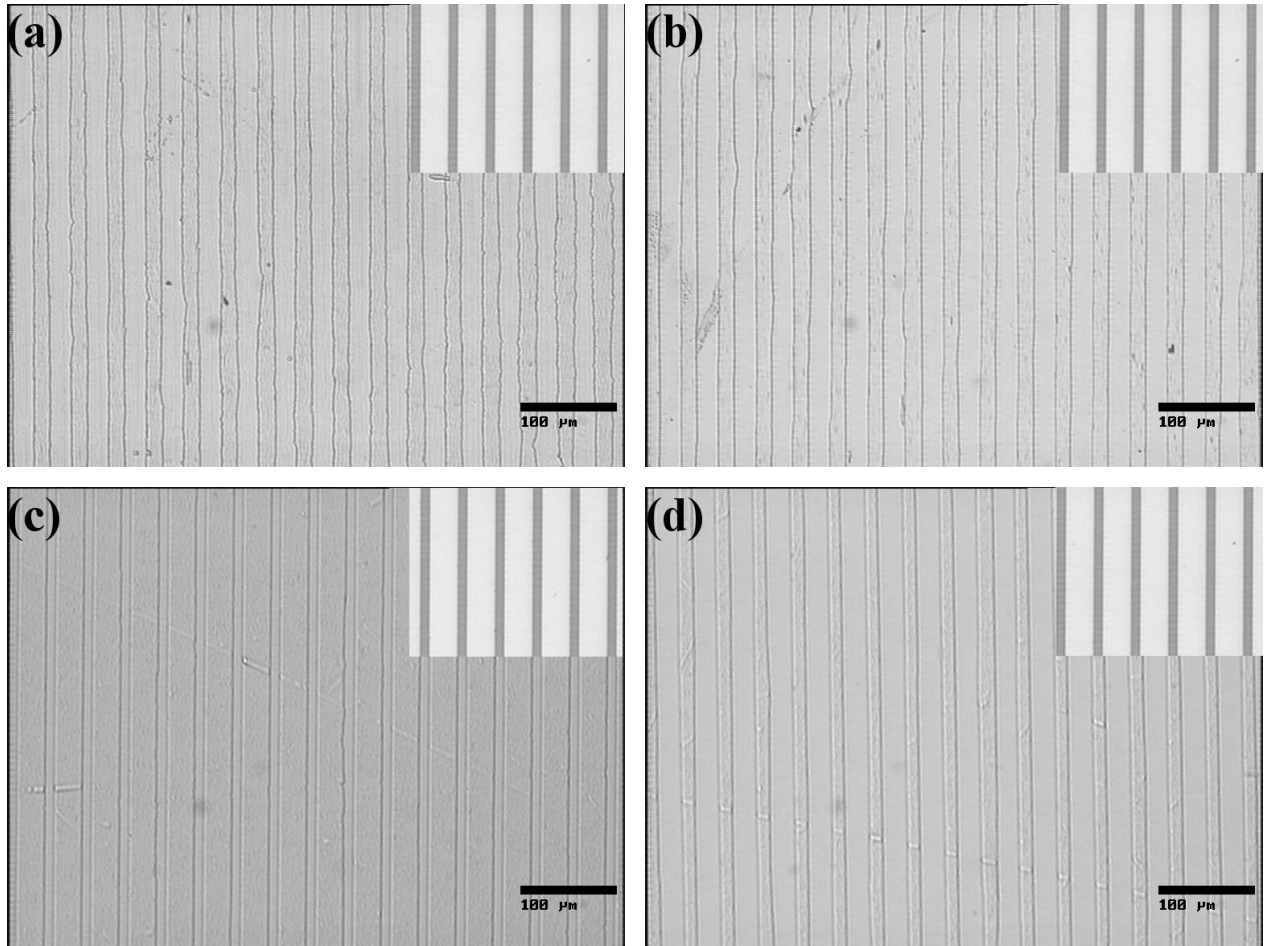


Fig. 5.8. Former patterned (a) and non-patterned (b) faces of a 3 mm thick PPKTP sample, and patterned (c) and non-patterned (d) faces of a 3 mm thick PPRKTP sample with period  $38.86 \mu\text{m}$ . The inset shows the electrode structure.

## 5.4. Sample preparation

### 5.4. Sample preparation

The sample preparation for periodic poling is illustrated in Fig. 5.9. Usually the largest  $d_{33}$  nonlinear coefficient is preferred when fabricating QPM devices in the KTP isomorphs. The as-purchased KTP or RKTP wafers are usually  $z$ -cut and have typical dimensions of  $35 \times 30 \times 1$  mm<sup>3</sup> along the  $x$ ,  $y$  and  $z$  directions, respectively. Due to the variations in the conductivity, it is reasonable to cut the wafer into smaller samples, so that each sample can be poled separately in order to obtain a higher poling yield. Typically, the wafer is cut into smaller samples of size  $10 \times 6 \times 1$  mm<sup>3</sup> along the  $x$ ,  $y$  and  $z$  axes respectively. To take advantage of the ferroelectric domain anisotropy in the KTP isomorphs [5.10, 5.11], the orientation of the periodic electrode pattern is chosen such that the grating vector is aligned along the  $x$  axis and the electrode stripes are aligned along the  $y$  axis of the crystal.

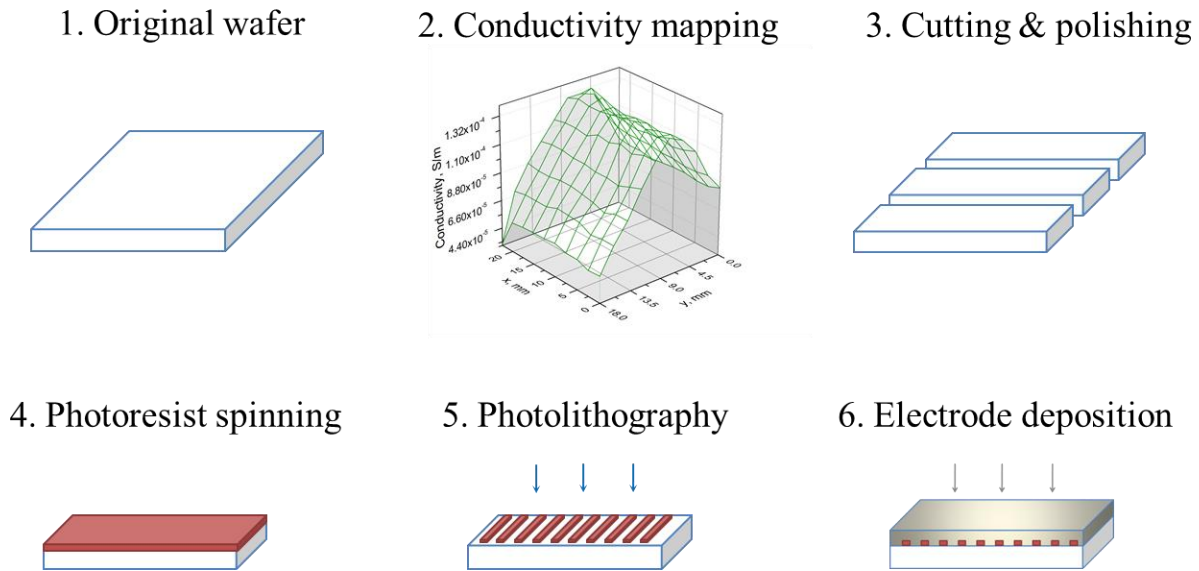


Fig. 5.9. A schematic representation of the sample preparation steps for periodic poling.

The end faces of the samples are polished to an optical quality to let the laser beam pass along the  $x$  axis of the crystals. For grating periods larger than  $2 \mu\text{m}$ , standard contact photolithography patterning is employed. For this purpose, a  $1.8 \mu\text{m}$  thick photoresist layer is deposited on the  $c$  surfaces of the crystals using the spin-coating technique. The photoresist is soft-baked at a temperature of  $110^\circ\text{C}$  for  $90$  s to ensure proper hardening of the photoresist and then the desired pattern is exposed using a contact mask aligner. After the exposure, the photoresist is developed and an aluminum electrode is deposited in the openings. The photoresist structure is kept as an insulator for the regions where domain inversion is undesired.

Due to the limitations of our contact photolithographic system, it is not possible to expose structures smaller than  $1 \mu\text{m}$ , therefore, for applications requiring sub- $\mu\text{m}$  periods, a special in-house interferometric lithography system operating at  $266$  nm wavelength was built. A deep UV

photoresist is used in this case together with a sample preparation procedure similar to the one described above.

### 5.5. Electric field poling setup

After the sample preparation, the crystal is contacted to the poling circuit using liquid electrodes. The schematic poling circuit is shown in Fig. 5.10. The pulse shape is synthesized by an arbitrary waveform generator and is amplified with a high voltage amplifier. A serial resistance  $R_1 = 10 \text{ k}\Omega$ , is used to monitor the current. The resistances  $R_2 = 100 \text{ M}\Omega$  and  $R_3 = 100 \text{ k}\Omega$  act as a voltage divider. The electric field across the sample is determined by measuring the voltage across the resistance  $R_3$ .

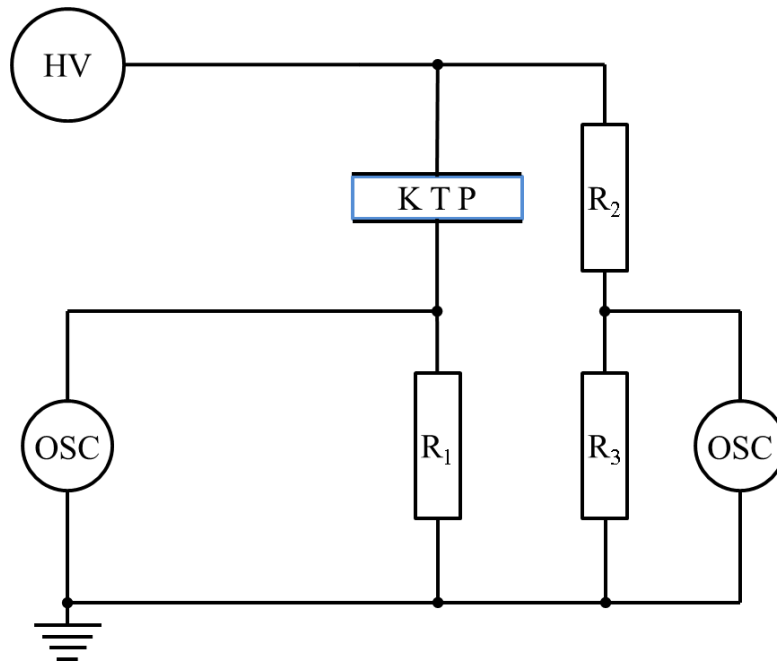


Fig. 5.10. Schematic setup of the poling circuit.

If the magnitude of the applied electric field is too large, domain switching under the isolating photoresist occurs, causing domain broadening and domain merging – so the crystal is considered to be *overpoled*. Conversely, if the magnitude of the applied electric field is too low, the area under the electrodes is not fully reversed and the crystal is *underpoled*. In addition, the outcome of the periodic poling may vary depending on the individual crystal properties, and, therefore, monitoring of the poling process is required. In very low conductive ferroelectric crystals like  $\text{LiNbO}_3$ , the charge transferred through the sample can be used to monitor the poling process. The poling is stopped when the total charge, transferred through the crystal is  $Q = 2P_s A$ , where  $A$  is the area of the electrode. However, due to the relatively high ionic conductivity of the KTP isomorphs it is very difficult to distinguish the switching current from the ionic counterpart, therefore, alternative monitoring methods must be employed. In this thesis, two different monitoring techniques have been used: the first one is based on electro-optic effect [5.12], and

### 5.5. Electric field poling setup

the second is based on in-situ second harmonic generation [5.13]. The setup of the first method is illustrated in Fig. 5.11.

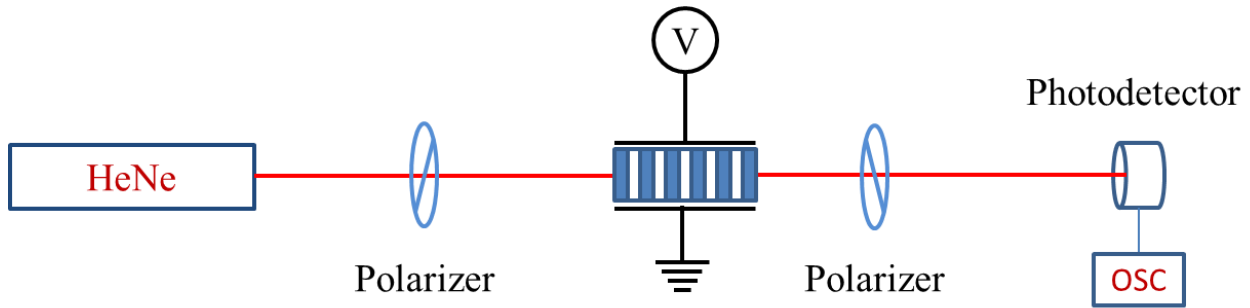


Fig. 5.11. Poling monitoring based on the electro-optic effect.

The light from a He-Ne laser is linearly polarized at  $45^\circ$  relative to the  $z$  axis and launched along the  $x$  axis of the crystal. When an external electric field is applied across the crystal, the output polarization of the laser light will vary due to the electro-optic effect during the rise and fall of the electric field pulse. Additional variation in the polarization occurs when the crystal is being poled and the sign of the electro-optic coefficients reverses. The polarization of the output light is translated into an intensity modulation by a second polarizer, set orthogonally to the input polarization, and is measured by a photodetector. This method allows only a rough estimation of the poling process, but unfortunately it does not help to evaluate the quality of the resulting crystals.

In order to have a direct assessment of the quality of the periodic poling, SHG can be used, as shown in Fig. 5.12.

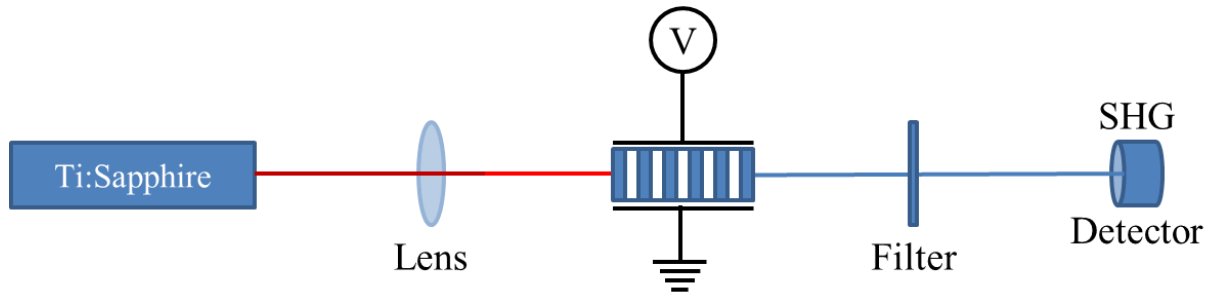


Fig. 5.12. Poling monitoring based on in-situ second harmonic generation.

Here, a tunable continuous wave Ti:Sapphire laser beam is set to the phase-matching wavelength and focused along the  $x$  axis into the crystal. The SHG output after each poling event is recorded by a power meter. Using this method, the quality of the QPM grating can be evaluated by scanning the crystal aperture and measuring the SHG output. Since the available Ti:Sapphire laser can be tuned in the range of 750-950 nm, periods ranging from 3 to 6  $\mu\text{m}$  can be evaluated using the first order SHG, whereas for longer periods, higher order QPM must be used.

A drawback of this method, however, is that the evaluation of the sample is only possible post factum, i.e., when the poling already has occurred. When the external electric field is applied

across the crystal, there is a change in the refractive index due to the electro-optic effect, which shifts the phase-matching wavelength outside the narrow bandwidth of the CW Ti:Sapphire laser, making QPM SHG detection during the periodic poling impossible. Recently, this was addressed by instead using a mode-locked Ti:Sapphire laser, emitting femtosecond pulses with a FWHM bandwidth of 6 nm. This enables an efficient SH generation and online detection during the periodic poling and allows studying the dynamics of the ferroelectric domain structure formation.

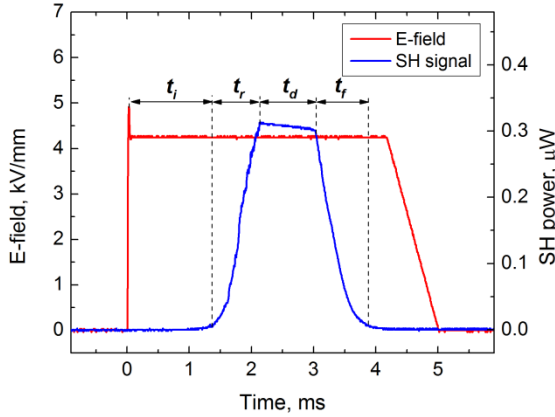
## 5.6. Electric field pulse optimization

The high ionic conductivity presents a serious problem for periodic poling of the KTP isomorphs: first, it leads to domain broadening, described earlier in Section 5.3, and second, it hampers the domain growth in the polar direction. According to Eq. (5.3.1), the domain broadening problem in high conductive ferroelectrics should be mitigated by polarization switching with short electric field pulses, which also increases the domain propagation velocity along the polar axis, since short pulses mean that large electric-field magnitudes must be used. However, the choice of the optimal pulse length is not obvious. Another consideration is the choice of the electric field pulse shape, which can have a significant impact on the QPM grating quality. An online second harmonic generation experiment was performed in order to study the effect of the electric field pulse length and its shape in periodic poling of the RKTP crystals. In this experiment, the crystals were patterned with a period of 4  $\mu\text{m}$  and electrode duty-cycle of 0.47. The domain dynamics was studied by the *in-situ* SHG employing a mode-locked Ti:Sapphire laser as a pump source, operating at 842 nm central wavelength and emitting 170 fs pulses at 76 MHz repetition rate with a FWHM bandwidth of 6 nm, which enabled efficient first order QPM second harmonic generation during the poling process. The  $z$ -polarized laser beam was collimated to a radius of 30  $\mu\text{m}$ , launched along the  $x$  direction, and centered along the  $z$  direction in the crystal. The filtered SH signal was detected with a microsecond temporal resolution detector. This method provides integrated information of the domain formation along the beam path, therefore, the temporal shape of the detected SH signal reflects the dynamics of the QPM structure formation in the sampled volume. Two basic pulse-shapes were chosen: square and symmetric triangular electric-field pulses, as shown in Fig. 5.13. The SH signal temporal evolution during the periodic poling process, shown in Fig. 5.13, demonstrates some characteristic features, namely, the incubation time ( $t_i$ ), the rise time ( $t_r$ ), the dwell time ( $t_d$ ) and the fall time ( $t_f$ ). The incubation time can be associated with the time needed to form the stable ferroelectric domain nuclei under the electrodes [5.14]. The rise time reflects the formation of the QPM grating within the sampled volume. The detection of the SHG signal begins when the reversed domains start propagating through the beam path, and reaches a maximum when the duty-cycle of the domains is close to 0.5. A short rise time indicates a more uniform QPM structure formation, while a long one suggests a larger temporal dispersion between the formation and the growth of the different individual domains, resulting in a less homogeneous QPM structure. The dwell time can be associated with the time needed to form critical nuclei under the insulating photoresist layer. The fall time, associated with the rapid drop of the SH signal, indicates the deviations from the ideal

## 5.6. Electric field pulse optimization

duty-cycle due to the domain broadening, eventually resulting in domain coalescence, corresponding to zero SH signal.

(a)



(b)

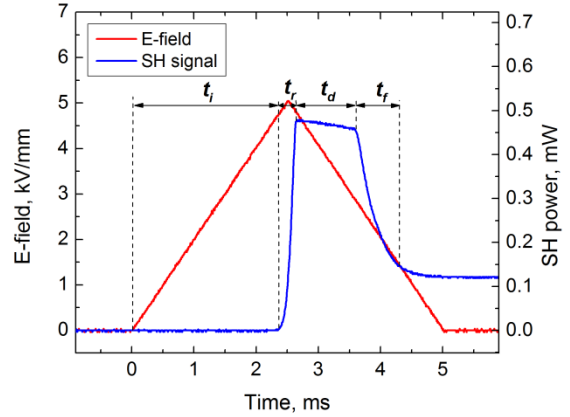


Fig. 5.13. The investigated pulse shapes: square electric field pulse (a), and triangular electric field pulse (b). The blue curves represent the temporal evolution of the second harmonic signal during the poling process.

From Fig. 5.13 it is clear that the QPM grating formation in RKTP occurs on a millisecond timescale, therefore, millisecond pulse length is a reasonable choice for periodic poling. On the other hand, using short pulses increases the coercive field of the material, as evident from Fig. 5.4, and this may therefore be a limiting factor due to the available poling equipment. In addition, an incorrectly chosen pulse length and magnitude may lead to excessive ion migration in the crystal, leading to material breakdown. The experimentally determined optimum electric field pulse length for periodic poling of the KTP isomorphs is typically 2.5-5 ms.

Figure 5.14 shows the evolution of the SH signal in the RKTP crystals poled with a 5 ms long square pulse (a), and a 5 ms long triangular pulse (b), together with the respective ferroelectric domain structures revealed after selective etching on the  $c^+$  faces of both crystals ((c) and (d)). The electric field magnitude in the case of the square pulse was 3.6 kV/mm, while in the triangular pulse case the peak field magnitude was 4.2 kV/mm. In both cases, the field magnitudes were chosen to obtain the maximum SHG output. The rise time in the case of the triangular pulse is 0.34 ms, while in the square pulse case it is almost an order of magnitude longer (2.07 ms). Substantially shorter rise times suggest that poling with pulses of triangular shape is beneficial, since it results in higher quality QPM gratings. This conclusion is supported by the fact that the ferroelectric domain structure on the  $c^+$  face of the PPRKTP crystal, poled with a triangular pulse (Fig. 5.14(d)), is more uniform than that obtained with the square pulse (Fig. 5.14(c)). The superiority of the triangular pulses in periodic poling of RKTP is also confirmed by the substantially higher normalized conversion efficiency obtained in the sample poled with triangular electric field pulse (1.7 %/Wcm), compared to the square pulse case (0.7 %/Wcm).

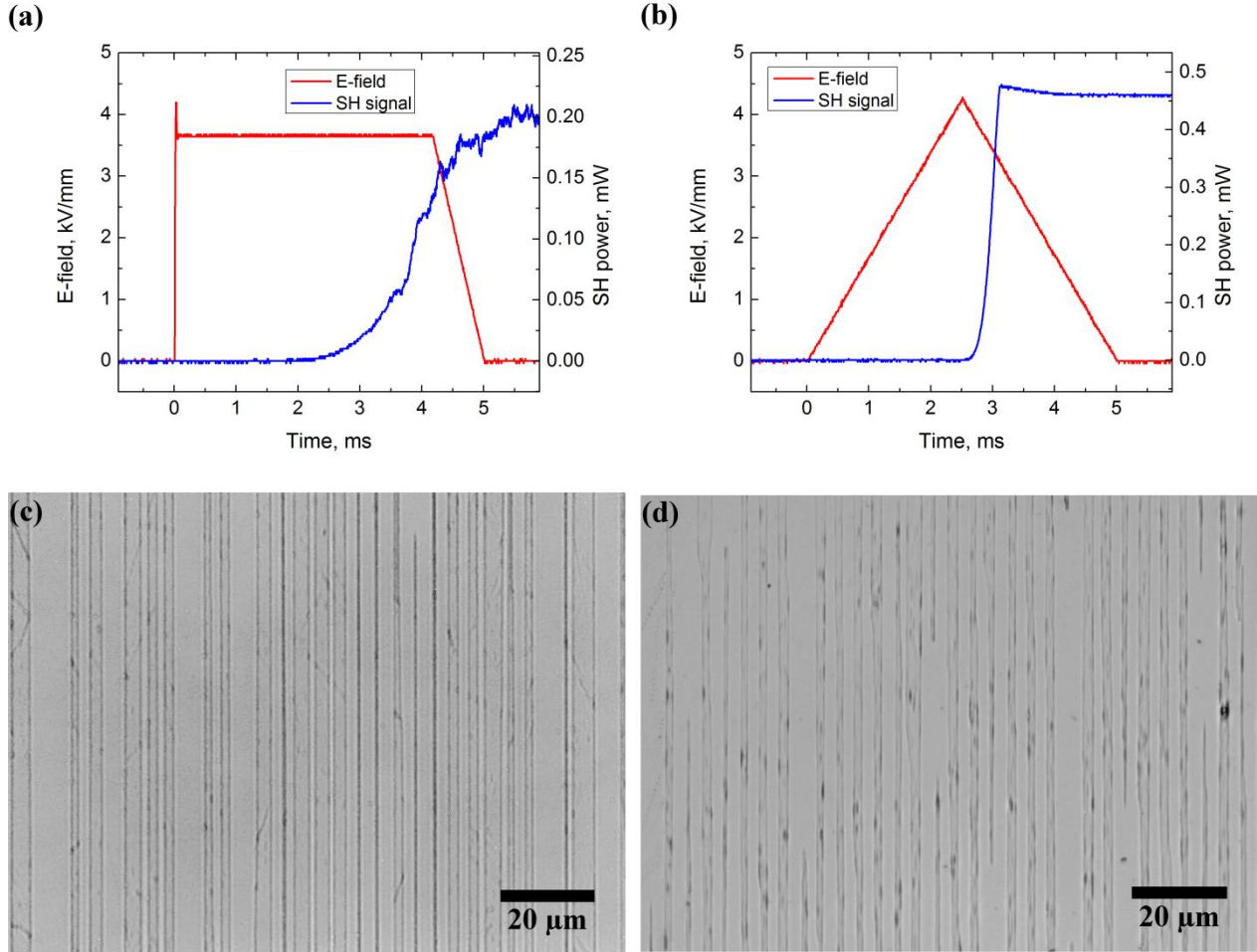


Fig. 5.13. SH signal evolution (blue curve) under square electric field pulse (a), and triangular electric field pulse (b), when the field magnitudes are chosen to obtain the maximum SHG output after the periodic poling. Corresponding ferroelectric domain structures revealed by selective etching in the square pulse case (c) and the triangular pulse case (d).

The differences between periodic poling with square and triangular electric field pulses can be explained by the different nucleation probability distributions in each case. While poling with the square electric field pulse, a constant electric field determines a fixed domain nucleation rate, therefore, the nucleation and propagation of the individual domains happens until the electric field is switched off, resulting in a less uniform QPM grating, which is reflected by a longer SH signal rise time. From Fig. 5.5, it is evident that the polarization switching occurs in a nucleation-limited regime in the square pulse case. On the other hand, since the nucleation probability has an exponential dependence on the electric field [5.15], poling with the triangular pulse results in most domains nucleating near the peak of the electric field pulse, where the probability is the highest, which is also reflected by a short SH signal rise time. A more uniform domain growth under triangular pulses was previously confirmed in a study, using digital holography [5.16].

## 5.7. Sample characterization

### 5.7. Sample characterization

Often it is desirable to visually inspect the QPM grating for any defects or irregularities. This is possible by selectively etching the periodically poled crystals. KOH based water solutions are suitable etchants for the KTP isomorphs [5.17]. The hydroxide attacks the  $c^-$  ends of the domains, while the etch rate of the  $c^+$  ends is much slower. Typically, etching is performed by immersing the crystal for 20 s in a mixture of KOH and  $\text{KNO}_3$  (molar ratio 1.82:1) in water, heated to approximately 100 °C. This method allows revealing the QPM structure on the polar faces of the crystals; however, due to the destructive nature it must be used with caution. It is important to note that the selective etching of the  $y$  faces does not occur in the KTP isomorphs, therefore, this method is not suitable for revealing the domain structure in the crystal bulk.

The homogeneity of the QPM grating can be evaluated by mapping the conversion efficiency across the crystal aperture. For this purpose, the crystal is placed in a temperature-stabilized setup, and the pump beam is launched along the  $x$  axis of the crystal. The pump power is fixed, the crystal is translated in the  $y$ - and the  $z$ - directions in steps, and the conversion efficiency is recorded at each step. The obtained conversion efficiency distribution reflects the QPM grating homogeneity across the crystal aperture.

## References

- 5.1. M. C. Gupta, W. P. Risk, A. C. G. Nutt, and S. D. Lau, "Domain inversion in  $\text{KTiOPO}_4$  using electron beam scanning," *Appl. Phys. Lett.* **63**, 1167-1169 (1993).
- 5.2. W. P. Risk, and S. D. Lau, "Periodic electric field poling of  $\text{KTiOPO}_4$  using chemical patterning," *Appl. Phys. Lett.* **69**, 3999-4001 (1996).
- 5.3. H. Karlsson and F. Laurell, "Electric field poling of flux grown  $\text{KTiOPO}_4$ ," *Appl. Phys. Lett.* **71**, 3474-3476 (1997).
- 5.4. G. Rosenman, A. Skliar, D. Eger, M. Oron, and M. Katz, "Low temperature periodic electrical poling of flux-grown  $\text{KTiOPO}_4$  and isomorphous crystals," *Appl. Phys. Lett.* **73**, 3650-3652 (1998).
- 5.5. C. Canalias, J. Hirohashi, V. Pasiskevicius, and F. Laurell, "Polarization-switching characteristics of flux-grown  $\text{KTiOPO}_4$  and  $\text{RbTiOPO}_4$  at room temperature," *J. Appl. Phys.* **97**, 124105 (2005).
- 5.6. P. A. Morris, A. Ferretti, and J. D. Bierlein, "Reduction of the ionic conductivity of flux grown  $\text{KTiOPO}_4$  crystals," *J. Cryst. Growth* **109**, 367-375 (1991).
- 5.7. H. H. Wieder, "Activation field and coercivity of ferroelectric barium titanate," *J. Appl. Phys.* **28**, 367-369 (1957).
- 5.8. R. C. Miller and A. Savage, "Velocity of Sidewise  $180^\circ$  Domain-Wall Motion in  $\text{BaTiO}_3$  as a Function of the Applied Electric Field," *Phys. Rev.* **112**, 755-762 (1958).
- 5.9. G. Rosenman, Kh. Garb, A. Skliar, M. Oron, D. Eger, and M. Katz, "Domain broadening in quasi-phase-matched nonlinear optical devices," *Appl. Phys. Lett.* **73**, 865-867 (1998).
- 5.10. G. Rosenman, A. Skliar, M. Oron, and M. Katz, "Polarization reversal in  $\text{KTiOPO}_4$  crystals," *J. Phys. D: Appl. Phys.* **30**, 277-282 (1996).
- 5.11. P. Urenski, M. Lesnykh, Y. Rosenwaks, and G. Rosenman, "Anisotropic domain structure of  $\text{KTiOPO}_4$  crystals," *J. Appl. Phys.* **90**, 1950-1954 (2001).
- 5.12. H. Karlsson, F. Laurell, and L. K. Cheng, "Periodic poling of  $\text{RbTiOPO}_4$  for quasi-phase matched blue light generation," *Appl. Phys. Lett.* **74**, 1519 (1999).
- 5.13. S. Wang, V. Pasiskevicius, and F. Laurell, "High-efficiency frequency converters with periodically-poled Rb-doped  $\text{KTiOPO}_4$ ," *Opt. Materials* **30**, 594-599 (2007).
- 5.14. V. Gopalan and T. E. Mitchell, "Wall velocities, switching times, and the stabilization mechanism of  $180^\circ$  domains in congruent  $\text{LiTaO}_3$  crystals," *J. Appl. Phys.* **83**, 941-954 (1998).
- 5.15. R. C. Miller and A. Savage, "Velocity of Sidewise  $180^\circ$  Domain-Wall Motion in  $\text{BaTiO}_3$  as a Function of the Applied Electric Field," *Phys. Rev.* **112**, 755-762 (1958).
- 5.16. C. Canalias, V. Pasiskevicius, F. Laurell, S. Grilli, P. Ferraro, and P. De Natale, "In situ visualization of domain kinetics in flux grown  $\text{KTiOPO}_4$  by digital holography," *J. Appl. Phys.* **102**, 064105 (2007).
- 5.17. F. Laurell, M. G. Roelofs, W. Bindloss, H. Hsiung, A. Suna, and J. D. Bierlein, "Detection of ferroelectric domain reversal in  $\text{KTiOPO}_4$  waveguides," *J. Appl. Phys.* **71**, 4664-4670 (1992).



## Chapter 6. Periodic domain structures in KTA

### 6.1. KTA as a nonlinear medium

The high ionic conductivity of KTA is probably the main impediment to achieve periodic poling in this material. Conductivity variations across the poled area may significantly influence the quality of the QPM grating. Additionally, high ionic conductivity sets a demanding requirement for simultaneously supplying the high voltage and the large amount of external charge needed to compensate the ionic current. Rosenman *et al.*, overcome the conductivity problem by poling KTA at temperatures below 170 K, where the ionic conductivity of KTA is suppressed [6.1]. This method, however, requires complex instrumentation, and a substantially increased coercive field at low temperatures limits the aperture of the QPM devices. On the other hand, the work presented in this thesis demonstrates that it is possible to periodically pole KTA with short electric field pulses at room temperature.

### 6.2. Periodic poling of KTA

The KTA crystals used in this work were commercial, single-domain, *z*-cut, flux-grown samples, obtained from three different vendors. Four different types of KTA crystals were distinguished by their vendors and their conductivity: low-conductive KTA from vendor I (LC-KTA), high-conductive KTA from vendor I (HC1-KTA), high-conductive KTA from vendor II (HC2-KTA), and high-conductive KTA from vendor III (HC3-KTA). This designation is given in Table 6.1.

Table 6.1. KTA crystal designation by vendor and conductivity.

Crystal designation	Crystal vendor	Conductivity, S/m
LC-KTA	Coherent Inc.	$5 \times 10^{-8} - 8.2 \times 10^{-8}$
HC1-KTA	Coherent Inc.	$1.5 \times 10^{-5} - 4 \times 10^{-5}$
HC2-KTA	Eksma Optics	$8.1 \times 10^{-5} - 1.1 \times 10^{-4}$
HC3-KTA	Crystech Inc.	$2 \times 10^{-3} - 3.4 \times 10^{-3}$

Most of the as-purchased KTA crystals were found to be multi-domain, with “natural” domains of sizes varying from a few millimeters to tens of micrometers and extending over the whole crystal thickness, therefore, they were first poled with planar electrodes to obtain single-domain crystals. This “pre-poling” was performed by applying several 5 ms long 6 kV/mm square shape electric field pulses.

For OPO applications, the HC1-KTA crystals were patterned on the *c*<sup>-</sup> faces with a period of 39.5 μm and a duty-cycle of 0.5. For relatively large periods, domain broadening is less severe and such crystals can be periodically poled with short square shape electric field pulses. In this case 5 ms long electric field pulses were used. The magnitude of the electric field was set between 2.3 and 2.6 kV/mm depending on the specific ionic conductivity of each sample. An example of the resulting domain structure on the patterned face (a) and the non-patterned face (b)

## 6.2. Periodic poling of KTA

of a selectively etched PPKTA sample is shown in Fig. 6.1. Note that the duty-cycle of the inverted domains in this sample varies from 0.54 on the patterned face to 0.56 on the non-patterned face, therefore it can be assumed that a slightly lower electric field magnitude would have resulted in an ideal 0.5 duty-cycle all the way through the crystal.

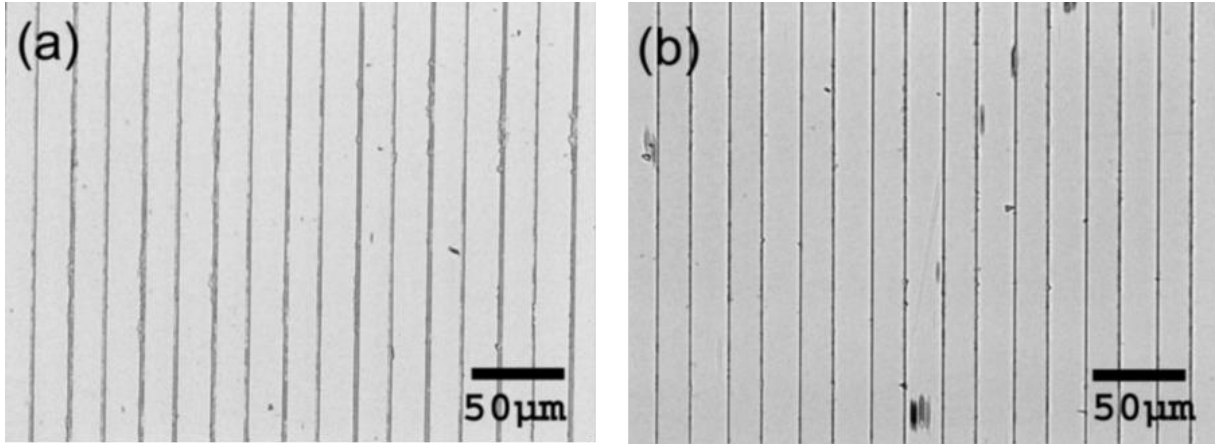


Fig. 6.1. Periodic domain structure revealed by selective etching on the patterned face (a) and the non-patterned face (b) of a PPKTA sample with period 39.5  $\mu\text{m}$ .

For SHG at 1066 nm, the LC-KTA, HC2-KTA and HC3-KTA crystals patterned with a period of 8.49  $\mu\text{m}$  and a duty-cycle of 0.15 were used. Since domain broadening depends on the crystal conductivity, it was expected that the electrode pattern would be best reproduced in the LC-KTA crystals, while some broadening would occur in the HC2-KTA crystals. In the HC3-KTA crystals, the domain broadening would be the most severe. As discussed in Chapter 5, poling with short electric field pulses of a symmetric triangular shape should mitigate the domain-broadening problem. Furthermore, triangular pulses offer a larger tolerance window of the electric field magnitude, which was of utmost importance for these samples, since the crystals that were initially multi-domain presented regions with slightly different coercive fields. The LC-KTA samples were poled at room temperature with 2.5 ms long electric field pulses of magnitude 5.4 kV/mm, while the HC2-KTA samples were poled applying 5 ms long pulses of magnitude 4.6 kV/mm. The total charge transferred through the crystal, including the contributions of the ionic and the switching current, was  $3.3 \times 10^{-5}$  C in the periodically poled HC2-KTA (HC-PPKTA) case, and  $7.6 \times 10^{-6}$  C in the periodically poled LC-KTA (LC-PPKTA) case. Since the spontaneous polarization was assumed to be the same in both materials, the actual current required for domain switching was about an order of magnitude larger in HC2-KTA. The current requirement for switching the HC3-KTA crystals was even larger. Unfortunately, the available equipment failed to meet this requirement, therefore, these high-conductive crystals could not be switched. Figure 6.2 shows the domain structure on the polar faces of the HC-PPKTA (a) and the LC-PPKTA (b) crystals. The duty-cycle of the inverted domains is around 0.45 on the patterned face, and 0.51 on the non-patterned face. As expected, the domain broadening was reduced in the LC-PPKTA crystals, leading to a duty-cycle of the reversed domains of 0.27 on the patterned face, and approximately 0.36 on the opposite face, as shown in Fig. 6.2(b).

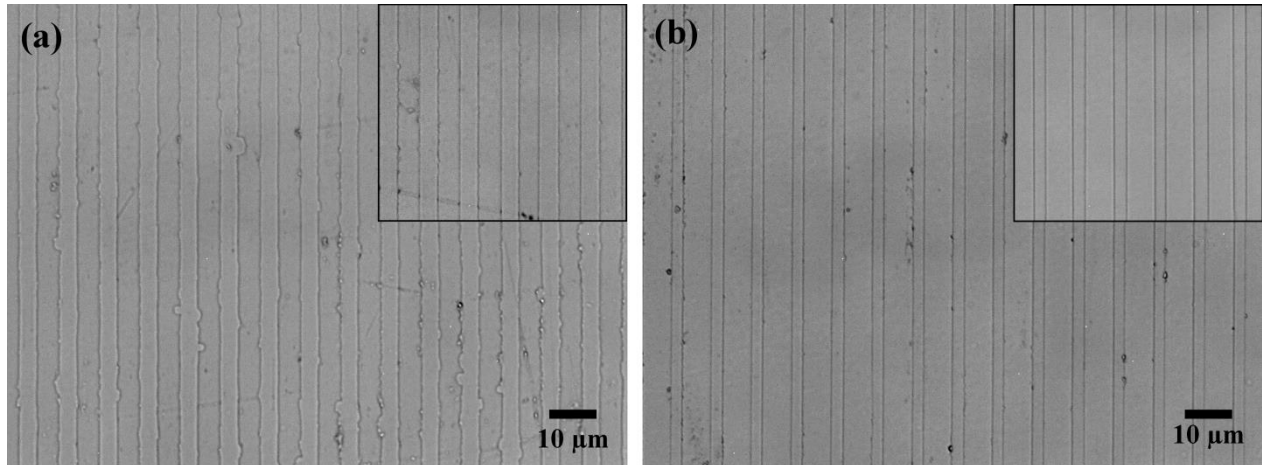


Fig. 6.2. Periodic domain structure on the patterned face of the HC-PPKTA (a) and the LC-PPKTA (b) crystals. The insets show the periodic structure on the non-patterned faces of the HC-PPKTA and the LC-PPKTA crystals, respectively.

### 6.3. PPKTA-based OPO

The PPKTA crystal shown in Fig. 6.1 was used to demonstrate a QPM OPO. For this purpose, the uncoated crystal was placed in a linear OPO cavity, pumped by 1064 nm light, generating a 1.538  $\mu\text{m}$  signal and a 3.452  $\mu\text{m}$  idler output. The effective nonlinear coefficient of the PPKTA crystal was evaluated by measuring the threshold energy for different cavity lengths while using a 90% reflectivity output coupler. Figure 6.3 shows the measured threshold energies for cavity lengths of 30–50 mm together with the calculated thresholds for different values of  $d_{\text{eff}}$ .

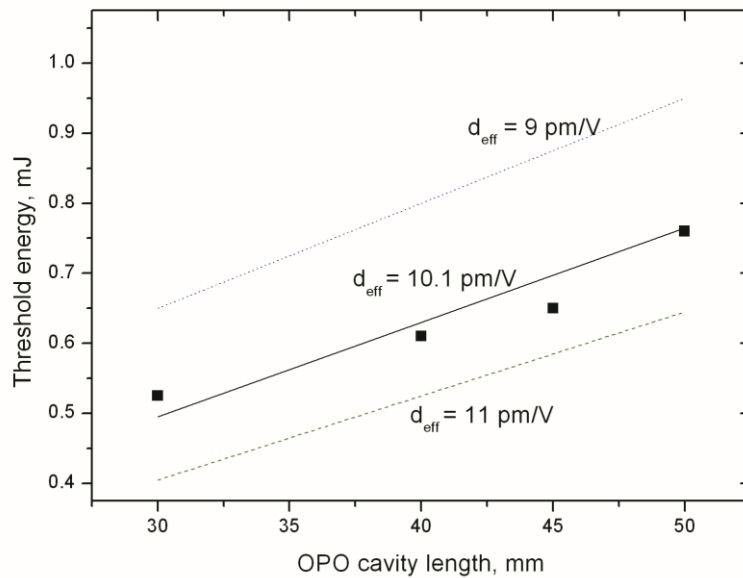


Fig. 6.3. PPKTA OPO threshold energy versus the OPO cavity length. Squares represent the experimental data. The dotted, solid and dashed lines are calculated OPO threshold energies, corresponding to effective nonlinearities of 9 pm/V, 10.1 pm/V and 11 pm/V, respectively.

#### 6.4. PPKTA for second harmonic generation

As can be seen, an effective nonlinear coefficient value  $d_{eff} = 10.1$  pm/V is in good agreement with the experimental results. This value is very close to the expected value of 10.3 pm/V obtained by  $d_{eff} = 2d_{33}/\pi$ , where  $d_{33} = 16.2$  pm/V [6.2] for a perfect QPM grating with a duty-cycle of 0.5.

To obtain a highly efficient OPO, a partially reflective output coupler with  $R = 50\%$  at the signal wavelength, and a cavity length of 30 mm were used. Figure 6.4 shows the pump depletion, the signal efficiency, and the combined signal and idler efficiency for different pump energies.

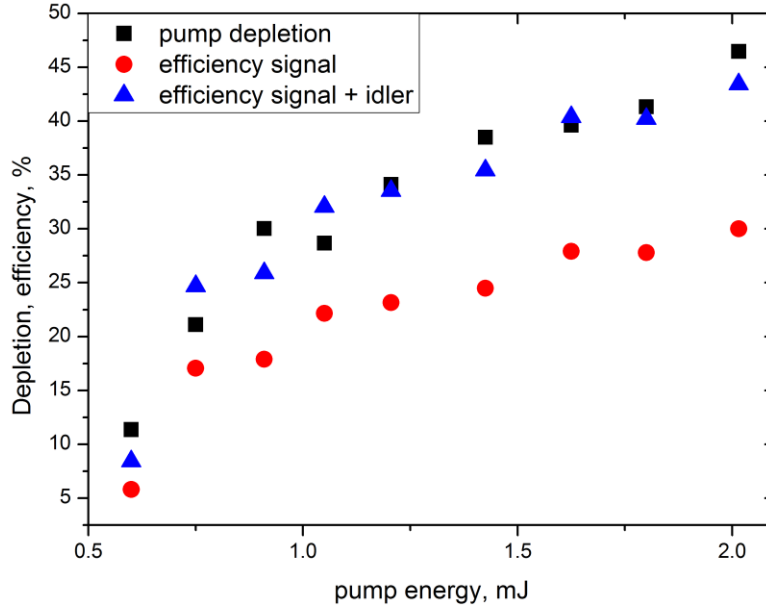


Fig. 6.4. PPKTA OPO pump depletion and the efficiencies as a function of pump energy.

Two dielectric mirrors, transmitting at 1064 nm and reflecting at 1.5  $\mu\text{m}$ , were used to separate the signal and the pump light. The signal wavelength was 1538.2 nm with a FWHM bandwidth of 2.5 nm while the maximum signal output was 0.6 mJ (130 MW/cm<sup>2</sup>) for a pump energy of 2 mJ (440 MW/cm<sup>2</sup>). The depletion and the combined signal and idler efficiency reached 45% for 2 mJ of pump energy and were approximately the same over the whole pump energy range. This supports the expected low absorption of the PPKTA at the signal wavelength.

#### 6.4. PPKTA for second harmonic generation

The uncoated HC-PPKTA and LC-PPKTA crystals were evaluated in a SHG setup pumped by a tunable CW Ti:Sapphire laser. The pump beam was launched along the crystal  $x$ -axis and focused into the crystal to a beam waist of 25  $\mu\text{m}$ , while the crystal temperature was kept at 21  $^{\circ}\text{C}$ . Figure 6.5 shows the conversion efficiencies for these crystals as a function of pump power at a wavelength of 1066 nm.

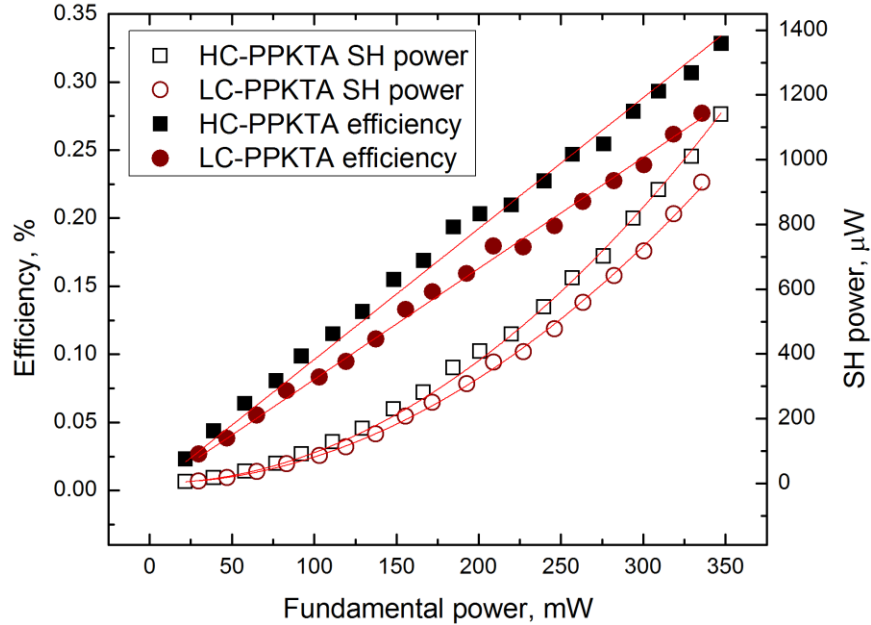


Fig. 6.5. Second harmonic power (open symbols) and conversion efficiency (solid symbols) of HC-PPKTA (squares) and LC-PPKTA (circles) as a function of pump power. The solid curves represent the quadratic fits in the SH power case, and linear fits in the efficiency case.

At a fundamental pump power of 347 mW, the HC-PPKTA crystal generated 1.15 mW of green light. This crystal showed a normalized conversion efficiency of 1.2 %/Wcm, and its effective nonlinear coefficient was  $d_{eff} = 10.5$  pm/V, which is close to the calculated value of 10.3 pm/V, obtained from  $d_{33} = 16.2$  pm/V [6.2]. Slightly lower values were obtained for the LC-PPKTA crystal (normalized conversion efficiency of 1.03%/Wcm,  $d_{eff} = 9.7$  pm/V) due to the deviation from the ideal duty-cycle of 0.5. The estimated normalized conversion efficiency and the effective nonlinearity value for the ideal duty-cycle in this crystal are  $\eta_{norm} = 1.26$ %/Wcm and  $d_{eff} = 10.7$  pm/V, respectively.

The normalized conversion efficiency distributions across the crystal aperture for the HC-PPKTA and the LC-PPKTA are shown in Fig. 6.6.

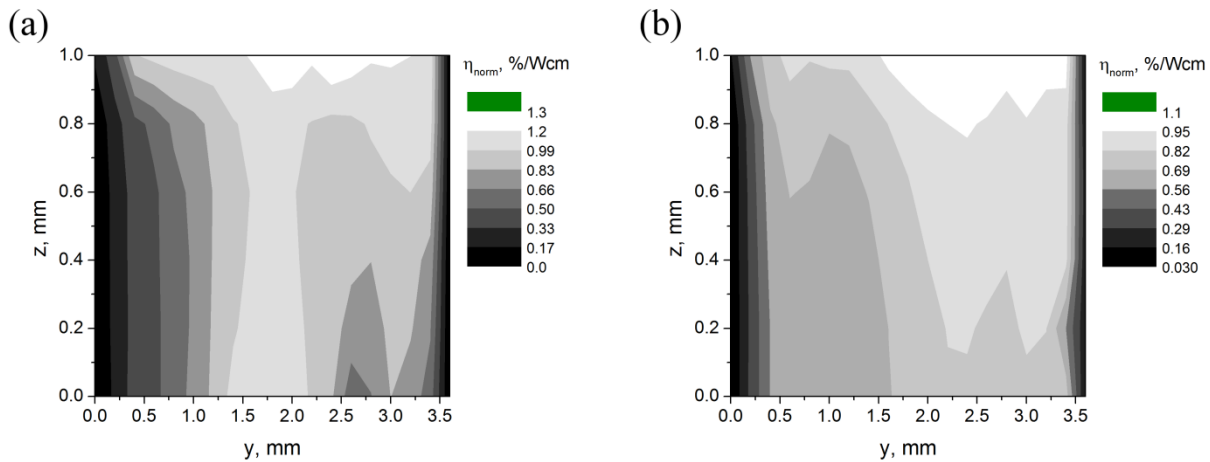


Fig. 6.6. Normalized conversion efficiency distribution across the crystal aperture in (a) the HC-PPKTA, and (b) the LC-PPKTA crystals.

#### 6.4. PPKTA for second harmonic generation

The standard deviation across the  $3 \times 1 \text{ mm}^2$  aperture is 0.23%/Wcm in the HC-PPKTA case, while it is 0.14%/Wcm in the LC-PPKTA case.

The temperature acceptance bandwidth of these crystals was evaluated by tuning the crystal temperature and recording the SHG output, at the pump wavelength of 1066.5 nm. The measurement results for both the HC-PPKTA and the LC-PPKTA crystals are shown in Fig. 6.7.

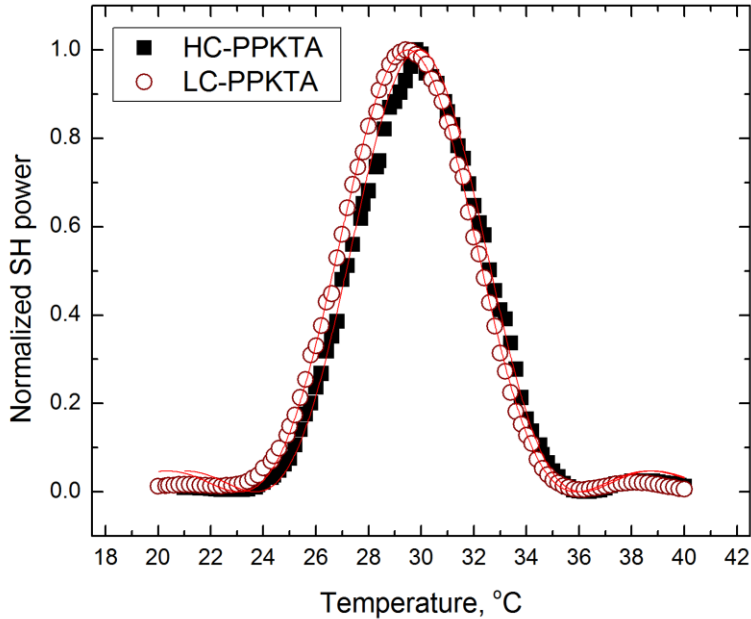


Fig. 6.7. Normalized second harmonic power as a function of the PPKTA crystal temperature.

The temperature acceptance bandwidths are  $\Delta T_{FWHM} = 5.6 \text{ }^\circ\text{C}$  for the HC-PPKTA crystal and  $\Delta T_{FWHM} = 5.7 \text{ }^\circ\text{C}$  for the LC-PPKTA, respectively. These values are similar to those obtained for a high-quality, periodically poled KTP of similar length designed for SHG at 1064 nm [6.3].

The demonstrated ability to implement relatively short period QPM gratings in KTA crystals enables the use of PPKTA for high-power, second harmonic generation in the visible spectral region. Due to their lower linear absorption, the LC-PPKTA crystals should provide superior performance in the high-power SHG applications. In order to prove this assumption, the uncoated PPKTA crystals were placed in a single-pass SHG setup, pumped by a CW Yb-doped fiber laser, capable of providing >100 W maximum output power with a beam quality of  $M^2 < 1.2$ .

The pump beam was focused along the  $x$  axis into the crystal to a beam waist radius of 25  $\mu\text{m}$ . For proper thermal management purposes, the crystals were wrapped in indium foil and placed into a temperature-controlled oven. A slight tilt of the crystal with respect to the pump beam prevented detrimental feedback to the pump laser. The SHG power and the conversion efficiency as a function of pump power for both the LC-PPKTA and the HC-PPKTA crystals are shown in Fig. 6.8.

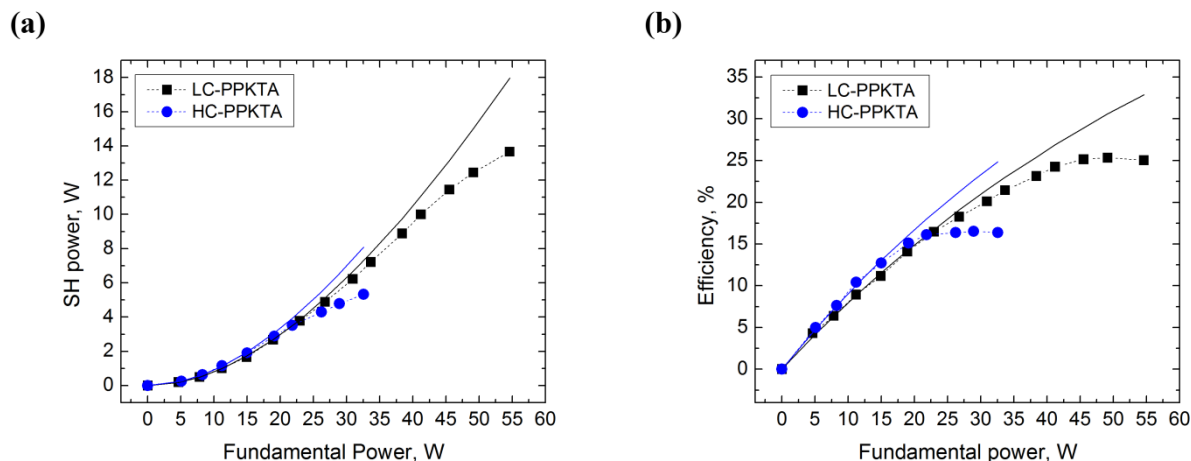


Fig. 6.8. Second harmonic power (a), and conversion efficiency (b) as a function of pump power in the LC-PPKTA and the HC-PPKTA crystals. Solid curves represent the numerical fits.

The theoretical fits are provided by a model based on a numerical solution of the coupled wave equations and spatially resolved heat propagation. This model takes into account the focusing conditions, pump depletion and the linear absorption. However the thermal dephasing effects are not accounted for in this model. From Fig. 6.8 it is clear that, due to the higher linear absorption at 533 nm, thermal dephasing becomes pronounced in the HC-PPKTA crystal at a considerably lower power level, compared to the LC-PPKTA sample. Consequently, the LC-PPKTA generated a maximum power of 13.6 W with a 25% conversion efficiency, while in the HC-PPKTA crystal, the maximum SH power was only 5.3 W with a 17% conversion efficiency. Further improvements in the thermal management, e.g., a reduction of the aperture of the PPKTA crystals, should allow further upscaling of the SH power.

## 6.5. Temperature tuning characteristics

From the OPO and the SHG experiments it became clear that the existing Sellmeier data are not suitable for our KTA crystals. To illustrate this, the tuning of the OPO output wavelength was carried out by varying the OPO PPKTA crystal temperature between 15 and 65 °C. Figure 6.9 shows the measured signal and the calculated idler wavelengths as a function of the crystal temperature. The theoretical tuning curves are based on the Sellmeier equations derived by Fradkin-Kashi *et al.* [6.4], together with the temperature correction proposed by Emanuelli and Arie [6.5]. From Fig. 6.9, it is clear that there is a discrepancy between the calculated and the experimental tuning curves, which might be caused by the differences in the material, for instance, the concentration of the impurities added during the crystal growth to promote the single-domain crystal formation [6.2].

## 6.5. Temperature tuning characteristics

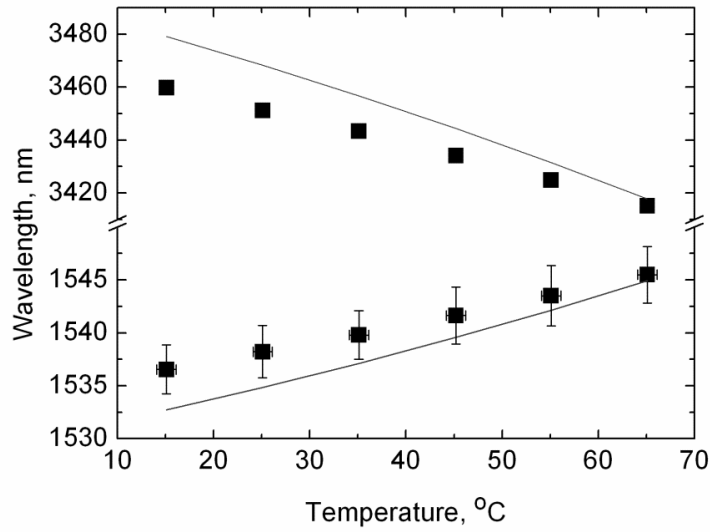


Fig. 6.9. The dependence of the OPO output wavelength on the PPKTA crystal temperature. Squares represent the experimental data, solid lines – the theoretical dependence.

In the SHG case, the dependence of the phase-matched pump wavelength on the crystal temperature was evaluated for both the HC-PPKTA and the LC-PPKTA crystals. In this measurement, the pump beam was kept parallel to the grating vector and the crystal temperature was varied in steps of 2 °C between 20 and 40 °C, while the pump was tuned to give the highest SH output at each step. Figure 6.10 shows the phase-matched pump wavelength as a function of the crystal temperature for these crystals.

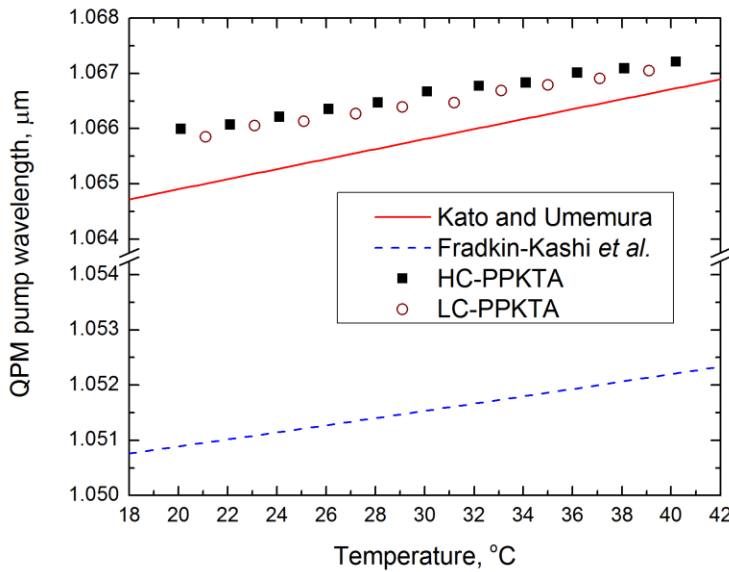


Fig. 6.10. Temperature tuning of the phase-matched pump wavelength in the LC-PPKTA and the HC-PPKTA crystals. Squares and circles represent the experimental data, solid lines – the theoretical dependence.

The dashed curve represents the theoretical prediction based on the Sellmeier equations derived by Fradkin-Kashi *et al.* [6.4], together with the temperature correction, optimized for these equations, proposed by Emanuelli and Arie [6.5]. The large discrepancy between the measured and the calculated values in this case may be due to the fact that these Sellmeier equations were optimized for mid-infrared spectral range and are more suitable for 1  $\mu\text{m}$  pumped OPO applications. The solid curve is calculated using the temperature-corrected Sellmeier equations derived by Kato and Umemura [6.6]. As in the OPO case, here the difference between the experimental and the calculated values can be explained by the small differences in the raw KTA material, which had already been pointed out as a source for the relatively large refractive index differences [6.2, 6.7].

From these measurements it is clear that further studies of the impact of the crystal composition on the refractive index of KTA and the temperature dependence of the refractive index are needed both in the visible and the infrared spectral regions.

## References

- 6.1. G. Rosenman, A. Skliar, Y. Findling, P. Urenski, A. Englander, P. A. Thomas, and Z. W. Hu, "Periodically poled  $\text{KTiOAsO}_4$  crystals for optical parametric oscillation," *J. Phys. D* **32**, L49-L52 (1999).
- 6.2. L. K. Cheng, L. T. Cheng, J. D. Bierlein, F. C. Zumsteg, and A. A. Ballman, "Properties of doped and undoped crystals of single domain  $\text{KTiOAsO}_4$ ," *Appl. Phys. Lett.* **62**, 346 (1993).
- 6.3. V. Pasiskevicius, S. Wang, J. A. Tellefsen, F. Laurell, and H. Karlsson, "Efficient Nd:YAG Laser Frequency Doubling with Periodically Poled KTP," *Appl. Opt.* **37**, 7116-7119 (1998).
- 6.4. K. Fradkin-Kashi, A. Arie, P. Urenski, and G. Rosenman, "Mid-infrared difference-frequency generation in periodically poled  $\text{KTiOAsO}_4$  and application to gas sensing," *Opt. Lett.* **25**, 743-745 (2000).
- 6.5. S. Emanuelli and A. Arie, "Temperature-Dependent Dispersion Equations for  $\text{KTiOPO}_4$  and  $\text{KTiOAsO}_4$ ," *Appl. Opt.* **42**, 6661-6665 (2003).
- 6.6. K. Kato, and N. Umemura, "Sellmeier and thermo-optic dispersion formulas for  $\text{KTiOAsO}_4$ ," in Conference on Lasers and Electro-Optics, CLEO 2004, Technical Digest (CD), (Optical Society of America, 2004), paper CThT35. <http://www.opticsinfobase.org/abstract.cfm?URI=CLEO-2004-CThT35>
- 6.7. K. Kato, "Second-harmonic and sum-frequency generation in  $\text{KTiOAsO}_4$ ," *IEEE J. Quant. Electron.* **30**, 881-883 (1994).

## Chapter 7. Large aperture QPM devices

### 7.1. Large aperture nonlinear crystals

Implementation of large aperture QPM devices is challenging due to the increasingly high voltages required for polarization-switching together with the difficulty of propagating the domain grating through the whole crystal thickness. Periodically poled, Mg-doped congruent LiNbO<sub>3</sub> with thicknesses up to 10 mm and Mg-doped congruent LiTaO<sub>3</sub> with thicknesses of 5 mm have been recently reported [7.1, 7.2]. In these materials, periodic poling was performed at elevated temperatures in order to take advantage of the decreased coercive field. However, the domain structures obtained are still limited in homogeneity due to duty-cycle variations, domain broadening, and domain merging throughout the crystal thickness.

Periodically poled structures in KTP and RTA crystals with a thickness of up to 3 mm have been reported previously [7.3, 7.4]. However in flux-grown KTP, the high ionic conductivity, the inhomogeneous stoichiometry over a single wafer and a poor wafer-to-wafer consistency limits the yield of well-poled samples. RTA has a substantially lower ionic conductivity compared to flux-grown KTP; however, its availability is very limited and, therefore, was not considered as a candidate for large aperture QPM device fabrication.

Improved material properties and the ability to handle higher optical powers make RKTP the best choice for periodic poling of large aperture QPM crystals to date.

### 7.2. Periodic poling of 5 mm thick RKTP crystals

Large aperture QPM devices were implemented in 5 mm thick RKTP crystals. A period of 38.86  $\mu\text{m}$  with a duty-cycle of 0.5 was chosen for a 1064 nm pumped degenerate OPO, generating 2128 nm wavelength at room temperature. Since the currently available poling equipment is capable of providing a maximum voltage of 20 kV, it was not possible to use triangular pulses with these crystals, therefore, they were periodically poled at room temperature by applying 5 ms long square electric field pulses of magnitude 3.2 kV/mm. Since the poling was performed in the low field regime, two consecutive electric field pulses were needed in order to get complete domain reversal under the periodic electrodes. Figure 7.1 shows the ferroelectric domain structure on the patterned face (a) and the non-patterned face (b) of the 5 mm thick RKTP crystal after the first electric field pulse. Because of the high fringing fields at the electrode edges, only the domain tips nucleated at these edges and propagated through the whole 5 mm thickness after the first pulse. Additionally, some domains had already nucleated under the electrodes, although they had not propagated. The domain structure on the patterned face (c) and the non-patterned face (d) of 5 mm thick PPRKTP crystal after the second electric field pulse is also shown in Fig. 7.1.

## 7.2. Periodic poling of 5 mm thick RKTP crystals

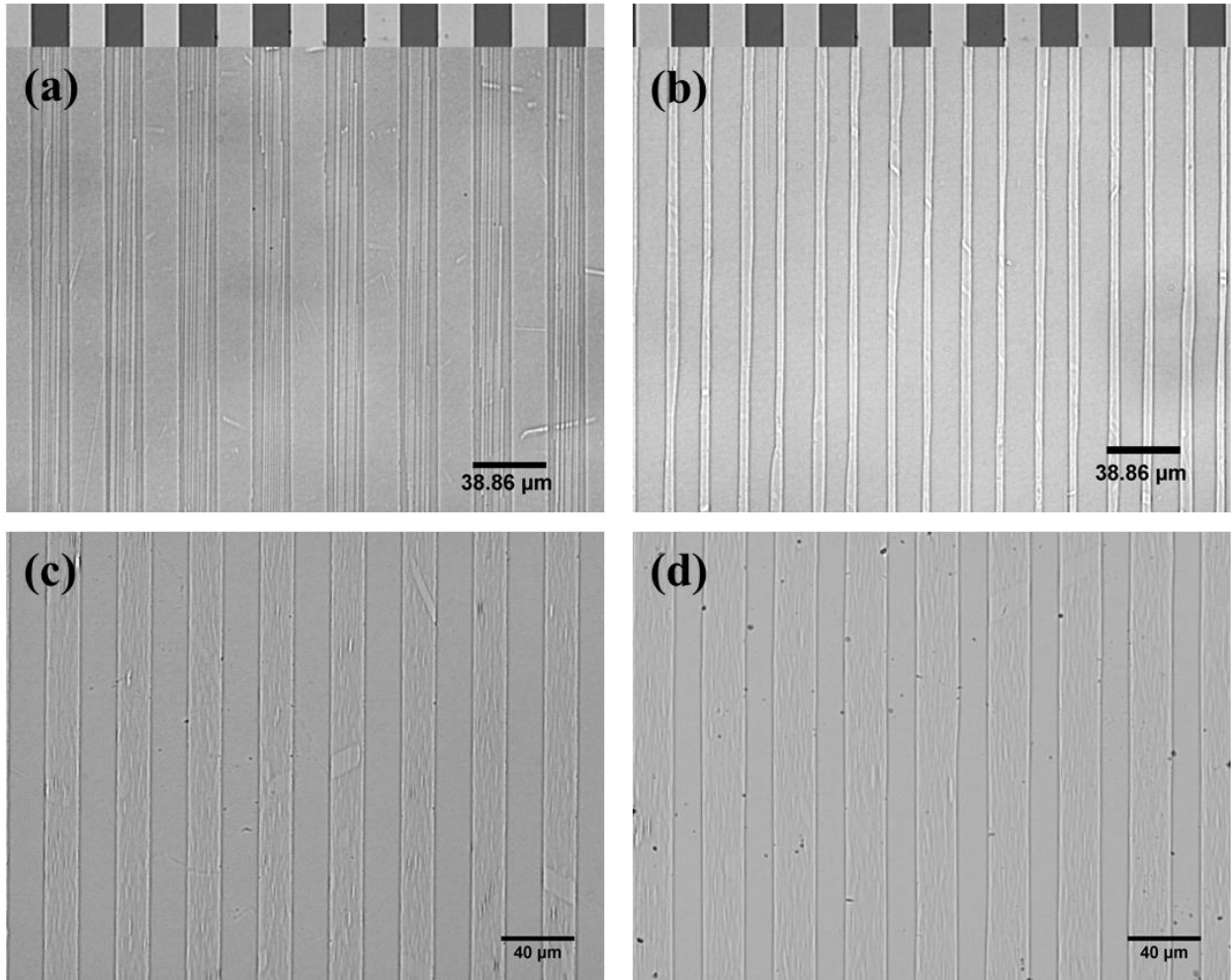


Fig. 7.1. Ferroelectric domain structure on the patterned (a) and the non-patterned (b) faces of 5 mm thick PPRKTP crystal after poling with a single electric field pulse, and the patterned (c), and the non-patterned (d) faces of 5 mm thick PPRKTP crystal after the second electric field pulse. The top parts represent the original metal-photoresist pattern with a duty-cycle of 0.5.

As can be seen, the duty-cycle is close to 0.5 on the patterned face and is approximately 0.57 on the opposite face of the crystal. Taking into account the crystal thickness of 5 mm, the domain broadening is very small. The homogeneity of the sample is well illustrated in Fig. 7.2, which shows the OPO output energy distribution across the crystal aperture of  $8 \times 4 \times 5 \text{ mm}^3$  along the  $x$ ,  $y$  and  $z$  directions, respectively. From this measurement it is clear that the QPM grating is uniform and homogeneous in the bulk of the 5 mm thick PPRKTP crystal.

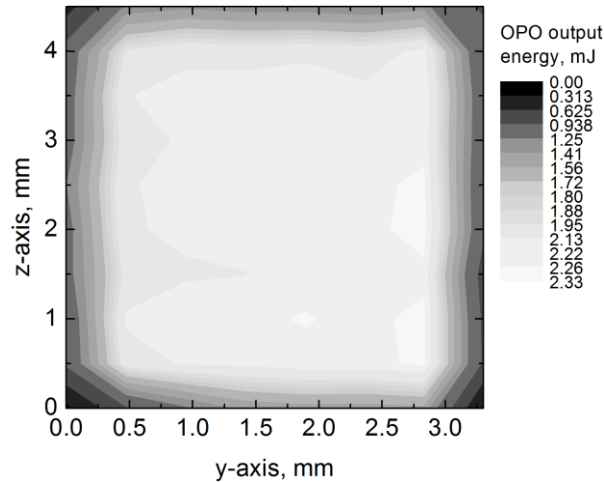


Fig. 7.2. OPO output energy distribution in the  $yz$  plane of the PPRKTP crystal.

The possibility of periodic poling large aperture crystals with a shorter period was also assessed. A period of  $\Lambda = 9.01 \mu\text{m}$ , with a duty-cycle of 0.4, was chosen for SHG at 1064 nm. Again, due to the high voltage requirements, square electric field pulses had to be employed, as in the large period case. Applying two consecutive 5 ms long square electric field pulses with a magnitude of 3.2 kV/mm gave the best periodic poling results, as shown in Fig. 7.3.

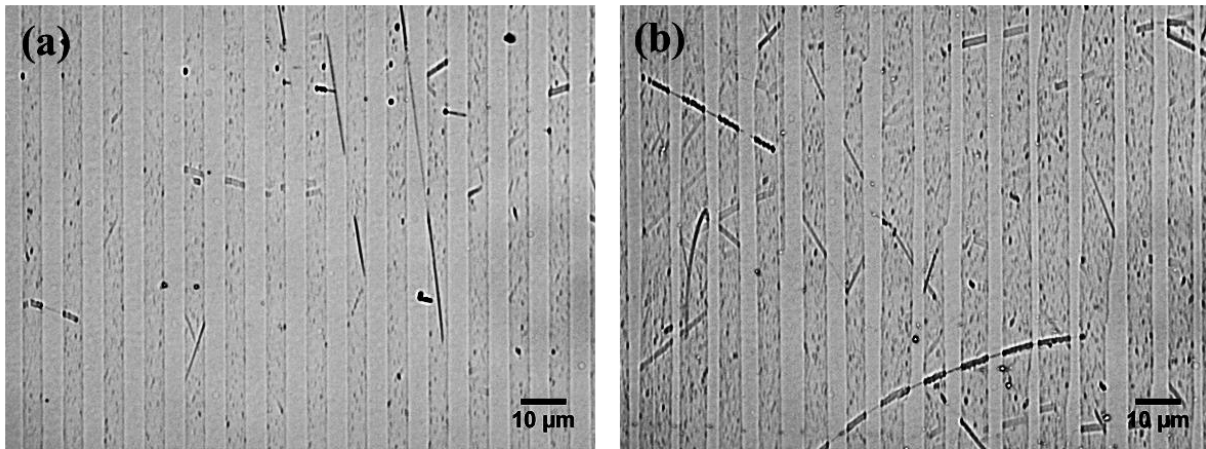


Fig. 7.3. Ferroelectric domain structure on (a) the patterned, and (b) the non-patterned faces of a 5 mm thick PPRKTP crystal with period of  $9.01 \mu\text{m}$ .

The duty-cycle of the inverted domains is close to the ideal case of 0.5 on the patterned face of the crystal. On the non-patterned face, however, the QPM grating is less uniform, and the duty-cycle varies from 0.35 to 0.7 which may be a consequence of the non-optimal poling conditions. On the other hand, taking into account that the aspect ratio of the domains is 1:1100, RKTTP demonstrates remarkably little domain broadening. Periodic poling with triangular pulses and with higher electric field magnitude might improve the QPM grating quality in this case. Figure 7.4 shows the SHG output energy distribution across the aperture in one of the 5 mm thick PPRKTP crystals.

### 7.3. Large aperture PPRKTP OPO performance

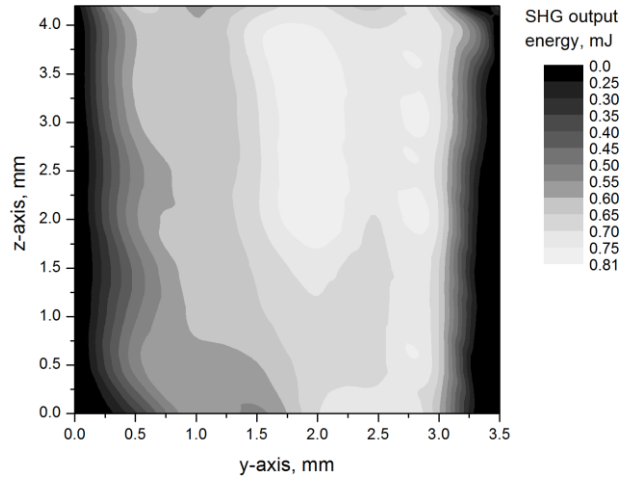


Fig. 7.4. SHG output energy distribution in  $yz$  plane of the PPRKTP crystal.

As can be seen from Fig. 7.4, the QPM grating is less homogeneous in this crystal compared to larger period case.

### 7.3. Large aperture PPRKTP OPO performance

A large-aperture OPO PPRKTP crystal was pumped by a seeded, diode-pumped, single-longitudinal mode Nd:YAG laser and amplifier system providing 12 ns long pulses at 1064 nm wavelength and at a 100 Hz repetition rate with a maximum output energy of 130 mJ. The reflectivity of the OPO output coupler was 30% at 2.1  $\mu\text{m}$ . The OPO cavity length was set to 20 mm, while the temperature was stabilized just above room temperature. The  $z$ -polarized pump was expanded and collimated into a beam with a  $\sim 2$  mm radius and then launched along the  $x$ -axis into the crystal. Figure 7.5 shows the pump depletion and the combined signal and idler efficiency as a function of the pump energy.

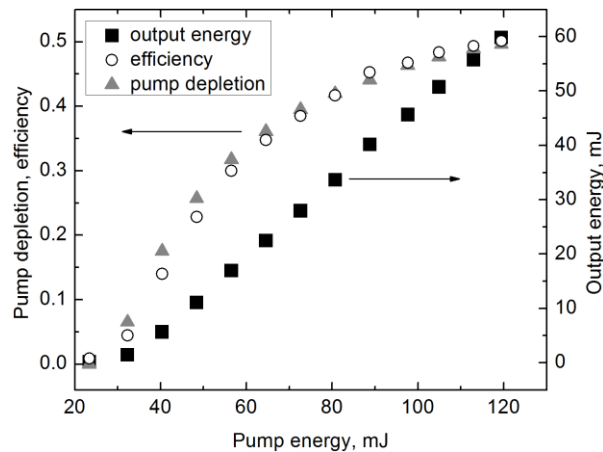


Fig. 7.5. The OPO output energy, conversion efficiency, and the pump depletion for different pump energies inside the crystal.

The temperature tuning properties of the OPO were studied by varying the crystal temperature between 10 and 70 °C. Figure 7.6(a) shows the experimental data together with the theoretical tuning curves based on the Sellmeier equations for KTP derived by Fradkin *et al.* [7.5], including the temperature correction proposed by Emanuelli and Arie [7.6], and the temperature-corrected Sellmeier equations by Kato and Takaoka [7.7].

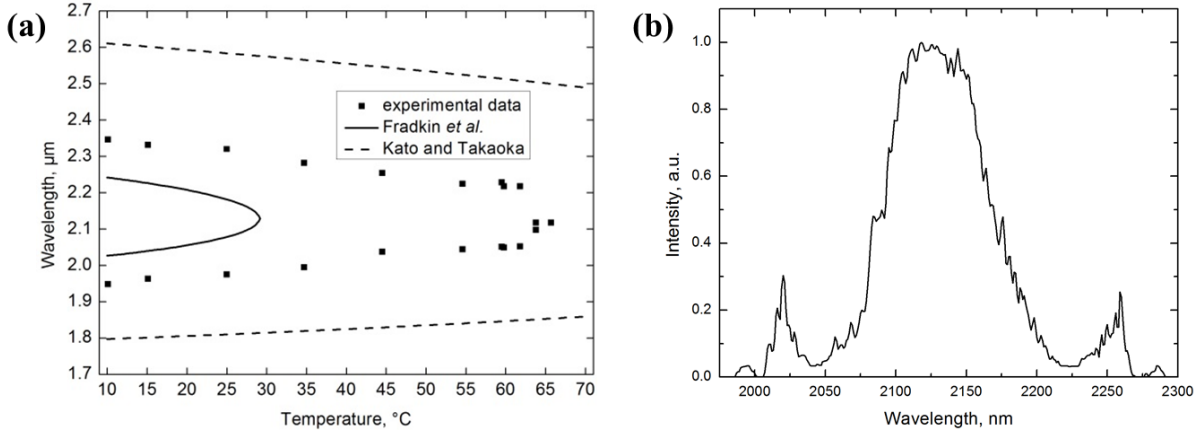


Fig. 7.6. Temperature tuning of the signal and the idler waves (a), and the OPO output spectrum at degeneracy with the crystal temperature set to 50 °C (b).

The discrepancy between the measured and the theoretical temperature tuning curves may be explained by the fact that neither of the Sellmeier equations were derived at this wavelength span.

In order to investigate the spectral properties of the OPO at degeneracy, the crystal temperature was set to 50 °C and the OPO output spectrum was recorded, as shown in Fig. 7.6(b). The measurement was performed using a spectrometer with a PbSe detector. The output is centered at a wavelength of  $\sim 2.1$   $\mu\text{m}$  with a FWHM of 80 nm. Two side peaks, with a separation in frequency of  $\sim 16$  THz from each other can also be seen in the recorded spectrum. The frequency of 8 THz corresponds to the lowest-frequency infrared-active TO phonon mode in KTP [7.8]. Therefore, these peaks can be attributed to a four-wave mixing process, assisted by intra-cavity stimulated Raman scattering [7.9], and followed by the amplification of the sidebands by the second order parametric process. Narrowing down the intra-cavity gain by using a volume Bragg grating should effectively remove the gain from this process.

## References

- 7.1. H. Ishizuki and T. Taira, "Fabrication of 10-mm-thick periodically poled Mg-doped congruent LiNbO<sub>3</sub> device for high-energy wavelength conversion," in Conference on Lasers and Electro-Optics, CLEO 2012, Technical Digest (CD), (Optical Society of America, 2012), paper CTh1B.1.
- 7.2. H. Ishizuki and T. Taira, "High-energy quasi-phase-matched optical parametric oscillation using Mg-doped congruent LiTaO<sub>3</sub> crystal," *Opt. Express* **18**, 253-258 (2010).
- 7.3. H. Karlsson, M. Olsson, G. Arvidsson, F. Laurell, U. Bäder, A. Borsutzky, R. Wallenstein, S. Wickström, and M. Gustafsson, "Nanosecond optical parametric oscillator based on large-aperture periodically poled RbTiOAsO<sub>4</sub>," *Opt. Lett.* **24**, 330-332 (1999).
- 7.4. M. Peltz, U. Bäder, A. Borsutzky, R. Wallenstein, J. Hellström, H. Karlsson, V. Pasiskevicius, and F. Laurell, "Optical parametric oscillators for high pulse energy and high average power operation based on large aperture periodically poled KTP and RTA," *Appl. Phys. B* **73**, 663-670 (2001).
- 7.5. K. Fradkin, A. Arie, A. Skliar, G. Rosenman, "Tunable midinfrared source by difference frequency generation in bulk periodically poled KTiOPO<sub>4</sub>," *Appl. Phys. Lett.*, **74**, 914-916 (1999).
- 7.6. S. Emanuelli, A. Arie, "Temperature-dependent dispersion equations for KTiOPO<sub>4</sub> and KTiOAsO<sub>4</sub>," *Appl. Opt.* **42**, 6661-6665 (2003).
- 7.7. K. Kato, E. Takaoka, "Sellmeier and thermo-optic dispersion formulas for KTP," *Appl. Opt.* **41**, 5040-5044 (2002).
- 7.8. V. Pasiskevicius, C. Canalias, and F. Laurell, "Highly efficient stimulated Raman scattering of picosecond pulses in KTiOPO<sub>4</sub>," *Appl. Phys. Lett.* **88**, 041110 (2006).
- 7.9. V. Pasiskevicius, A. Fragemann, F. Laurell, R. Butkus, V. Smilgevicius, and A. Piskarskas, "Enhanced stimulated Raman scattering in optical parametric oscillators from periodically poled KTP," *Appl. Phys. Lett.* **82**, 325-327 (2003).

## Chapter 8. Short-period QPM devices for blue light generation

### 8.1. Need of short-period QPM structures

Many important applications, such as high density optical information storage [8.1], biomedical research [8.2], laser cooling of atoms [8.3] and spectroscopy [8.4] demand coherent radiation sources operating in the blue spectral region. Most commonly, blue light is generated by LBO [8.5, 8.6] or BBO [8.7, 8.8] crystals in birefringent phase matching configurations. Unfortunately, there is no simple way to implement QPM in these materials. In addition, these materials exhibit relatively low effective nonlinearities and their hygroscopic properties add additional complications [8.9].

KTP is a widely used QPM nonlinear material which is also free of photorefractive damage issues. The use of the KTP isomorphs in the blue spectral region, together with the possibility of implementing QPM, may bring additional advantages, such as the ability to employ the highest nonlinearity available in this material and the use of noncritical phase matching. QPM structures with periods of the order of a few micrometers are needed for second harmonic generation in the blue spectral region. RKTP is an ideal candidate for the fabrication of such short-period QPM devices. Additionally, this material has a lower susceptibility to gray-tracking as compared to regular flux-grown KTP, which is beneficial for applications in the visible region (see Section 4.5). For low-intensity fundamental beams (below  $\sim 300$  MW/cm<sup>2</sup>), the shortest wavelength where the KTP isomorphs could be used, is given by the material bandgap of about 3.5 eV (355 nm). For ultrashort pulses, with higher peak intensities, where the nonlinear absorption becomes important, the short wavelength range is further restricted, therefore, the effects of multi-photon absorption and the increased thermal loading in PPKTP and in PPRKTP on the SHG efficiency at wavelengths below 400 nm, need to be evaluated.

### 8.2. Periodic poling of short-period QPM structures

For SHG at 796 nm, the RKTP crystals were patterned with a period of 3.18  $\mu\text{m}$  and with an electrode duty-cycle of 0.2. For comparison purposes, KTP crystals were also patterned with the same period and with an electrode duty-cycle of 0.1. Both RKTP and KTP crystals were periodically poled with 5 ms long triangular pulses with the magnitudes of 7.7 and 6.0 kV/mm, respectively. Figure 8.1 shows the resulting domain structure revealed on the polar faces after selective chemical etching on (a) the patterned face and (b) the non-patterned face of the PPRKTP crystal, and (c) the patterned face and (d) the non-patterned face of the PPKTP crystal. The inverted ferroelectric-domain duty-cycle close to 0.47 was obtained on both polar faces of the PPRKTP crystal, and is a result of the periodic poling in the high field regime. In the PPKTP case, substantial domain broadening can be observed, resulting in a duty-cycle close to 0.62 on the patterned face; however, the domain structure did not propagate homogeneously through the crystal bulk.

### 8.3. Frequency conversion in the blue region

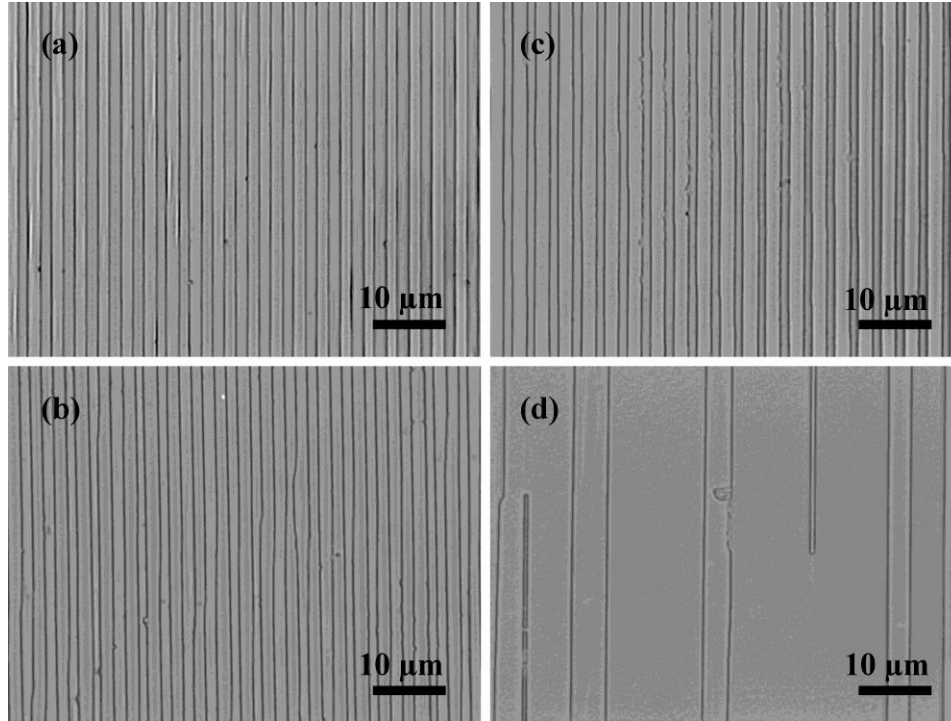


Fig. 8.1. Ferroelectric domain structure on patterned (a) and non-patterned (b) faces of PPRKTP, and patterned (c) and non-patterned (d) faces of PPKTP crystal. The period is  $\Lambda = 3.18 \mu\text{m}$ .

### 8.3. Frequency conversion in the blue region

The uncoated PPKTP and PPRKTP crystals shown in Fig. 8.1 were evaluated in a CW SHG setup. The PPRKTP crystal showed a normalized conversion efficiency of 1.79 %/Wcm and an effective nonlinear coefficient  $d_{eff} = 8.3 \text{ pm/V}$ , which is somewhat lower than the calculated value  $d_{eff} = 2d_{33}/\pi = 10 \text{ pm/V}$  [8.10]. Indeed, this should be expected since the duty-cycle of the domain structure deviates from the perfect one. The highest normalized conversion efficiency achieved in PPKTP crystals was 1.1 %/Wcm when the fundamental beam was propagating close to the patterned crystal face. The effective nonlinear coefficient in this case was  $d_{eff} = 6.45 \text{ pm/V}$ .

In order to evaluate the performance of the PPKTP and the PPRKTP crystals at higher intensities a femtosecond Ti:Sapphire laser operating at a 76 MHz repetition rate was used. In order to compare the relatively long (6.5 mm) crystals, the fundamental beam was focused to a waist radius of 50  $\mu\text{m}$  along the  $x$ -axis in the crystal and the pulse length was adjusted to 138 fs. The calculated wavelength acceptance bandwidth of the 6.5 mm long PPKTP crystals was 0.17 nm. The temperature of each crystal was stabilized to 25 °C. The generated second harmonic average power and the efficiency, both in the PPKTP and the PPRKTP, are shown in Fig. 8.2(a).

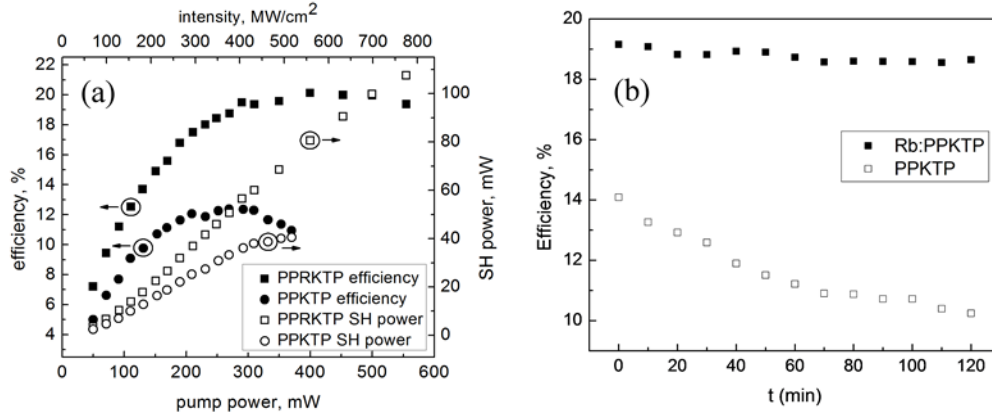


Fig. 8.2. (a), SH average power (open symbols) and SHG efficiency (solid symbols) in the 6.5 mm-long PPKTP (circles) and the PPRKTP (squares) for 138 fs long fundamental pulses at 796 nm. (b), long-term variation of the SHG efficiency at  $0.4 \text{ GW/cm}^2$ .

Due to the higher quality of the PPRKTP structures, the efficiency in this QPM device is substantially higher than that in the PPKTP. Strong gray-tracking in the PPKTP at a fundamental peak intensity of  $0.5 \text{ GW/cm}^2$  could be observed. This process requires the presence of both the intense near-infrared and the generated SH blue light. While increasing the fundamental average power further, the nonlinear absorption-induced gray-tracking leads to thermal dephasing and to an eventual breakdown of the crystal. Under the same pumping conditions, the PPRKTP did not show any signs of gray-tracking even at the peak intensity of  $0.77 \text{ GW/cm}^2$ . The time-dependence of the conversion efficiencies over two hours of continuous operation in both materials is shown in fig. 8.2(b). The peak intensity here was  $0.4 \text{ GW/cm}^2$ . This clearly indicates the long-term color-center formation effect in the PPKTP crystal, which was not observed in the case of PPRKTP.

When the group velocity mismatch is large, higher conversion efficiency for femtosecond pulses can normally be achieved by employing short nonlinear crystals and tight focusing. Therefore, the length of the PPRKTP crystals was reduced to 1 mm. The wavelength acceptance bandwidth of the 1 mm long PPRKTP crystals was estimated to be 1.1 nm. The fundamental pulse length in this case was 85 fs. The focusing conditions remained the same as with the 138 fs pulses. Figure 8.3 shows the SH average power and the conversion efficiency as a function of the average pump power in this PPRKTP crystal. From Fig. 8.3 it is evident that the SHG efficiency in the shorter PPRKTP crystals is actually lower than in the longer ones, and the efficiency is decreasing at the fundamental peak intensities above  $1 \text{ GW/cm}^2$ . Again, no visible gray-tracking could be seen in the PPRKTP crystals even after operation at peak intensities of  $1.5 \text{ GW/cm}^2$ .

The saturation of the SHG efficiency and the lower saturated efficiency in shorter crystals cannot be explained only by thermal effects, which should be much more pronounced in longer crystals. The group velocity dispersion is also reduced in shorter crystals.

### 8.3. Frequency conversion in the blue region

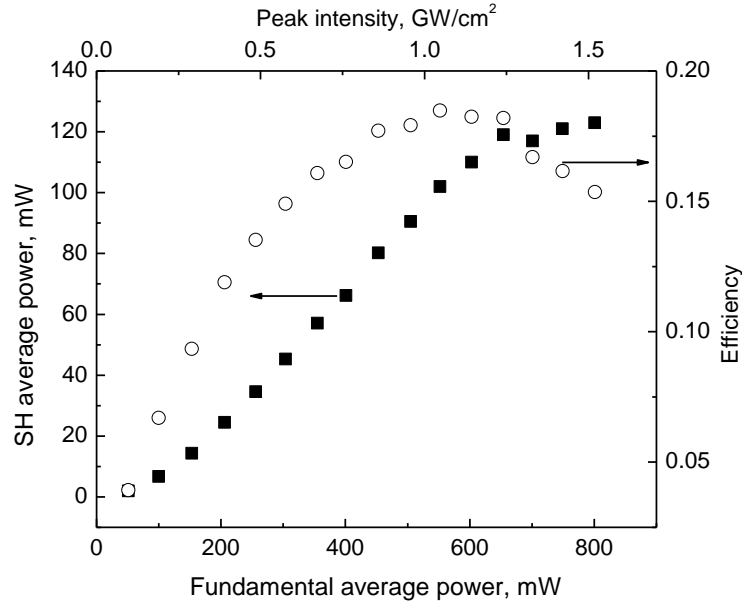


Fig. 8.3. Second harmonic average power (solid squares) and the conversion efficiency (open circles) in a 1 mm long PPRKTP crystal. Pump: 85 fs pulses at 76 MHz repetition rate, 796 nm wavelength.

The strongest process limiting the efficiency of the frequency doubling of 796 nm high-peak power pulses is two photon absorption (TPA). It should be noted that the energy of the fundamental frequency photon is smaller than one half of the bandgap of RKTP, therefore the most probable is the simultaneous absorption of the fundamental and the second harmonic photons. The effect of the TPA is clearly seen in an open aperture  $z$ -scan measurement, as shown in Fig. 8.4.

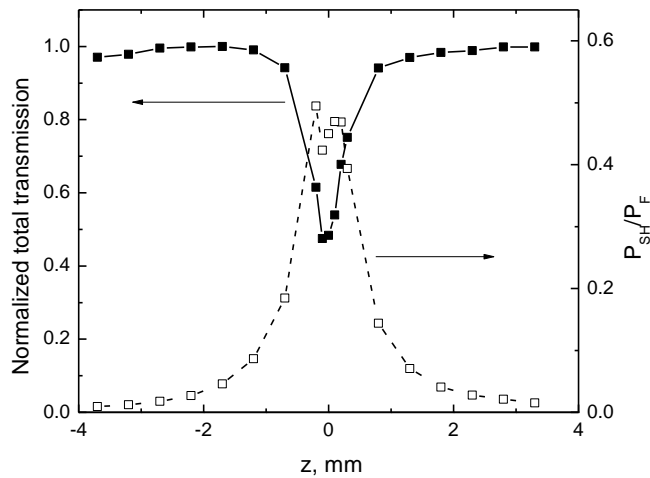


Fig. 8.4. Normalized total transmission (solid squares) and the ratio of the second harmonic and the fundamental powers after the crystal (open squares) as a function of crystal position with respect to the beam waist. The maximum intensity at the beam waist is 5.8 GW/cm<sup>2</sup>. The PPRKTP crystal length is 1 mm, pulse length is 85 fs.

In this measurement, the beam waist radius was 13  $\mu\text{m}$  and the crystal temperature was stabilized to 25  $^{\circ}\text{C}$ , corresponding to the most efficient SHG in the CW experiments. The total combined fundamental and second harmonic power transmission decreases by 53% when the crystal is at the beam waist position. At this position, about 50% of the total transmitted power is actually in the second harmonic. Moreover, such a reduction of the transmitted power was not observed in the single-domain RKTP crystals.

It is clear that the two-photon absorption involving both the fundamental and the second harmonic photons is the main source of the losses which, in turn, limits the obtainable SHG efficiency in this extreme SHG regime. As a result, the SHG efficiency at 796 nm, as normalized to the incident fundamental power, does not exceed 20% even for the short PPRKTP crystals and for tight focusing, in strong contrast to the femtosecond SHG at 1  $\mu\text{m}$  or the CW SHG at 846 nm, where the multi-photon absorption process is absent or significantly reduced [8.11, 8.12]. The above experiments could not be performed with the PPKTP due to crystal damage associated with an increased absorption by induced color-centers.

## References

- 8.1. T. Tanaka, K. Takahashi, K. Sako, R. Kasegawa, M. Toishi, K. Watanabe, D. Samuels, and M. Takeya, "Littrow-type external-cavity blue laser for holographic data storage," *Appl. Opt.* **46**, 3583-3592 (2007).
- 8.2. T. Wunderer, J. E. Northrup, Z. Yang, M. Teepe, N. M. Johnson, P. Rotella, and M. Wraback, "Nitride VECSELs as Light Sources for Biomedical Applications," Conference on Lasers and Electro-Optics (CLEO 2013), San Jose, USA, June 9-14 (2013), JM3O.1.
- 8.3. S. Kobtsev, B. Lev, J. Fortagh, and V. Baraulya, "Powerful narrow-line source of blue light for laser cooling Yb/Er and Dysprosium atoms," *Proc. SPIE* **7578**, 75782F (2010).
- 8.4. O. M. Marago, B. Fazio, P. G. Gucciardi, and E. Arimondo, "Atomic gallium laser spectroscopy with violet/blue diode lasers," *Appl. Phys. B* **77**, 809-815 (2003).
- 8.5. Y. Asakawa, H. Kumagai, K. Midorikawa, M. Obara, "50% frequency doubling efficiency of 1.2-W cw Ti:sapphire laser at 746 nm," *Optics Commun.* **217**, 311-315 (2003).
- 8.6. J. Zhang, J. Y. Huang, H. Wang, K. S. Wong, and G. K. Wong, "Second-harmonic generation from regeneratively amplified femtosecond laser pulses in BBO and LBO crystals," *J. Opt. Soc. Am. B* **15**, 200-209 (1998).
- 8.7. T. Kanai, X. Zhou, T. Sekikawa, S. Watanabe, and T. Togashi, "Generation of subterawatt sub-10-fs blue pulses at 1–5kHz by broadband frequency doubling," *Opt. Lett.* **28**, 1484-1486 (2003).
- 8.8. W.-L. Zhou, Y. Mori, T. Sasaki, and S. Nakai, "High-efficiency intracavity continuous-wave ultraviolet generation using crystals CsLiB<sub>6</sub>O<sub>10</sub>, β-BaB<sub>2</sub>O<sub>4</sub> and LiB<sub>3</sub>O<sub>5</sub>," *Opt. Commun.* **123**, 583-586 (1996).
- 8.9. Z. Lin, L. F. Xu, R. K. Li, Z. Wang, C. Chen, M.-H. Lee, E. G. Wang, and D.-S. Wang, "Ab initio study of the hygroscopic properties of borate crystals," *Phys. Rev. B* **70**, 233104 (2004).
- 8.10. M. V. Pack, D. J. Armstrong, and A. V. Smith, "Measurement of tensors of KTiOPO<sub>4</sub>, KTiOAsO<sub>4</sub>, RbTiOPO<sub>4</sub> RbTiOAsO<sub>4</sub>," *Appl. Opt.* **43**, 3319-3323 (2004).
- 8.11. A. A. Lagatsky, C. T. A. Brown, W. Sibbett, S. J. Holmgren, C. Canalias, V. Pasiskevicius, F. Laurell, and E. U. Rafailov, "Efficient doubling of femtosecond pulses in aperiodically and periodically poled KTP crystals," *Opt. Express* **15**, 1155-1160 (2007).
- 8.12. F. Torabi-Goudarzi, and E. Riis, "Efficient cw high-power frequency doubling in periodically poled KTP," *Opt. Commun.* **227**, 389–403 (2003).

## Chapter 9. Sub- $\mu\text{m}$ QPM devices

### 9.1. Introduction

Second-order nonlinear interactions involving counter-propagating waves demand QPM periods on the order of the scale of the optical wavelength. Even though such QPM structures were already demonstrated in KTP [9.1-9.3], their fabrication remains a challenge. First, standard photolithography is applicable only to domain sizes larger than  $1\ \mu\text{m}$ . Second, the electrode fringing fields and the lateral domain growth become increasingly important when the domain sizes are in the sub- $\mu\text{m}$  range, limiting the quality and the yield of periodically poled structures. Therefore, a reliable structuring technology for sub- $\mu\text{m}$  QPM gratings needs to be developed.

### 9.2. Periodic poling of sub- $\mu\text{m}$ QPM devices

In order to create patterns with sub- $\mu\text{m}$  periods, an in-house built UV-laser lithography system has been used. A schematic setup of this system is shown in Fig. 9.1.

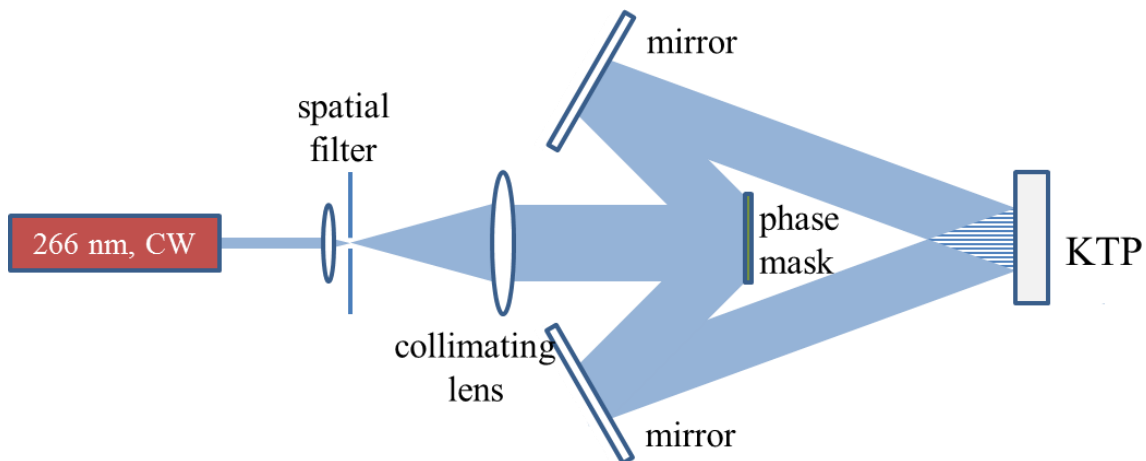


Fig. 9.1. UV laser lithography system for sub- $\mu\text{m}$  period patterning.

A frequency-quadrupled, CW single-mode Nd:YVO<sub>4</sub> laser, operating at 266 nm wavelength, was employed as an exposure source. The laser beam is cleaned up using a spatial filter, then expanded and collimated. Using a reflective diffraction grating, the collimated beam is then split into the +1 and -1 diffraction orders, which are then recombined using high-reflective mirrors to form an interference fringe pattern. The period of the interference pattern can be tuned by adjusting the angles and positions of the mirrors used to reflect the two diffraction orders. The interference pattern is then exposed to a UV26 photoresit layer deposited on the  $c$  face of the RKTP crystal. A pattern profile, achieved using this lithography method, is shown in Fig. 9.2.

## 9.2. Periodic poling of sub- $\mu\text{m}$ QPM devices

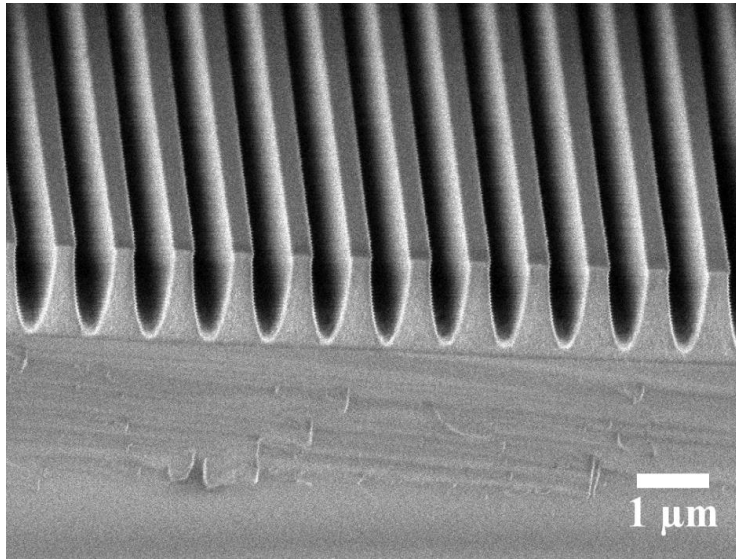


Fig. 9.2. Scanning electron microscope image of the interference pattern profile, exposed in 1.8  $\mu\text{m}$  thick UV26 photoresist, using an in-house built UV lithography system.

The duty-cycle of the openings in the pattern varies at the crystal surface. This variation may result in a non-uniform electrical contact, therefore, a rectangularly shaped pattern profile with a controlled duty-cycle is preferred. Nevertheless, the pattern shown in Fig. 9.2 can be used to evaluate the potential of RKTP for fabrication of QPM devices with sub- $\mu\text{m}$  periods.

For this purpose, RKTP crystals were patterned with a grating period of 690 nm and an aluminum electrode was deposited in the photoresist openings. The samples were poled with 2.5 ms long triangular pulses with a maximum field magnitude of 8 kV/mm. As expected, defects in the photoresist grating prevented uniform electrical contact, resulting in a non-uniform domain grating. However, successful periodic poling was achieved in the regions with good electrical contact. Figure 9.3 shows scanning electron microscope (SEM) images of the etched domain pattern on (a) the patterned face and (b) the non-patterned face of one of the PPRKTP crystals.

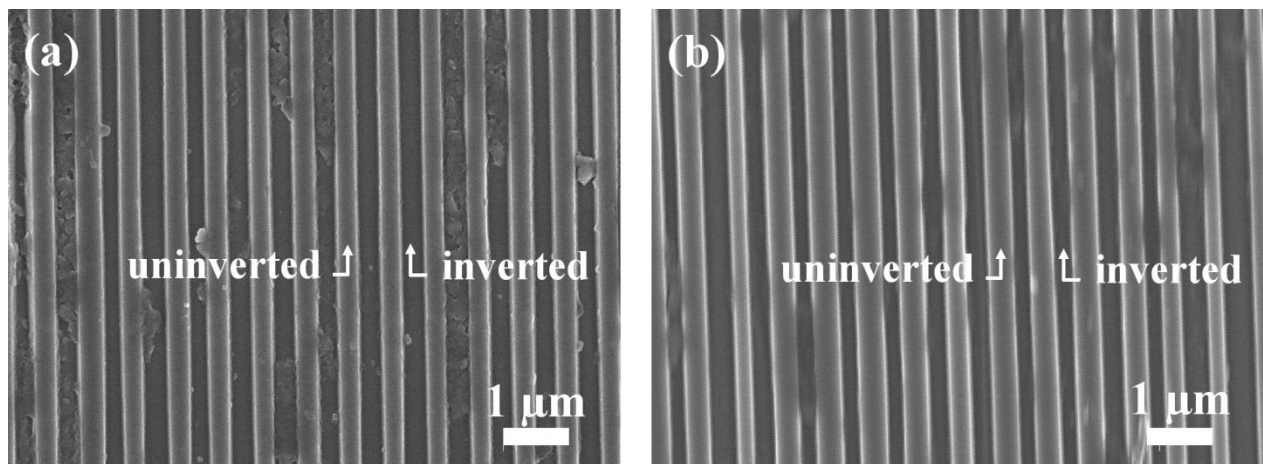


Fig. 9.3. Scanning electron microscope images of patterned (a) and non-patterned (b) faces of the RKTP crystal poled with a period of 690 nm.

The duty-cycle of the inverted domains on the patterned face was 0.49, whereas it varied between 0.45 and 0.6 in the non-patterned face in this PPRKTP crystal. This shows that domain broadening in RKTP is limited even when poling sub- $\mu\text{m}$  periods.

### 9.3. Self-assembled sub- $\mu\text{m}$ domains in RKTP

As discussed above, the fabrication of sub- $\mu\text{m}$  domain structures is still challenging, therefore, it is desirable to explore alternative techniques. The properties of the polar faces and the ferroelectric-electrode interface strongly influence the dynamics of the polarization switching. Indeed, recently, a few novel sub- $\mu\text{m}$  self-organized domain formation techniques in  $\text{LiNbO}_3$  (LN) have been demonstrated, based on the modification of the ferroelectric surface via interaction with the intense UV light [9.4] or via ion implantation [9.5]. Unfortunately, the trigonal crystal structure of LN favors a sub- $\mu\text{m}$  self-organized surface domain formation along the three equivalent symmetry directions in the crystal, resulting in a three-fold ray pattern of sub- $\mu\text{m}$  ferroelectric domains on the crystal surface [9.4, 9.6]. On the other hand, the domain anisotropy of RKTP suggests that the modification of the polar surfaces of this material may be a valid route to obtain one-dimensional bulk sub- $\mu\text{m}$  ferroelectric domain structures.

For this purpose, RKTP crystals were placed in a KOH and  $\text{KNO}_3$  aqueous solution (molar ratio:  $\text{KOH}:\text{KNO}_3:\text{H}_2\text{O} = 1.8:1:11.2$ ) at a temperature of  $135^\circ\text{C}$  for 2-3 minutes. Afterwards, the crystals were contacted to the poling circuit and poled applying single 5 ms long symmetric triangular electric field pulses of magnitude 4.8 – 6.4 kV/mm. The poling resulted in a quasi-periodic domain grating that extends over the whole poled region, and was revealed by selectively etching the crystals using the same solution. The width of the inverted domains, as well as the distance between the neighbouring domains, were systematically measured in several locations of each sample with a scanning electron microscope (SEM) in order to extract statistical data. Figure 9.4 shows typical domain structure on (a) former  $c^-$  and (b) former  $c^+$  face of one of the self-assembled RKTP (SA-RKTP) crystals.

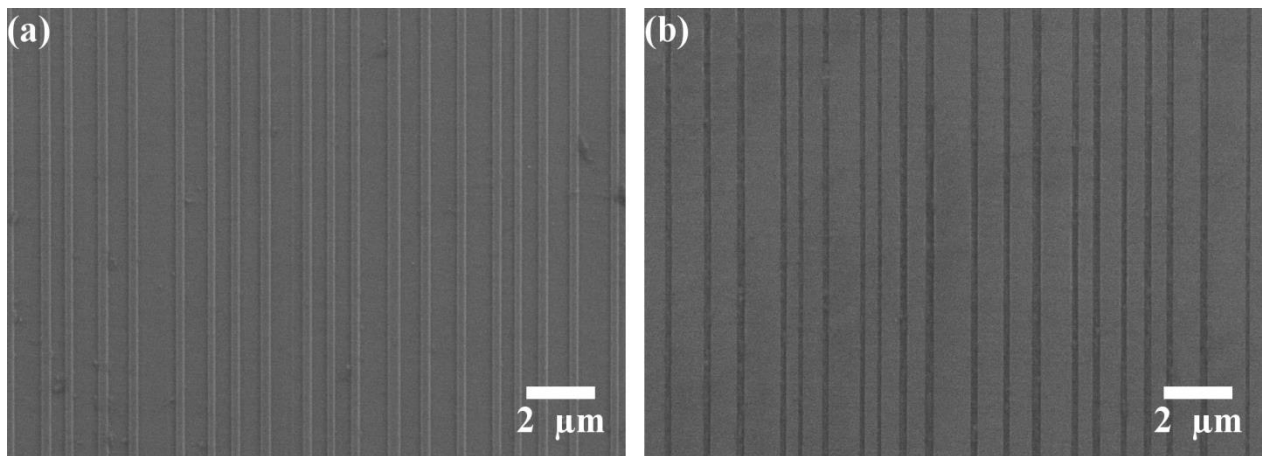


Fig. 9.4. Scanning electron microscope images of the domain structure on (a) the former  $c^-$  face and (b) the former  $c^+$  face of a chemically treated RKTP sample, poled with planar electrodes.

### 9.3. Self-assembled sub- $\mu\text{m}$ domains in RKTP

The average domain size on the former  $c^-$  face of the crystal is  $225 \pm 75$  nm and the average domain periodicity is  $650 \pm 200$  nm. Since the domain nucleation in RKTP starts preferentially on the  $c^-$  face, and the domain propagation is directed towards the  $c^+$  surface, the domains measured on the former  $c^+$  face are slightly smaller with an average domain size of  $175 \pm 75$  nm. Such domain sizes and periodicities are characteristic to all chemically treated RKTP samples poled with symmetric triangular electric field pulses with the magnitudes in the range of 5.6 – 6.0 kV/mm. Figure 9.5 shows the obtained domain size and periodicity as a function of the poling field. Note that the domain width along the  $x$  direction remains relatively constant for the investigated electric field range. Since the domain nucleation rate depends on the electric field magnitude, in crystals poled with low electric fields the domain structure is less dense, and the domains have not propagated along the polar axis. With moderate electric field, the domain density increases, shortening the distances among them, and the period becomes more uniform as can be seen from the smaller standard deviation. At the highest electric field, domain merging starts to occur, increasing the overall domain size and thus decreasing the domain density.

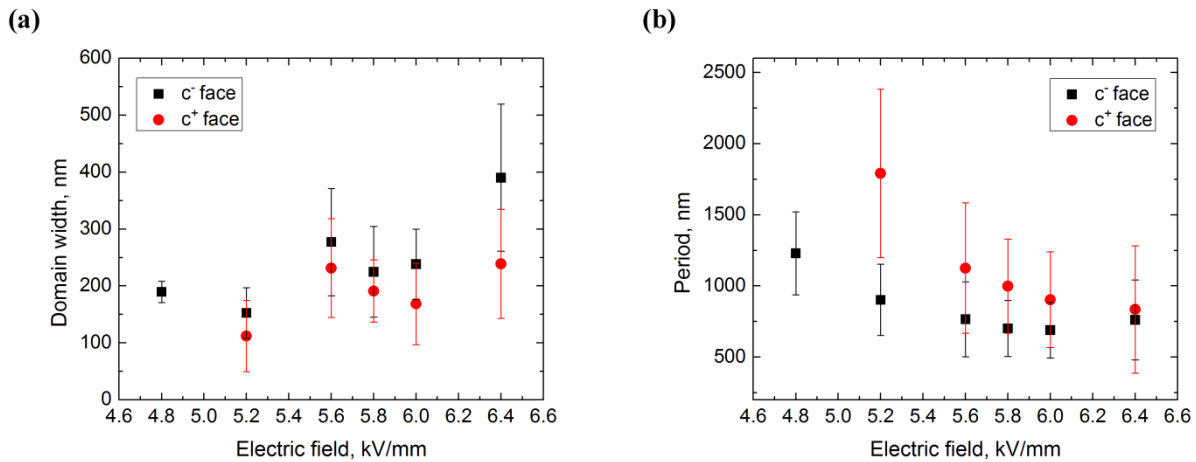


Fig. 9.5. (a) domain size, and (b) periodicity dependence on the E-field magnitude. The error bars represent standard deviation of the distribution.

In order to gain a better understanding of the self-assembled domain grating formation, samples treated at different temperatures and with different solutions were studied. No significant difference either in the periodicity or the domain size could be observed when the solution temperature was varied between 75 and 200 °C. In addition, it is worth noting that at 200 °C, the surface corrugation resulting from the etching was quite severe with deep ( $> 4 \mu\text{m}$ ) etch pits, however, it did not affect the resulting domain width and density. This suggests a surface charge-mediated mechanism rather than a surface mechanical-damage mechanism. Indeed, dry etching of the RKTP samples with argon ions, or wet etching in hydrofluoric acid (HF) did not result in any self-assembled domain structures. On the other hand, treatment with water-based solutions of KOH, RbOH,  $\text{KNO}_3$  or  $\text{RbNO}_3$ , did result in self-assembled gratings with similar features in terms of periodicity and domain size. However, ion-bath in pure  $\text{KNO}_3$  at 400 °C for 2 hours did not result in an ordered domain structure. This suggests a surface-layer modification involving  $\text{K}^+$  or  $\text{Rb}^+$  ions, both being native to the RKTP crystal structure, and mediated by the  $\text{OH}^-$  groups.

The following mechanism can be proposed: the  $\text{OH}^-$  anions readily attack the  $c^-$  face, leaving this face ready to take a surplus of  $\text{K}^+$  ions, whereas the  $c^+$  face remains relatively untouched. This results in a change of the surface-layer properties on the  $c^-$  face, which translates into a higher and more uniform nucleation site density. When the external electric field is applied, it is energetically more favorable to nucleate new domains and propagate them along the  $y$  and  $z$  directions than to expand them along the  $x$  axis. In untreated samples, the nucleation site density is more heterogeneous and with a larger span of thresholds, making the sideways growth and nucleation to be competing effects. The switching time measurements further support this idea: the treated samples, poled with 20 ms long square pulses of magnitude 4.4 kV/mm, completely switched in 3 ms, whereas virgin samples, poled at under the same conditions, switched in 6.5 ms. This reduction of the switching time by approximately a factor of two can be associated with a larger nucleation site density and a lower nucleation threshold. Nevertheless, this simplified picture is incomplete. First, the relatively constant domain size suggests some sort of intrinsic effect, related to the crystallographic structure or defects of the RKTP crystal. Second, domain-domain interaction is also possible [9.7], and seems to play an important role. Figure 9.8 shows the former  $c^-$  face of a sample poled at 5.2 kV/mm. It can be clearly seen that the nucleated domains appear already aligned along the  $y$  direction, suggesting electrostatic interaction, and a possible correlated nucleation [9.8, 9.9].

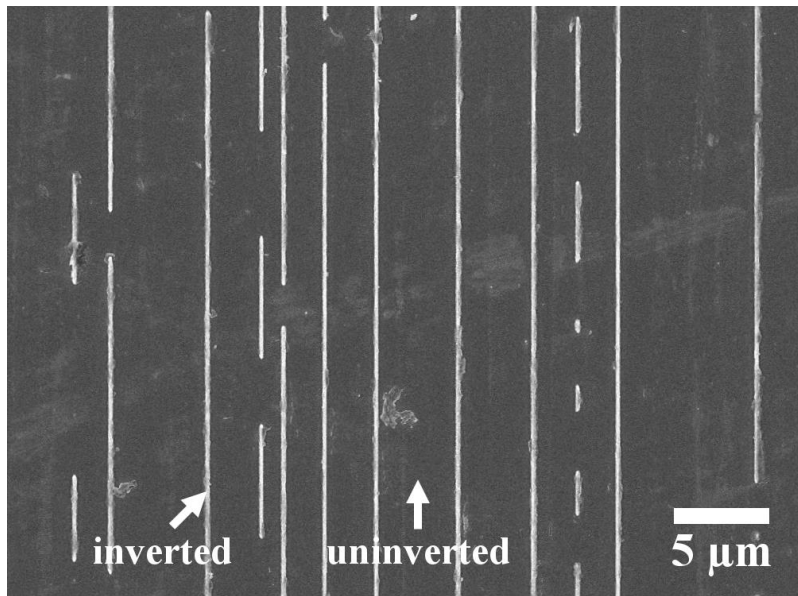


Fig. 9.8. SEM image of the domain structure on the former  $c^-$  face of a SA-RKTP crystal, poled with 5.2 kV/mm.

Further investigations are needed to gain a better understanding of the physical mechanisms behind the self-organized formation of ferroelectric domain structures in the RKTP crystals in order to answer the question whether it is possible to obtain truly periodic sub- $\mu\text{m}$  QPM structures using this relatively simple method.

One of the SA-RKTP crystals, which contained a self-assembled ferroelectric domain structure with a periodicity of  $552 \pm 160$  nm, was used to demonstrate non-collinear 5<sup>th</sup> order

backward propagating QPM second harmonic generation. The experimental setup is shown in fig. 9.7(a), where the inset illustrates the vector diagram for the non-collinear BSHG. The phase-matching relation for non-collinear BSHG is given by [9.10]:

$$\frac{\lambda_{2\omega}}{n_{2\omega}} = \frac{\Lambda}{m} \sqrt{\left(1 - \frac{n_{\omega}}{n_{2\omega}}\right)^2 + \frac{4n_{\omega}}{n_{2\omega}} \sin^2 \theta}, \quad (9.3.1)$$

where  $\lambda_{2\omega}$ ,  $n_{2\omega}$  are the wavelength and the index of refraction of the SH wave,  $\Lambda$  – the QPM period,  $m$  – the QPM order, and  $n_{\omega}$  – the index of refraction of the fundamental wave. The input and output angles,  $\alpha_{in}$  and  $\alpha_{out}$ , can be calculated from the phase-matching relation and the Sellmeier equations. To avoid the total internal reflections of the fundamental and the SH beams, the self-assembled crystal was pumped with 100 fs Ti:Sapphire pulses at a fixed input angle  $\alpha_{in} = 30^\circ$  and the 5<sup>th</sup> order non-collinear BSHG peak at an output angle  $\alpha_{out} = 30^\circ$  was observed.

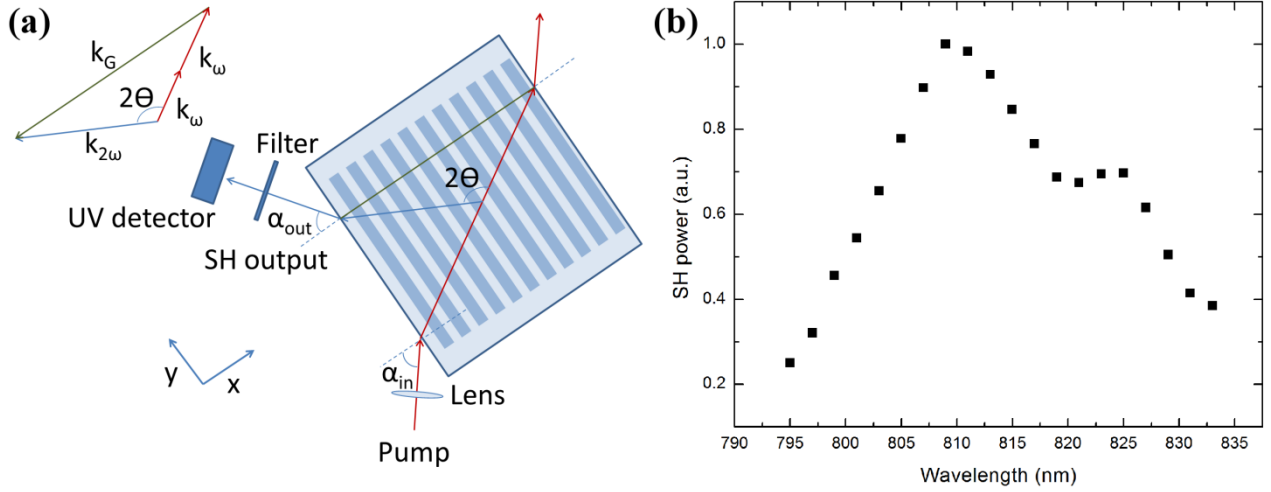


Fig. 9.7. Experimental setup for QPM non-collinear backward second harmonic generation (a) and non-collinear backward second harmonic generation efficiency dependence on the fundamental wavelength in RKTP with self-assembled structures (b).

The wavelength of the pump beam was tuned in 2 nm steps within the range of 795 – 833 nm and the SH output power was measured at each step. The dependence of the non-collinear BSHG power on fundamental wavelength is shown in fig. 9.7(b). The peak of the distribution at 809 nm, corresponds to a period of 555 nm. The large bandwidth of the SH peak reflects a period variation of  $\pm 20$  nm, and was limited by the tuning range of the Ti:sapphire laser.

## References

- 9.1. C. Canalias and V. Pasiskevicius, "Mirrorless optical parametric oscillator," *Nature Photonics* **1**, 459-462 (2007).
- 9.2. C. Canalias, V. Pasiskevicius, R. Clemens, and F. Laurell, "Sub-micron periodically poled flux grown  $\text{KTiOPO}_4$ ," *Appl. Phys. Lett.* **82**, 4233-4235 (2003).
- 9.3. C. Canalias, V. Pasiskevicius, M. Fokine and F. Laurell, "Backward quasi-phase matched second harmonic generation in sub-micrometer periodically poled flux-grown  $\text{KTiOPO}_4$ ," *Appl. Phys. Lett.* **86**, 181105 (2005).
- 9.4. C. E. Valdivia, C. L. Sones, J. G. Scott, S. Mailis, R. W. Eason, D. A. Scymgeour, V. Gopalan, T. Jungk, E. Soergel, and I. Clark, "Nanoscale surface domain formation on the +z face of lithium niobate by pulsed ultraviolet laser illumination," *Appl. Phys. Lett.* **86**, 022906 (2005).
- 9.5. D. O. Alikin, E. I. Shishkin, E. V. Nikolaeva, V. Ya. Shur, M. F. Sarmanova, A. V. Ievlev, M. S. Nebogatikov, and N. V. Gavrilov, "Formation of Self-Assembled Domain Structures in Lithium Niobate Modified by Ar Ions Implantation," *Ferroelectrics* **399**, 35-42 (2010).
- 9.6. I. T. Wellington, C. E. Valdivia, T. J. Sono, C. L. Sones, S. Mailis, and R. W. Eason, "Ordered nano-scale domains in lithium niobate single crystals via phase-mask assisted all-optical poling," *Appl. Surf. Sci.* **253**, 4215-4219 (2007).
- 9.7. L.-H. Peng, Y.-C. Shih, S.-M. Tsan, and C.-C. Hsu, "Mitigation of transverse domain growth in two-dimensional polarization switching of lithium niobate," *Appl. Phys. Lett.* **81**, 5210-5212 (2002).
- 9.8. V. Ya. Shur, E. L. Romyantsev, E. Nikolaeva, E. Shishkin, R. G. Batchko, G. D. Miller, M. M. Fejer, and R. L. Byer, "Micro- and nanoscale domain engineering in lithium niobate and lithium tantalate," *Proc. SPIE* **3992**, 143-154 (2000).
- 9.9. V. Ya. Shur, "Kinetics of ferroelectric domains: Application of general approach to  $\text{LiNbO}_3$  and  $\text{LiTaO}_3$ ," *J. Mater. Sci.* **41**, 199-210 (2006).
- 9.10. S. Moscovich, A. Arie, R. Urneski, A. Agronin, G. Rosenman, and Y. Rosenwaks, "Noncollinear second-harmonic generation in sub-micrometer-poled  $\text{RbTiOPO}_4$ ," *Opt. Express* **12**, 2236-2242 (2004).



## Chapter 10. Conclusions

This work focuses on periodic poling of KTP, RKTP and KTA crystals. It has been shown that optimization of the poling parameters such as electric field pulse shape and duration can significantly improve the QPM grating-quality and reduce domain broadening, enabling fabrication of fine-pitch bulk domain structures. The optical performance of the QPM devices based on different KTP isomorphs has been also evaluated.

Compared to KTP, KTA presents mainly two advantages: first, it has an extended transparency range in infrared region, and second, it has a lower linear absorption in the green spectral region. Prior this work, the potential of KTA for QPM applications had not been fully explored due to the difficulties in implementing QPM structures. For OPO applications, a PPKTA with a period of 39.5  $\mu\text{m}$  and an effective nonlinearity of 10.1 pm/V has been fabricated. The crystal was used in a Nd:YAG-pumped OPO setup to generate a signal wavelength of 1538 nm an idler wavelength of 3452 nm, with a combined signal and idler conversion efficiency of 45%. KTA also proved to be very suitable frequency conversion in the visible spectral range. The crystals poled for green-light generation had a QPM period of 8.49  $\mu\text{m}$  and present an effective nonlinear coefficient as high as 10.5 pm/V with good uniformity over the crystal aperture. They were used to generate 13.6 W output power with 25% conversion efficiency at 533 nm, which today it is the highest power achieved in a CW single pass QPM SHG configuration with a KTP isomorph as a gain medium. In addition, the absorption characteristics of KTA crystals obtained from different growth processes were studied, suggesting that optimization of growth process may play a key role on the transmission properties of KTA in the visible range.

It is well known that the ionic conductivity of the KTP crystals is one of the key factors influencing domain broadening and plays a significant role in periodic poling. This problem is alleviated by using RKTP, which presents an ionic conductivity two orders of magnitude lower than that of regular flux-grown KTP, allowing fabrication of high aspect ratio domain structures. This has been exploited to fabricate large-aperture QPM devices in 5 mm thick crystals, which were used to demonstrate a degenerate QPM-OPO, which generated 60 mJ of combined signal and idler output energy, corresponding to 6 W of average power with a conversion efficiency of 50% at a room temperature. Some of these large aperture crystals were employed in a master-oscillator power amplifier setup to pump ZnGeP<sub>2</sub> OPO in order to reach 6.45  $\mu\text{m}$  wavelength for laser surgery applications.

It has also been demonstrated that RKTP is more resistant to gray-tracking in blue region than conventional flux-grown KTP. This allowed investigating the PPRKTP frequency doubling performance at 796 nm in high-peak power and high-repetition rate regime, showing that the predominant mechanism limiting the SHG efficiency in this spectral range is the two-photon absorption process involving the fundamental and the second harmonic photons.

The potential of RKTP for fabrication of QPM structures with sub- $\mu\text{m}$  periods was also evaluated. The favorable properties of RKTP allow fabrication of periodic QPM structures with a period as short as 690 nm. Moreover, a relatively simple method for self-assembling quasi-

periodic sub- $\mu\text{m}$  ferroelectric domain gratings was introduced by exploiting nucleation enhancement via chemical etching.

The results presented here provide a better understanding of ferroelectric domain dynamics in the KTP isomorphs and enable the fabrication of excellent-quality QPM structures. On the other hand, there are still issues to overcome and improvements to be made. Future work should include the development of a reliable structuring technology of bulk sub- $\mu\text{m}$  QPM gratings to be able to explore the full potential of nonlinear optics involving counter-propagating waves. Moreover, a better understanding of the physical mechanisms behind the self-organized formation of the ferroelectric domain structures in RKTP crystals may open the way to truly periodic self-assembled QPM structures using this relatively simple technique.

Finally, detailed studies of absorption and gray-tracking in the blue and the green spectral regions should further clarify the physical mechanisms behind these phenomena and answer the question whether the crystal growth improvements can enhance the performance of the KTP isomorphs in the visible spectral range.